PREDICTING BEHAVIORS AND EFFECTS OF BIOMASS BURNING

A Dissertation
Presented to
The Academic Faculty

By

Aika Yano Davis

In Partial Fulfillment
of the Requirements for the Degree
Doctor of Philosophy in the
School of Civil and Environmental Engineering

Georgia Institute of Technology

May 2015

PREDICTING BEHAVIORS AND EFFECTS OF BIOMASS BURNING

Approved by:

Dr. Armistead G. Russell, Advisor
School of Civil and Environmental Engineering
Georgia Institute of Technology

Dr. Michael Bergin
School of Civil and Environmental Engineering
Georgia Institute of Technology

Dr. M. Talat Odman, Advisor
School of Civil and Environmental Engineering
Georgia Institute of Technology

Dr. Yongqiang Liu
Southern Research Station
USDA Forest Service

Dr. James A. Mulholland
School of Civil and Environmental Engineering
Georgia Institute of Technology

Dr. Yuhang Wang
School of Earth and Atmospheric Sciences
Georgia Institute of Technology

Date Approved: November 12, 2014

To Gary and our family,

ACKNOWLEDGEMENTS

I would like to thank my advisors, Dr. Talat Odman and Dr. Armistead Russell, for their support and the opportunity to join their research group. I also would like to thank my research group, especially Dr. Yongtao Hu and Dr. David Lavoue, for their help and guidance. I appreciate the assistance I received from Dr. Yongqiang Liu, Dr. James Mulholland, Dr. Michael Bergin, and Dr. Yuhang Wang, whom are on my thesis committee. Finally, I would like to thank my colleagues, friends and family for their love and support throughout my doctoral studies. Gary and Yukiko, words cannot explain how much I appreciate you; love you and thank you.

TABLE OF CONTENTS

LIST OF TABLES

LIST OF FIGURES

Page

SUMMARY

Wildfires and prescribed burns are important sources of air pollution. Both types of biomass burnings can significantly affect air quality downwind at urban locations across large regions. Environmental regulators often rely on Eulerian numerical models for air quality forecasts. Land managers are starting to use Eulerian numerical models to understand the potential impacts of fires [*Larkin et al.*, 2009]. However, the ability of these models to simulate concentrated smoke plumes is limited since they lack fire specific physics and chemistry. Coupling of a sub-grid plume model with a chemical transport model was designed to address this issue.

Daysmoke, an empirical Lagrangian particle model, was used in all the studies with prescribed burning since it is specifically designed for prescribed burning. Many plume dispersion models require a series of models to calculate key input parameters such as fuel loading, fuel consumption, fire spread, heat release, and emission. The various fire models chosen for the study were capable of accurately predicting the input parameters within 15% of measured values for a studied burn event. The uncertainty in input emissions impacted the concentrations predicted by Daysmoke as much as the model's inherent uncertainty due to turbulence.

A new approach of coupling a plume dispersion model with an air quality model was introduced. A plume dispersion model was included inside an air quality model as a sub grid model to calculate plume dispersion until the plume was at a fixed distance away from the fire. This method was carried out by coupling Daysmoke with the Community Multiscale Air Quality modeling system (CMAQ). Coupled Daysmoke-CMAQ improved its performance compared to previous methods of inserting fire emissions at the source.

An adaptive grid was also introduced in Daysmoke-CMAQ to further minimize the effect of numerical diffusion. The horizontal grid in CMAQ increased its resolution towards areas with higher $PM_{2.5}$ concentrations from the fire. The concentration gradient in the plume was better preserved using adaptive grid.

The adaptive grid Daysmoke-CMAQ was also used to simulate prescribed burning scenarios with varying age of fuel bed, season, acreage, ignition type, and time of the day. Each simulated scenario showed varying results due to the changes in input and/or environmental parameters. Older fuel, summers, larger, longer ignition, and afternoon burns showed to increase emissions but did not necessarily increase the magnitude of ground-level $PM_{2.5}$ concentration downwind. Lower ground level $PM_{2.5}$ concentration was achieved when the smoke plume had enough vertical heat flux to reach above the mixing layer.

Deposition of reactive nitrogen species from the atmosphere has been increasing over the last decades, causing vegetation to change in certain areas of US. The effect of anthropogenic and biogenic emissions to nitrogen deposition was studied for 2010 at national parks throughout US. Emissions from mobile sources had the largest influence to reactive nitrogen deposition at most of the national parks, followed by emissions from livestock.

REFERENCES

Achtemeier, G., S. Goodrick, Y. Liu, F. Garcia-Menendez, Y. Hu, and M. Odman (2011), Modeling Smoke Plume-Rise and Dispersion from Southern United States Prescribed Burns with Daysmoke, *Atmosphere*, *2*(3), 358-388.

Larkin, N. K., S. M. O'Neill, R. Solomon, S. Raffuse, T. Strand, D. C. Sullivan, C. Krull, M. Rorig, J. Peterson, and S. A. Ferguson (2009), The BlueSky smoke modeling framework, *International Journal of Wildland Fire*, *18*(8), 906-920.

CHAPTER 1

Introduction

Fire is an important ecological process that affects ecosystems throughout the world. Fires prepare the ground for tree seeding and planting, control disease and tree competition, manage understory debris, and perpetuate fire-dependent plant species. Fires also improve wildlife habitat (e.g. to protect endangered animal species). Though fire is a naturally occurring process on Earth, it has been a concern for humans and our environment. Fires can physically destroy our properties and deteriorate air quality by emitting trace gases, including greenhouse gases, and particulates that can exacerbate cardiovascular and respiratory diseases. PM_{10} (particles smaller than 10 μm in diameter) are known to penetrate into the lower respiratory system of our body, while fine particulates ($PM_{2.5,}$ particulate matter less than or equal to 2.5 μm in aerodynamic diameter) may penetrate further into the gas-exchange region of the lung [*Brunekreef and Holgate*, 2002; *Seaton et al.*, 1995]. Smoke from a fire can also contribute to regional haze and reduce visibility in scenic areas and along major traffic corridors [Achtemeier, 2008]. Smoke can have a negative radiative forcing effect as well [*IPCC*, 2001]. Aerosols emitted from intense wildfires can change vertical profiles of temperature and moisture, as well as cloud microphysics [*Grell et al.*, 2011]. Landslides are common after a burn due to fire removing litter and reducing infiltration of water [*Pierce et al.*, 2004].

Every year wildland fires burn millions of acres [*NIFC*, 2014] and emit 2 Pg of carbon per year [*van der Werf et al.*, 2010]. About half of black carbon emitted globally (5.63 Tg C/yr) is from biomass burning, which includes wildfires and agricultural fires

[*Liousse et al.*, 1996]. In the United States (US), the annual cost for fire suppression can be as much as $1.6 billion for years with severe fires [Whitlock, 2004]. US wildfires account for about 20% of annual emissions of carbon monoxide (CO), $PM_{2.5}$, and volatile organic compounds (VOCs) [*EPA*, 2013]. Although fires can have beneficial effects on some plants and species, large wildfires are often associated with negative ecological effects. With climate changing, wildfire activities and fire severity are expected to increase [*Miller et al.*, 2009; *Westerling et al.*, 2006]. One of the most effective methods to reduce the risk of potential wildfires is a human ignited burning method known as prescribed burning.

Prescribed burning is practiced throughout the world for ecological and safety benefits. Prescribed burnings typically exist in temperate forests [Seiler and Crutzen, 1980] including in Australia (e.g. Fernandes et al., 2013) , Europe (e.g. Montiel and Kraus, 2010), and the southeastern US (e.g. Tian et al., 2008). The Healthy Forests Restoration Act (16 U.S.C. sec. 6501) was introduced in 2002 to promote restoring forests by prescribed burning; however, not enough prescribed burns are being practiced to meet the optimal number of burns for restoring natural ecosystems and reducing damages from unplanned wildfires [Engel, 2013]. Land managers have strict state regulations that must be met to practice prescribed burning. They must get approved for the appropriate weather conditions before performing a safe burn. Some states only allow burnings to occur at certain times of the year to avoid high ozone season. Many states often have strict rules and regulations to reduce the chances of fire escaping [*Yoder*, 2008]. Land managers must also make sure that the surrounding populated area will not exceed the National Ambient Air Quality Standards (NAAQS) as a result of the burn.

$PM_{2.5}$ should not exceed 35 μg/m^3 for a 24-hour average and 15 μg/m^3 for an annual average [*USEPA*, 2012]. A fire forecasting system that can accurately predict smoke behavior and air quality impacts can greatly help in planning for a safe prescribed burning.

Predicting the smoke effects from fires consist of multiple components. Fire models predict fuel loading (fuel available for burning), fuel consumption, fire behavior/spread, heat release, and emissions. Plume dispersion models process the information from fire models to predict plume transport and pollutant concentration downwind of the fire. This simulation order is called the BlueSky Smoke Modeling Framework [*Larkin et al.*, 2009]. The different types of plume dispersion models used include simple box model, Gaussian plume model, puff model, particle model, and full physics model [*Goodrick et al.*, 2013]. The latter types are more complex with fewer limiting assumptions, but come with significant computational cost. Puff, particle, and full physics models all have fire specific physics such as plume buoyancy and entrainment at regional scale. Some plume dispersion models are capable of predicting plume concentrations downwind, but they often do not include pollutant interactions with the environment.

Eulerian grid models have been used worldwide for weather and air quality forecasting. Great advancements have been made in many air quality chemical transport models (CTM) and meteorological models over the last 30 years [*Russell and Dennis*, 2000]. CTMs capture most of the known chemical and physical processes that occur in the atmosphere. Pollutants emitted in a CTM interact with the environment, simulating multiple fire plumes over regional, local, and global domain. However, CTMs cannot

capture the detailed effects of a plume as well as plume dispersion models. Often times, a fire may be smaller than the CTM grid cell, which causes a grid dilution effect and make it difficult to track individual plumes. Many commonly used CTMs do not incorporate fire physics, which makes it impossible for the Eulerian models to predict smoke dispersion accurately. Plume-in-grid (PinG) is a process used to characterize a point source plume into CTMs [*Karamchandani et al.*, 2011]. However, PinG is not appropriate for a wildland fire since it is not a point source, but an area source emission. *Pouliot et al.* [2005] included Bluesky into a CTM using plume heights calculated by Briggs equation, but *Liu et al.* [2013] proved that Briggs equation was not appropriate for some of the burns, especially for prescribed burnings.

The main objectives of this dissertation are to understand the capability of currently available fire/plume models and to improve on fire plume transport simulation in a CTM. An analysis of currently available fire and dispersion models are presented. Each fire model is built to give accurate outputs; however, during the transition from one model to another some of the detailed information gets lost, thus compromising the overall results. My research highlights important parameters in plume dispersion modeling and their uncertainties through simulations of various case studies. For all the studied burn events, extensive on-site measurements are available. The measurements are used to analyze uncertainty, accuracy, and predictability of the models. The second portion of the dissertation is on the new approach of coupling a plume dispersion model with a CTM. Improvements made by the developed system are presented. The system was used to simulate various burn scenarios. The last portion switches gears and focuses

on reactive nitrogen deposition throughout US. A brief description of the objectives for each chapter is given below.

Chapter 2: Fire Emission Uncertainties and their Impact on Smoke Dispersion Predictions: a Case Study at Eglin Air Force Base, Florida, USA

The modeling framework used to simulate fuel loading, fuel consumption, emissions, and plume dispersion within this work is described. For each category, predicted values are directly compared to on-site measurements for the case studied. Measurement uncertainty and model uncertainty for each step in emission prediction are also compared. Performance of a particle dispersion model is evaluated with concentration measurements made downwind. Parameters that increase the uncertainty in smoke plume dispersion prediction are highlighted. The significance of emission uncertainty, measurement uncertainty, and uncertainty inherent in a particle plume model onto downwind concentration predictions are presented.

Chapter 3: Prescribed Burning Plume Dispersion Simulation in an Air Quality Model using Ground and Satellite Data

Fire emissions are often calculated using site-specific ground observations but satellite retrieved data is starting to be used for emission prediction. $PM_{2.5}$ emission rates derived from ground observations and satellite retrievals are compared for a case study. Generally, satellites capture fire spread rate well, however, emissions calculated based on ground observations are known to have better estimates on total emissions. The total emission from site-specific ground measurements redistributed by fractional emission rate derived from satellite retrievals is also studied. The three sets of emission rates are simulated using the smoke dispersion modeling framework described in Chapter 2. The smoke parcel mass is converted into concentration using the grid domain from an air quality model. The predicted plume rises and downwind plume concentrations are

compared to measurements taken by an aircraft that flew through the smoke plume. The importance of accurately predicting total emissions, emission rate, and fire energy release onto plume dispersion modeling is presented.

Chapter 4: Coupling of Lagrangian Particle Smoke Transport Model and Air Quality Model

A new approach for coupling a plume dispersion model in an air quality model is introduced in this chapter. Pros and cons of both a Lagrangian plume model and an Eulerian air quality model are listed. The two models are combined to include benefits from each type of the model. The benefits from the new system are shown through model performance analysis using the same case study as Chapter 3 but with measurement taken at farther distance. Plume release point, spatial scale, and vertical diffusion parameterization in the air quality model are perturbed in an attempt to further improve the modeling system. Limitations to fire plume simulation in a CTM are identified.

Chapter 5: An Assessment of Air Quality Deterioration from Prescribed Burning Scenarios in a Longleaf Pine Forest

The developed fire modeling system from Chapter 4 is used to simulate different burn scenarios. The four important components that are important to land managers are time and size of the burn, age of fuel, season, and ignition type. One of the prescribed burning events at Fort Benning, Georgia is used as a base case for this study. Model performance is evaluated with simulated and measured ground concentrations at various distances downwind of the fire. Fuel, emission, plume dispersion, and downwind concentrations are calculated separately for each scenario. The five components are analyzed by comparing the total amount of fine particulates emitted, plume height, maximum concentration observed, and the concentration increase from the burn event.

Chapter 6: Sensitivity of Reactive Nitrogen Deposition to Anthropogenic and Biogenic Emissions over US National Parks

Deposition of reactive nitrogen species from the atmosphere has been increasing over time. The deposited amount is over the critical load, leading to eutrophication or a change in vegetation. The effect of anthropogenic and biogenic emissions of nitrogen species onto nitrogen deposition is studied for the year of 2010 at four different national parks; Joshua Tree, Grand Teton, Rocky Mountain, and Great Smoky Mountain National Parks. Model performance and accuracy is studied by comparing with site specific measurements and other model predictions. Monthly sensitivity of emissions from different sectors to nitrogen deposition is discussed.

Chapter 7: Conclusions

The key findings from the dissertation are summarized. Future research directions are identified and discussed.

1.1 References

Achtemeier, G. L. (2008), Effects of Moisture Released during Forest Burning on Fog Formation and Implications for Visibility, *Journal of Applied Meteorology and Climatology*, *47*(5), 1287-1296, doi:10.1175/2007JAMC1721.1.

Brunekreef, B., and S. T. Holgate (2002), Air pollution and health, *The lancet*, *360*(9341), 1233-1242.

Engel, K. H. (2013), Perverse Incentives: The Case of Wildfire Smoke Regulation, *Ecology Law Quarterly*, *40*(3).

EPA (2013), 1970 - 2013 Average annual emissions, all criteria pollutants in MS Excel, edited by U. S. Environmental Protection Agency.

Fernandes, P. M., G. M. Davies, D. Ascoli, C. Fernández, F. Moreira, E. Rigolot, C. R. Stoof, J. A. Vega, and D. Molina (2013), Prescribed burning in southern Europe: developing fire management in a dynamic landscape, *Frontiers in Ecology and the Environment*, *11*(s1), e4-e14, doi:10.1890/120298.

Goodrick, S. L., G. L. Achtemeier, N. K. Larkin, Y. Liu, and T. M. Strand (2013), Modelling smoke transport from wildland fires: a review, *International Journal of Wildland Fire*, *22*(1), 83-94.

Grell, G., S. Freitas, M. Stuefer, and J. Fast (2011), Inclusion of biomass burning in WRF-Chem: impact of wildfires on weather forecasts, *Atmospheric Chemistry & Physics*, *11*(11).

IPCC (2001), The global mean radiative forcing of the climate systen for the year 2000, relative to 1750, edited by C. C. W. G. I. T. S. Basis, Intergovernmental Panel on Climate Change.

Karamchandani, P., K. Vijayaraghavan, and G. Yarwood (2011), Sub-grid scale plume modeling, *Atmosphere*, *2*(3), 389-406.

Larkin, N. K., S. M. O'Neill, R. Solomon, S. Raffuse, T. Strand, D. C. Sullivan, C. Krull, M. Rorig, J. Peterson, and S. A. Ferguson (2009), The BlueSky smoke modeling framework, *International Journal of Wildland Fire*, *18*(8), 906-920, doi:http://dx.doi.org/10.1071/WF07086.

Liousse, C., J. Penner, C. Chuang, J. Walton, H. Eddleman, and H. Cachier (1996), A global three-dimensional model study of carbonaceous aerosols, *Journal of Geophysical Research: Atmospheres (1984–2012)*, *101*(D14), 19411-19432.

Liu, Y., S. Goodrick, G. Achtemeier, K. Forbus, and D. Combs (2013), Smoke plume height measurement of prescribed burns in the south-eastern United States, *International Journal of Wildland Fire*, *22*(2), 130-147, doi:http://dx.doi.org/10.1071/WF11072.

Miller, J., H. Safford, M. Crimmins, and A. Thode (2009), Quantitative evidence for increasing forest fire severity in the Sierra Nevada and southern Cascade Mountains, California and Nevada, USA, *Ecosystems*, *12*(1), 16-32.

Montiel, C., and D. T. Kraus (2010), *Best Practices of Fire Use: Prescribed Burning and Suppression: Fire Programmes in Selected Case-study Regions in Europe*, European Forest Institute.

NIFC (2014), Total Wildland Fires and Acres (1960-2009), edited, National Interagency Fire Center.

Pierce, J. L., G. A. Meyer, and A. T. Jull (2004), Fire-induced erosion and millennial-scale climate change in northern ponderosa pine forests, *Nature*, *432*(7013), 87-90.

Pouliot, G., T. Pierce, W. Benjey, S. M. O'Neill, and S. A. Ferguson (2005), Wildfire emission modeling: integrating BlueSky and SMOKE, paper presented at 14th Annual Emissions Inventory Conference, Las Vegas, Nevada, April 11 - 14, 2005.

Russell, A., and R. Dennis (2000), NARSTO critical review of photochemical models and modeling, *Atmos Environ*, *34*(12), 2283-2324.

Seaton, A., D. Godden, W. MacNee, and K. Donaldson (1995), Particulate air pollution and acute health effects, *The Lancet*, *345*(8943), 176-178.

Seiler, W., and P. Crutzen (1980), Estimates of gross and net fluxes of carbon between the biosphere and the atmosphere from biomass burning, *Climatic Change*, *2*(3), 207-247, doi:10.1007/BF00137988.

Tian, D., Y. Hu, Y. Wang, J. W. Boylan, M. Zheng, and A. G. Russell (2008), Assessment of biomass burning emissions and their impacts on urban and regional PM2. 5: A Georgia case study, *Environmental Science & Technology*, *43*(2), 299-305.

USEPA (2012), National Ambient Air Quality Standards for Particulate Matter; Final

Rule, edited by E. P. Agency, the Government Printing Office, Washington, DC.

van der Werf, G. R., J. T. Randerson, L. Giglio, G. Collatz, M. Mu, P. S. Kasibhatla, D. C. Morton, R. DeFries, Y. v. Jin, and T. T. van Leeuwen (2010), Global fire emissions and the contribution of deforestation, savanna, forest, agricultural, and peat fires (1997–2009), *Atmospheric Chemistry and Physics*, *10*(23), 11707-11735.

Westerling, A. L., H. G. Hidalgo, D. R. Cayan, and T. W. Swetnam (2006), Warming and earlier spring increase western US forest wildfire activity, *science*, *313*(5789), 940-943.

Whitlock, C. (2004), Land management: Forests, fires and climate, *Nature*, *432*(7013), 28-29.

Yoder, J. (2008), Liability, regulation, and endogenous risk: the incidence and severity of escaped prescribed fires in the United States, *Journal of law and economics*, *51*(2), 297-325.

CHAPTER 2

Fire Emission Uncertainties and their Impact on Smoke Dispersion Predictions: a Case Study at Eglin Air Force Base, Florida, USA[1]

Abstract

Prescribed burning is practiced to benefit ecosystems but the resulting emissions can adversely impact air quality. A better understanding of the uncertainties in emission estimates and how these uncertainties impact smoke predictions is critical for model-based decision making. This study examined uncertainties associated with estimating fire emissions and how they affect smoke concentrations downwind from a prescribed burn that was conducted at Eglin Air Force Base in Florida, US. Estimated variables used in the modeled emission calculation were compared to field measurements. Fuel loadings, fuel consumption, and emission factors were simulated using Photo Series, Consume, and previously published values. A plume dispersion model was used to study the effect of uncertainty in emissions on ground concentration prediction.

The fire emission models predicted fuel loading, fuel consumption, and emission factor within 15% of measurements. Approximately 18% uncertainty in field measurements of $PM_{2.5}$ emissions and 36% uncertainty attributed to variability in emission estimating models resulted in 20% and 42% ground level $PM_{2.5}$ concentration

---

This chapter was accepted to International Journal of Wildland Fires. Co-authors are Yongtao Hu, Armistead Russell, M. Talat Odman, Roger Ottmar, Scott Goodrick, Yongqiang Liu, Gary Achtemeier, Brian Gullett, Johanna Aurell, William Stevens, Roby Greenwald, and J. Kevin Hiers.

uncertainties, respectively, in dispersion modeling using Daysmoke. Uncertainty in input emissions impacts the concentrations predicted by the smoke dispersion model just as much as the model's inherent uncertainty due to turbulence.

2.1 Introduction

Prescribed burning is practiced throughout the world for ecological and safety benefits, and it is mostly practiced in temperate forests [*Seiler and Crutzen*, 1980] including Australia [*Fernandes et al*., 2013], Europe [*Montiel and Kraus*, 2010], and the southeastern United States (US) [*Tian et al*., 2008]. Prescribed burning is used to prepare the ground for tree seeding and planting; to control disease and tree competition; to manage understory debris; and to perpetuate fire-dependent plant species. Prescribed burning can also improve wildlife habitat (e.g. by protecting the habitat of endangered animal species) and reduce wildfire risk. However, prescribed burning produces smoke and release gases that may deteriorate air quality in local urban areas [*Hu et al*., 2008; *Y. Liu et al*., 2009]. The smoke can also contribute to regional haze that reduces visibility in scenic areas and along major traffic corridors [*G Achtemeier*, 2008]. US Environmental Protection Agency (EPA) 2011 National Emission Inventory [2013] reported that 15% (8.4×10^8 kg) of $PM_{2.5}$ (i.e., particulate matter less than 2.5 μm in aerodynamic diameter) emissions in the US are attributed to prescribed burnings, and 27% of $PM_{2.5}$ emissions from prescribed burnings originate from the southeastern US. Prescribed burning emissions remain as one of the most prominent sources of $PM_{2.5}$ in the southeastern US, and will become an increasing fraction as other sources are controlled.

Responsible practice of prescribed burning entails accurate predictions of air quality impacts to mitigate the potential to adversely impact air quality in heavily

populated regions. Several modeling tools are available for use in prescribed burning management [*G Achtemeier et al*., 2011; *Anderson et al*., 2004; *Andrews et al*., 2003; *Larkin et al*., 2009; *R D Ottmar*, 2014; *Pouliot et al*., 2005; *Prichard et al*., 2007; *Weise and Wright*, 2014]. The models are used to estimate fuel consumption, smoke emissions, plume transport, dispersion, and whether the pollutants would impact air quality in urban areas. Complex models may yield greater accuracy in predictions; however they require greater computational resources and time. Whether simple or complex, all models and their predictions are subject to uncertainty.

Several field and modeling studies have been conducted to better quantify prescribed burning emissions and associated uncertainties: French *et al*. [2004], Wiedinmyer *et al*. [2006], Tian *et al*. [2008], and Urbanski *et al*. [2011]. However, there are few studies that examine the effect of emission uncertainties on local air quality predictions. In this study, data was collected from a comprehensive field campaign called the Prescribed Fire Combustion and Atmospheric Dynamics Research Experiment (Rx-CADRE). Rx-CADRE was conducted at Eglin Air Force Base (AFB) near Niceville, Florida US; it provided a unique opportunity to evaluate uncertainties in emissions derived from measurements as well as emissions predicted by fire models. The magnitude of impact on smoke dispersion predictions from emission uncertainty was evaluated through a plume dispersion model. With a better understanding of uncertainties associated with estimated emissions and downwind concentrations, land managers should be able to better assess if a burn would lead to violation of air quality regulations such as the US National Ambient Air Quality Standards (NAAQS).

2.2 Site and Burn Description

The Rx-CADRE prescribed burn monitored for this study was unit 608A, a fairly flat unit, located at 30° 38' 38.76"N, 86° 16' 36.84"W in Eglin AFB (Figure 2.1). The 831 ha (2054 acre) unit was burned on 8 February 2011. Clear skies were observed with winds shifting from north to northeasterly during the burn. The fuel bed was classified as managed long leaf pine (*Pinus palustris*) and turkey oak (*Quercus laevis*) forest with an understory of little bluestem (*Schizachyrium scoparium*), palmetto (*Serenoa repens*), and grass (*Andropogon Virginicus*). Long leaf pine litter was the main fuel that carried the fire. A helicopter initiated ignition at 1159 Central Standard Time (CST) and the first half of the ignition was a backing fire that completed at 1251 CST. The remaining unit was ignited by head fire that started at 1323 CST and was completed at 1356 CST. The fuels continued to be consumed until 1420 CST. A tethered aerostat, a balloon with instruments restrained by cables attached to a vehicle, was launched to obtain measurements required for emission calculations near the burn site (Figure 2.1). There were two sites where the ground level concentration of $PM_{2.5}$ was measured: a stationary site at 4.0 km downwind, and a mobile site #2 at 9.2 km downwind (Figure 2.1). Initially these sites were roughly under the centerline of the plume, but when the wind shifted, the sites were off centered.

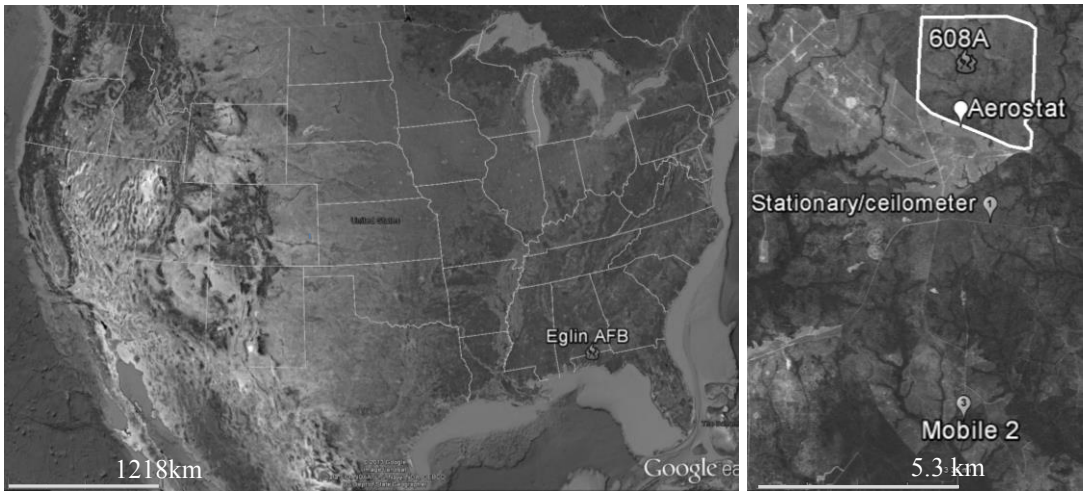

Figure 2.1: Location of Eglin AFB in FL, US (left) and a map of the burn site, showing Unit 608A bordered in white, the site of the aerostat and sonic anemometer at 1.4 km away from fire center (white balloon), the stationary and ceilometer site 4.0 km away (balloon #1), and Mobile 2 site 9.2 km away (balloon #3), shown on Google Earth [*GoogleEarth7.1*, 2013].

2.3 Materials and Methods

2.3.1 Emission

Prescribed burning emissions (E) for specific fuel types were calculated by multiplying the fuel loading consumed (FC; mass of burned vegetation per unit area) by an emission factor (EF; mass of compound emitted per mass of burned vegetation) and the total area burned (A) [*Seiler and Crutzen*, 1980]:

$$E = \mathrm{FC} \times \mathrm{EF} \times \mathrm{A} \qquad (1).$$

Fuel loading was studied first, followed by fuel consumption, emission factor, emissions, and plume dispersion (Figure 2.2). On-site measurements and model predictions were compared for each variable studied. Measurement procedures and modeling methods are described in the following sections.

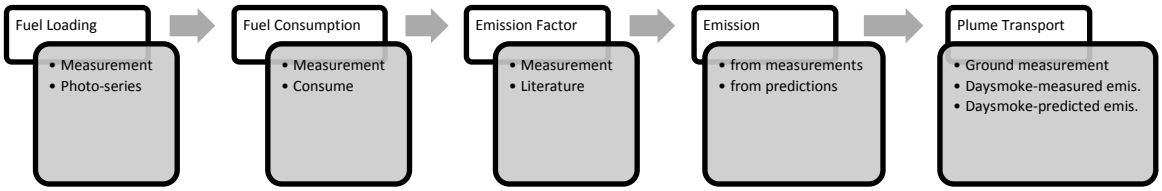

Figure 2.2: Framework used to predict fire emissions and plume transport. Calculated variables are shown in top white boxes and different ways of obtaining the variable are listed under each variable.

2.3.1.1 Fuel loading

Fuel loading is the total amount of vegetation that is on the site (mass per unit area). For both pre- and post- fire fuel loading measurements, standard ground-based inventory techniques [*Brown*, 1974] were used. There were three sampling locations, each representing one of the three distinctive vegetation types in unit 608A. 20 destructive clip plots (1 m^2 each) were collected at each sampling location. All biomass was sorted by fuel bed components including litter (all non-decomposed dead plant material including needles, leaves, etc.), duff (fermentation and humus layers) and understory vegetation biomass including herbaceous vegetation (grass and herbs), woody vegetation (shrubs and seedlings), palmetto, and 1-h, 10-h, and 100-h time lag dead woody fuels (representing woody fuel diameters of 0-0.60 cm, 0.61-2.5cm and 2.6-7.6 cm, respectively). The fuel material was oven-dried at 70 °C, then weighed to determine the dry fuel mass using area-weighted averages of three fuel loadings (Table 2.1). Because there were very few logs and little duff, those two fuel bed components were not measured.

Table 2.1: Photo-series-estimated vs. measured fuel loadings and modeled-by-Consume vs. measured consumptions by fuel type for Unit 608A at Eglin Air Force Base on 8 February 2011. Woody fuel debris consumptions are summed up into one number. 60 samples were averaged.

		Woody Fuels			Shrub	Nonwoody	Litter	Total
		1-h	10-h	100-h				
Fuel Loading	Field measurement	0.01	0.05	0.11	0.02	0.08	0.33	0.59
(kg m^{-2})	Photo series	0.02	0.07	0.09	0.01	0.03	0.44	0.66
Consumption	Field measurement		0.10		0.01	0.07	0.30	0.49
(kg m^{-2})	Photo/Consume		0.09		0.00	0.03	0.44	0.56

The fuel loading prior to the burn was predicted by the Stereo Fuels Photo Series for Quantifying fuels, Volume VIa [*R Ottmar et al*., 2003]. The fuels were identified closely to Sand hill (SH) 10 within the series with its cover type defined as Longleaf Pine-Scrub Oak (Society of American Foresters (SAF) 071). Since very little duff was observed on site, duff was assumed to be negligible and was not considered in fuel loading estimation. Listed values of fuel loadings for woody and surface material were compared with field measurements (Table 2.1). The summation over all fuel loadings for each fuel type is the total fuel loading.

2.3.1.2 Fuel Consumption

Fuel consumption is the amount of vegetation that burned during the fire (mass per unit area). The measured fuel consumption was determined by taking the difference between measured pre- and post-burn fuel loadings. The 20 post-burn destructive clip plots were offset from the pre-burn clipped plots to get post-burn fuel loading. The different fuel species remaining after the burn were separated into four different fuel bed

categories: shrubs (i.e., living and dead palmetto, woody shrub, yucca), grass (i.e., wiregrass, other grass, live and dead forbs), woody debris of all sizes smaller than 7.6 cm in diameter, and litter. The averages of each fuel bed category are presented in Table 2.1.

Consume 3.0 [*Prichard et al*., 2007] was used to predict how much of the fuel loading estimated from the Photo Series would be consumed by the fire. Consume takes in fuel characteristics, lighting patterns, fuel conditions, and meteorological attributes, and outputs fuel consumption by fuel bed categories. The following assumptions were made when running the model: 1) The crown consumption was considered to be zero because the objective of this prescribed fire was to burn in such a way that minimized crown consumption; 2) An ocular estimation rather than a true inventory was used because of limited inventory time and 80% of the shrubs were detected to be alive; and 3) The measured values for the depth (2.5 cm or 1 inch) and the fuel coverage of litter (70% coverage of the ground) were also used in Consume.

Fuel moisture is a significant factor in determining combustion efficiency [*Grandesso et al*., 2011]. Therefore, the measured fuel moisture values were used in Consume to minimize the effect of fuel moisture uncertainty on the consumption calculations. Fuel moisture values were determined by collecting samples of fuels immediately before the burn and weighing the samples. The same samples were later dried for 48 hours at a minimum of 70 °C and reweighed to obtain the percent fuel moisture content for each fuel bed category. The total mass of fuel consumed per unit area was calculated by summing the fuel consumptions for each fuel bed category.

2.3.1.3 Emission Factor

The $PM_{2.5}$ emission factor specific to this case study was derived from the filter sample collected by the aerostat located within 200 m of the burn site. The average $PM_{2.5}$ concentration derived from the filter sample was converted to an emission factor using the carbon mass balance approach [*Laursen et al*., 1992]. The carbon mass balance method assumes that all the carbon released by combustion was measured. The average $PM_{2.5}$ concentration divided by the sum of averages of measured carbon species and multiplied by carbon fraction in the biomass is the emission factor. 50% of the biomass was assumed to be carbon. Although the majority of carbon emitted is CO or CO_2, not all carbon species from combustion can be measured. Therefore, the $PM_{2.5}$ emission factor derived from carbon mass method tends to be slightly overestimated. Details on the aerostat's measurements and emission factor calculation can be found in Aurell and Gullett [2013]. The product of measured fuel consumption, emission factor, and the area of the burn is referenced as the total measured emissions, and this is listed in Table 2.2. The size of 608A was assumed to be equal to the area of the burn.

Table 2.2: Measured fuel loading, fuel consumption, and $PM_{2.5}$ emission factor vs. Photo-series-estimated fuel loading, modeled-by-Consume fuel consumption, and mean of published emission factors for Eglin Air Force Base.

	Fuel Loading ($kg\ m^{-2}$)	Fuel Consumption ($kg\ m^{-2}$)	$PM_{2.5}$ Emission Factor ($g\ kg^{-1}$)	$PM_{2.5}$ Emissions (kg)
Measured	0.59 ± 0.06	0.49 ± 0.06	14 ± 1.9	5.69×10^{4}
Modeled	0.66	0.56	13	6.08×10^{4}
Difference	11%	15%	-7%	7%

In emission modeling, emission factors are typically obtained from literature. Emission factors applicable to biomass at Eglin AFB were collected from various sources. In the US EPA AP-42 [1995] database, the $PM_{2.5}$ emission factor for conifer long needle biomass (13 g kg^{-1}) was assumed to be the most appropriate for this study. Urbanski *et al*. [2008] listed $PM_{2.5}$ emission factors from various burns conducted throughout the US and from previous measurements specific to Eglin AFB at 6.9 g kg^{-1} and 11.9 g kg^{-1}, respectively. Aurell and Gullett [2013] listed $PM_{2.5}$ emission factors obtained from another Rx-CADRE burn using filter measurements (13 g kg^{-1}) and simulated burns at an open burn test facility using fuels collected at Eglin (12, 15, and 19 g kg^{-1}). The mean and the standard deviation of the mentioned $PM_{2.5}$ emission factors were 13 and 3.4 g kg^{-1}, respectively. This value was used as the modeled emission factor. The total modeled emissions were calculated by taking the product of the modeled fuel consumption with this emission factor and the area of the burn.

2.3.2 Plume Dispersion

Lagrangian stochastic models are often applied to follow tracer particles in turbulent flow, and this type of model is especially suitable for quantifying how emissions from a particular source impact air quality [*Wilson and Sawford*, 1996]. This prescribed burn was simulated using Daysmoke, an empirical-stochastic fire plume model, which has been developed specifically for prescribed burnings in the southeastern US [*G Achtemeier et al*., 2011]. Daysmoke requires emission rates, updraft core numbers (the number of organized, rising plumes in a burn), updraft core vertical velocities, maximum initial updraft core diameters as well as vertical profiles of meteorological data as inputs for every 12 minutes [*GL Achtemeier et al*., 2012; *G Achtemeier et al*., 2011].

The ambient vertical temperature profile was used in the calculations that determine plume stability and plume height.

2.3.2.1 Time Profile of Heat Release and Relative Emission

Location and number of updraft cores, updraft core vertical velocities, maximum initial updraft core diameters, fractional emission rates, and the percentage of total emission per unit time, were all obtained from a cellular automata fire spread model called Rabbit Rules [*GL Achtemeier et al*., 2012]. 12-minute averages of these variables (Figure 2.3) were used. In all Daysmoke simulations, the updraft core numbers and the updraft core vertical velocities from Rabbit Rules were kept the same. Emission rates were derived by multiplying the fractional emission rates with the total measured or modeled emissions.

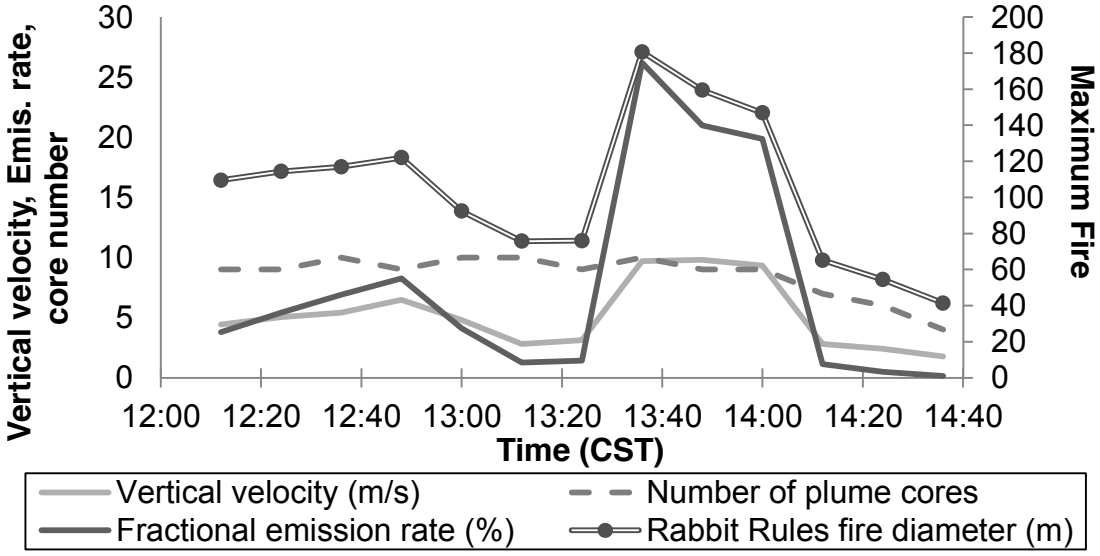

Figure 2.3: Time dependent updraft core vertical velocity, updraft core number, maximum initial updraft core diameter, and fractional emission rates produced by Rabbit Rules [*GL Achtemeier et al*., 2012].

The Daysmoke simulation using emissions calculated from the field measurements used the maximum initial updraft core diameters directly from Rabbit Rules. To obtain the maximum initial updraft core diameter ($Fdia$) commensurate with predicted emissions from the modeled case, the initial updraft core diameter from Rabbit Rule was adjusted following its relationship with heat release (Q), $Q \propto Fdia^2$, from Mercer and Weber [2001]. The hourly heat release rate was obtained from the Fire Emission Production Simulator (FEPS) [*Anderson et al*., 2004]. FEPS requires information such as fuel loading, fuel moisture, total consumption per acre, area burned per hour, and start and end times of ignition. FEPS was applied twice, once with measured fuel consumptions and the other time with estimated fuel consumptions from Consume 3.0. Since a helicopter ignited the burn and there were very little duff or large woody fuels, the fire burned efficiently, leading to an estimate of 95% fuel bed involvement in the flaming combustion stage and the remaining 5% in the long term smoldering stage.

2.3.2.2 Meteorology

Other sources of uncertainty in smoke dispersion simulations include model formulation, atmospheric stability, wind speed (WS), and most importantly wind direction (WD) [*Garcia-Menendez et al*., 2013; *Jain et al*., 2007]. Because this study focused on emission uncertainty, the uncertainty created by meteorology predictions was minimized by modifying modeled wind profiles to best match the observations.

The Weather Research and Forecasting Model (WRF) is an Eularian numerical weather prediction system used at the mesoscale level [*Skamarock et al*., 2008]. Different physics options are included in the model to simulate the planetary boundary layer, land-

surface processes, atmospheric and surface radiation, microphysics, and cumulus convection. Some of the schemes we used are Unified Noah land-surface model, YSU boundary layer scheme, and Kain-Fritsch (new Eta) cumulus scheme. WRF is capable of nesting its results to a smaller domain with a smaller grid resolution. WRF product is treated with interface processors to convert its format to be used in the chemical transport model.

WRF was used at 1.3 km grid resolution for this study. The dispersion model used the modified WRF vertical profiles taken at the center of the burn lot at every hour during the burn. The predicted atmospheric stability was in agreement with observations recorded around the burn site; however, wind speed and wind direction needed to be modified to match the real-time wind measurements taken on site. The first set of wind velocity measurements was taken by a 3D sonic anemometer (Young 81000, R.M. Young Corp.) on the aerostat [*Stevens et al*., 2013], at its measurement height ranging from 38 to 280 m. The second set of wind measurements was taken at 10 m above ground at approximately the same location as the aerostat. The third measurement was taken at 2 m above ground at 4.0 km downwind of the center of the burn lot.

The wind speed predicted for the burn site by WRF was evaluated against the three measured wind speeds. The wind speed ($\bar{u}$) at z meters above ground was corrected using logarithmic wind profile [*Holton*, 2004]:

$$\bar{u} = \frac{u_*}{k} \ln\left(\frac{z}{z_o}\right) \tag{2}$$

where z_o is the roughness length, u_* is the friction velocity, and k is von Karman's constant. These three values were adjusted so the boundary layer theory profile in Equation (2) became the least square fit for the three measurements and the WRF

prediction at planetary boundary layer (PBL) height. The values used to adjust WRF wind speed are listed hour by hour in Table 2.3. Since the smoke dispersion model's emission rate changed hourly, the WSs were corrected hourly as well.

Table 2.3: The roughness length (z_o), the friction velocity (u_*), and von Karman's constant (k) used for the least square fit on wind speed from 1200 CST to 1400 CST.

CST	z_o **(m)**	u_* **(m s^{-1})**	k
1200	6.1	0.5	1.8
1300	3.5	0.4	2.2
1400	0.3	0.3	4.8

Similar to the modification procedure with wind speed, wind direction was adjusted so the wind direction profile also became the least square fit through the three measured wind directions. The wind direction profile employed was the simplified Ekman spiral [*Holton*, 2004]. The directional wind vectors u_z and v_z at height z in Ekman spiral were simplified for the Northern Hemisphere as

$$u_z = u_g\left(1 - e^{-\pi z/De}\cos(\pi z/De)\right),\ v_z = u_g e^{-\pi z/De}\sin(\pi z/De) \qquad (3)$$

where u_g is the geostrophic wind and De is the PBL layer depth, which is obtained from WRF.

The directional wind vectors were used to calculate the angle by which the wind rotates at height z with respect to the wind at ground level:

$$\Delta WD_z = \tan^{-1}\left(\frac{v_z}{u_z}\right) \times \frac{180}{\pi}, \qquad \Delta WD_0 = 0^{\circ} \qquad (4)$$

where ΔWD_z is wind rotation angle. Wind direction at the ground level was obtained from least square curve fit to the three measurements. The adjusted wind direction was the sum of wind rotation angle with the optimized WD at ground:

$$WD_{adjusted,z} = \Delta WD_z + WD_{ground} \quad (5).$$

These hourly adjusted wind speed and wind direction were then input to Daysmoke.

Figure 2.4 shows the wind speeds measured and predicted at different times of the burn. The error bars represent the standard deviation of the measurements for each hour. For the three hours of simulation, WRF over predicted wind speed in all vertical layers in the PBL. The adjusted WRF profile was within one standard deviation of the three measurements. For 1200 CST to 1400 CST, WRF winds were reduced near the ground. The adjusted WS maximum decrease was 2.9 m s^{-1}, which was an 85% reduction.

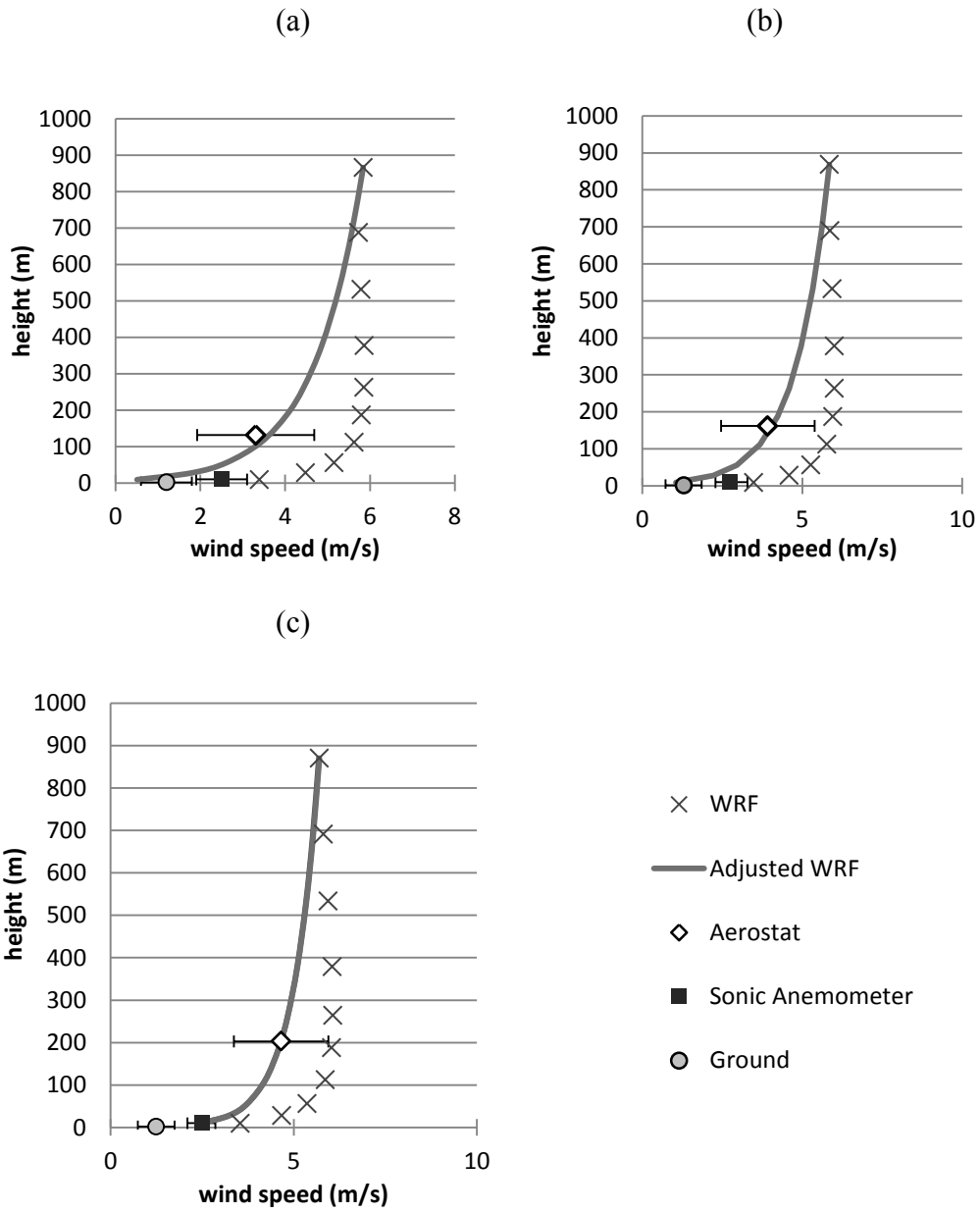

Figure 2.4: Comparison of measured and WRF-predicted wind speeds at a) 1200 CST, b) 1300 CST, and c) 1400 CST. Measurements are at the ground (2 m), on a mast (10 m), and by the aerostat (hourly average ranging from 131 m to 203 m). WRF winds adjusted by the three measurements are also shown. Horizontal error bars represent standard deviation for each hour.

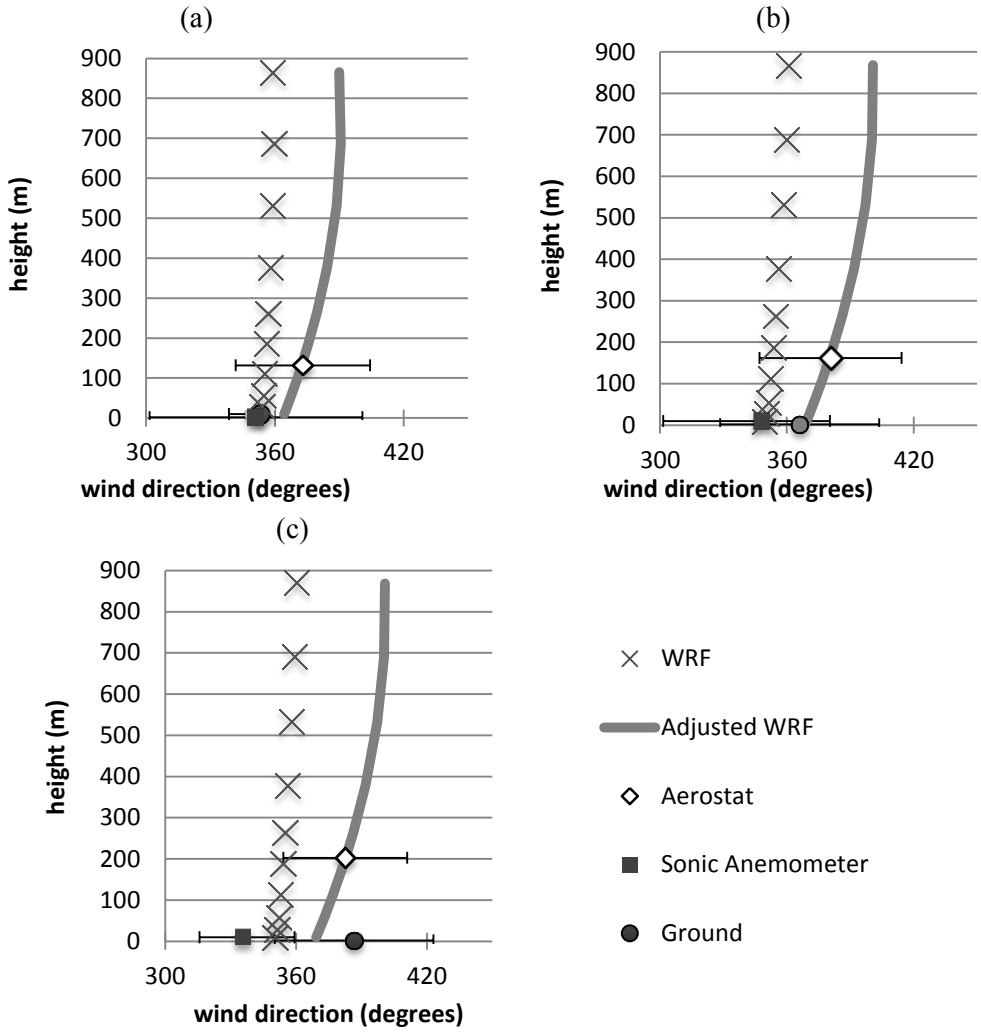

Figure 2.5: Comparison of measured and WRF-predicted wind directions at a) 1200 CST, b) 1300 CST, and c) 1400 CST. Measurements are at the ground (2 m), on a mast (10 m), and by the aerostat (131-203 m). WRF winds adjusted by the three measurements are also shown. Horizontal error bars represent standard deviation of measurements during each hour.

Figure 2.5 shows the wind directions measured and predicted during the burn. WRF wind directions were overpredicted (more easterly) at the ground (2 m) but underpredicted (more westerly) aloft (10 m and 131-203 m) for the majority of the burn period. Predicted winds from WRF generally were from the northwest, although the winds measured on and aboveground for 1300 CST and 1400 CST were from the

northeast. WRF wind direction at the top of PBL rotated by only 11 degrees with respect to the wind direction on the ground, but the adjusted wind direction at the top of PBL rotated 43 degrees from wind direction at ground level.

Table 2.4 shows the wind speed and wind direction that WRF originally predicted and adjusted wind speed and wind direction at 850 m above ground for three different hours during the burn. Adjusted wind speed at this height did not deviate much from the originally predicted values but the wind speeds closer to the ground did get reduced greatly. Vertical profiles of the adjusted wind speed and wind direction, and unadjusted temperature and relative humidity from WRF were input to Daysmoke.

Table 2.4: Original WRF-predicted wind speed and wind direction compared to WS and WD values adjusted to field measurements.

	WRF original		***Adjusted***	
CST	**WS (m s^{-1})**	**WD (degrees)**	**WS (m s^{-1})**	**WD (degrees)**
1200	5.8	-1.0	5.8	20
1300	5.9	0.7	5.8	41
1400	5.7	0.3	5.7	55

2.3.2.3 Plume Height

Daysmoke assigns a smoke parcel to every one kilogram of $PM_{2.5}$ emitted and tracks the trajectory of those parcels in a Lagrangian stochastic framework [2011]. The coordinates of the smoke parcels were used to predict the plume height and the ground concentration. To characterize the random variability in Daysmoke, the model was run 40 times for each emissions case: one with emission rates derived from the measurements and fire diameter directly from Rabbit Rules, and the other with modeled emission rates

and modified fire diameter using the relationship with heat release. The rest of the required variables were kept constant for all of Daysmoke simulations. From the 40 Daysmoke outputs, the mean and the standard deviation of the plume heights and the downwind concentrations were calculated at ten-minute intervals.

Simulated plume heights were evaluated with plume height measurements from Vaisala CL31 backscatter ceilometer designed around laser LIDAR technology [*Y Liu et al*., 2013]**.** The ceilometer emits short, powerful laser pulses at a wavelength of 0.9 μm in a vertical or slant direction. The backscattered light from aerosols found in the smoke plume, which is dominated by particles with a diameter of one micron and smaller [*Reid et al*., 2005], is measured as the LIDAR scans the sky. The ceilometer has a range of 7.5 km at a resolution of 20 m, with a detection frequency that is as high as two seconds. This ceilometer was located four kilometers away from the burn (Figure 2.1). The Daysmoke plume heights were calculated as the average height of the simulated smoke parcels near the ceilometer. Ten-minute averages of Daysmoke-simulated and measured plume heights were compared.

2.3.2.4 Ground Concentration

Daysmoke's performance was evaluated using measured ground level $PM_{2.5}$ concentrations at 4.0 and 9.2 km downwind from the burn site. Two continuous sampling instruments, a Tapered Element Oscillating Microbalance or TEOM (Thermo Scientific in Waltham, Massachusetts US) and an AeroTrak handheld particle counter Model 9306 (TSI Inc. in Shoreview, Minnesota US), both sampling at 10-second time step, were used. AeroTrak was available at both measurement sites and TEOM was used at the closer site to verify the AeroTrak measurements as well as to calculate the measurement uncertainty

associated with ground concentrations. The average concentrations of 40 Daysmoke runs at the two study sites were compared with the averages of AeroTrak measurements at every ten minutes.

2.3.3 Error Analysis

Two measures of model performance were calculated; the root mean squared error (RMSE) and the mean fractional error (MFE). RMSE aggregates the magnitudes of the errors in predictions. RMSE is expressed as:

$$RMSE = \sqrt{\frac{1}{n}\sum_{i=1}^{n}(P_i - O_i)^2} \tag{6}$$

where O_i is the i^{th} measured ground concentration out of n available measurements, and P_i is the ground concentration simulated by Daysmoke. MFE is often used in concentration comparisons because it has the advantage of equally weighting the biases for small and large predictions or observations [*Boylan and Russell*, 2006]. Using the same notation as RMSE, MFE is expressed as:

$$MFE = \frac{1}{n}\sum_{i=1}^{n}\frac{|P_i - O_i|}{\left(\frac{P_i + O_i}{2}\right)} \tag{7}$$

The modeled emissions and the measurement-derived emissions were also compared with these two metrics. Increases in RMSE and MFE due to input emission uncertainties were also studied.

Measurement uncertainties in fuel loading, fuel consumption (∂FC) and emission factor (∂EF) were estimated (Table 2.2) and they were propagated to estimate the total emission uncertainty (∂E):

$$\frac{\partial E}{E_{meas.}} = \sqrt{\left(\frac{\partial FC}{FC_{meas.}}\right)^2 + \left(\frac{\partial EF}{EF_{meas.}}\right)^2}. \quad (8)$$

The upper and lower bounds of total emissions ($E_{meas.} \pm \partial E$) were converted into emission rates using the fractional emission rates as described previously. The two sets of emission rates were input into Daysmoke and were simulated 40 times each. The ten-minute averages of $PM_{2.5}$ ground concentrations at the two measurement sites as well as across the plume at 9.2 km downwind were used as the basis to study the effect of input emissions uncertainty on ground concentration uncertainty. For the analysis across the plume, the concentrations were extracted from ten equally spaced points within the plume width.

The differences of modeled values from measured values ($\Delta x = x_{modeled} - x_{measured}$) were also studied. Since there were multiple emission factors to choose from, we defined the difference of "modeled" emission factor as the difference of the mean from the measured emission factor plus one standard deviation of the emission factors. The difference in total emissions (ΔE) is defined as

$$\frac{\Delta E}{E_{modeled}} = \sqrt{\left(\frac{\Delta FC}{FC_{modeled}}\right)^2 + \left(\frac{\Delta EF}{EF_{modeled}}\right)^2}. \quad (9)$$

The upper and lower deviation bound of total emission were also simulated in Daysmoke. Similarly, the ten-minute averages of $PM_{2.5}$ ground concentrations at the three studied areas were extracted.

2.4 Results and Discussion

2.4.1 Model Evaluation

Plume heights estimated by Daysmoke were in agreement with measured plume height from the ceilometer (Figure 2.6). The predicted plume heights using measurement-derived emissions and modeled emissions were consistently within one standard deviation of the measurements. The ceilometer measurements had a large standard deviation because the wind conditions created the plume to be turbulent, causing the plume height to vary frequently over time. Daysmoke did not capture the first sharp increase in the observed plume height at 1230 CST but instead simulated a gradual increase over time, similar to the fire diameter predicted by Rabbit Rules (Figure 2.3). Due to the second half of firing, which was represented by fractional emission rates and fire diameters increasing around 1330 CST, Daysmoke predicted the second increase in plume height similar to the measurements. The ceilometer measured the average plume height to be 860 m, and Daysmoke's average plume height using measurement-derived emissions was 760 m with MFE of 16%. The average plume height simulated using modeled emissions was 780 m with MFE of 13%, which was closer to the measurements than the case with measurement-derived emissions. Since the modeled fuel consumption was larger than the measured fuel consumption, the plume using the modeled emissions had larger heat release. With more heat released, the plume was more buoyant, leading to a 3% higher plume height than the plume height from measurement-derived emissions.

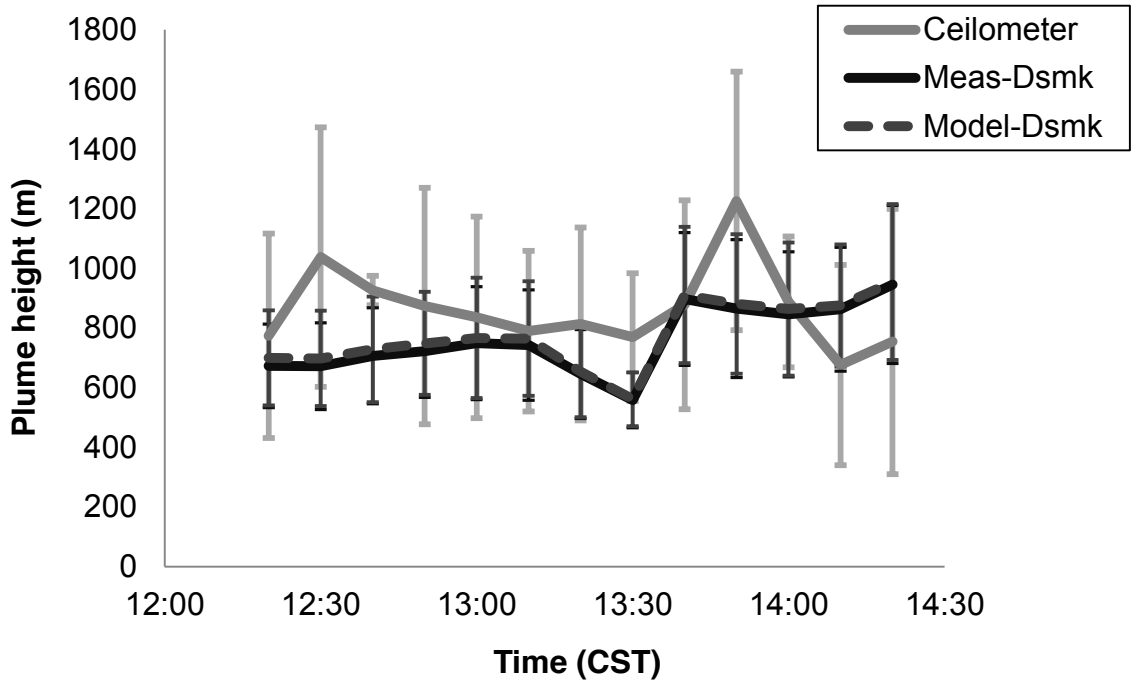

Figure 2.6: Ten-minute average plume height comparison between ceilometer measurement (light grey) and Daysmoke-simulated plume heights using emissions calculated from measurements (dark solid line) or modeled emissions (dashed line) at 4.0 km downwind. Error bars represent ceilometer's measurement uncertainty or modeling uncertainty.

Before comparing the dispersion model results to measured $PM_{2.5}$ ground concentrations, the uncertainty within the ground measurements was studied. The two sets of measurements by AeroTrak and TEOM were compared against each other. The AeroTrak measurements against TEOM measurements had a correlation, *R*, of 0.83 (Figure 2.7). The correlation between the two AeroTraks was 0.98.

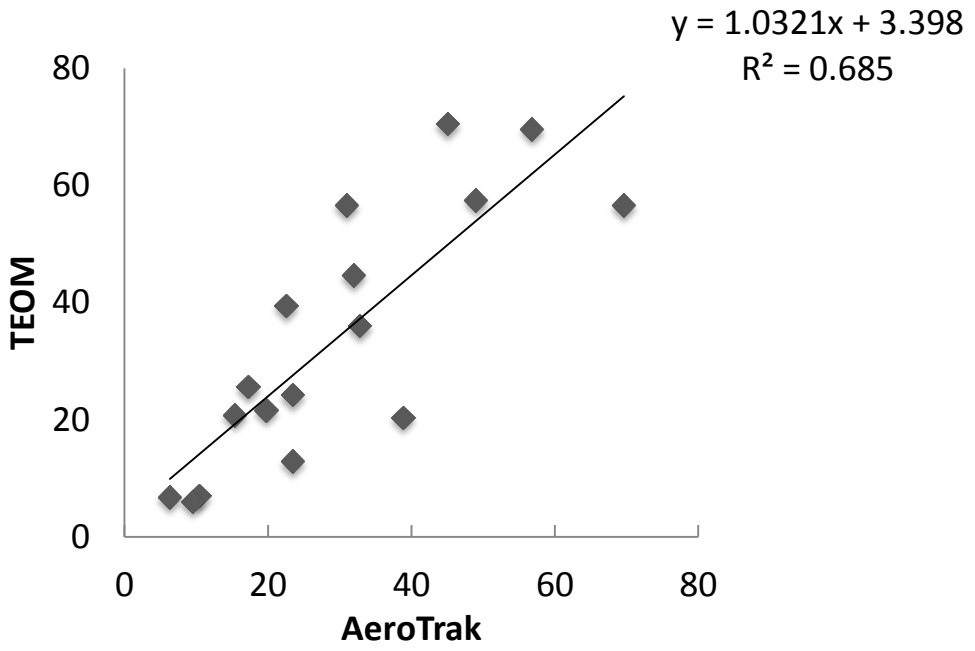

Figure 2.7: The 10-min-average concentrations (μg m^{-3}) derived from AeroTrak particle counter compared with TEOM measurements.

Time series comparison of the two sets of Daysmoke-simulated ground level $PM_{2.5}$ concentrations against the measurements are shown in Figure 2.8. The $PM_{2.5}$ concentration measurements taken 4.0 km downwind showed that the concentration increased from the background level due to the smoke for the first two hours after ignition. Similar to plume height, the concentration at 4.0 km away from the fire started increasing at 1330 CST. Mobile 2 was busy chasing for the plume for the first half of the simulation; therefore the measurements were only collected after 1310 CST at 9.2 km downwind. As the wind shifted direction, the plume shifted away from the measurement sites. Therefore the measured $PM_{2.5}$ concentrations at both measurement sites started decreasing after 1400 CST. Daysmoke simulations were able to capture this shift due to changing wind direction, and the simulated ground concentrations decreased around the

same time as the measurements did. RMSE and MFE of Daysmoke predictions using emissions calculated from the field measurements (labeled as measured emis.-Dsmk) at 4.0 km downwind against 14 ten-minute averages of TEOM measurements were 14.5 μg m^{-3} and 45%, and against 14 averages of AeroTrak measurements were 12.8 μg m^{-3} and 37%. The difference in MFE with respect to measurement discrepancy by TEOM and AeroTrak was only 8%. Daysmoke with measurement-derived emissions showed a decrease in $PM_{2.5}$ concentration measured at Mobile 2 site. RMSE and MFE against nine averages of AeroTrak measurements were 12.2 μg m^{-3} and 46%, respectively.

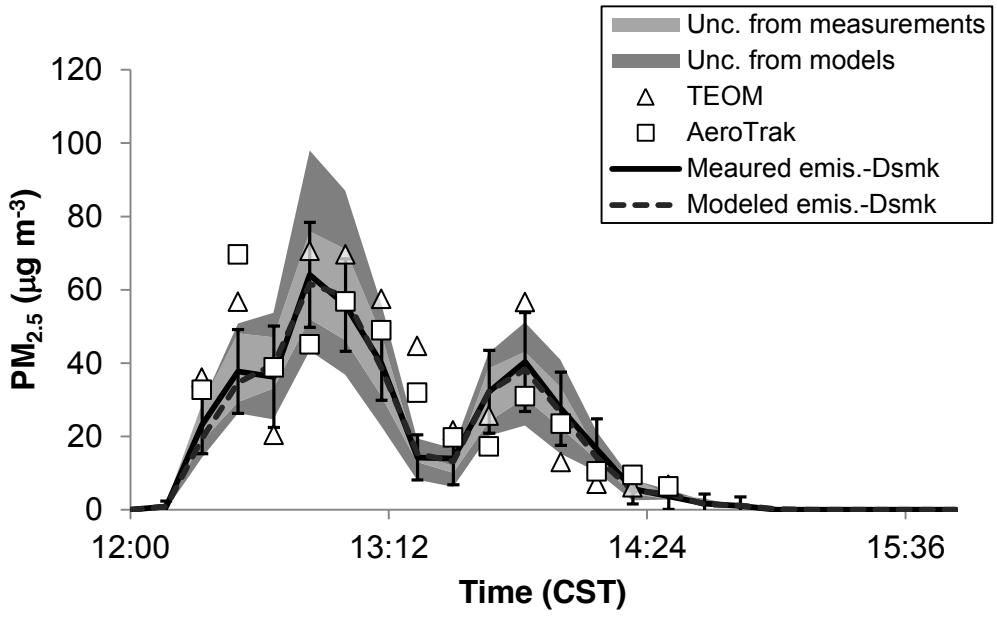

(a)

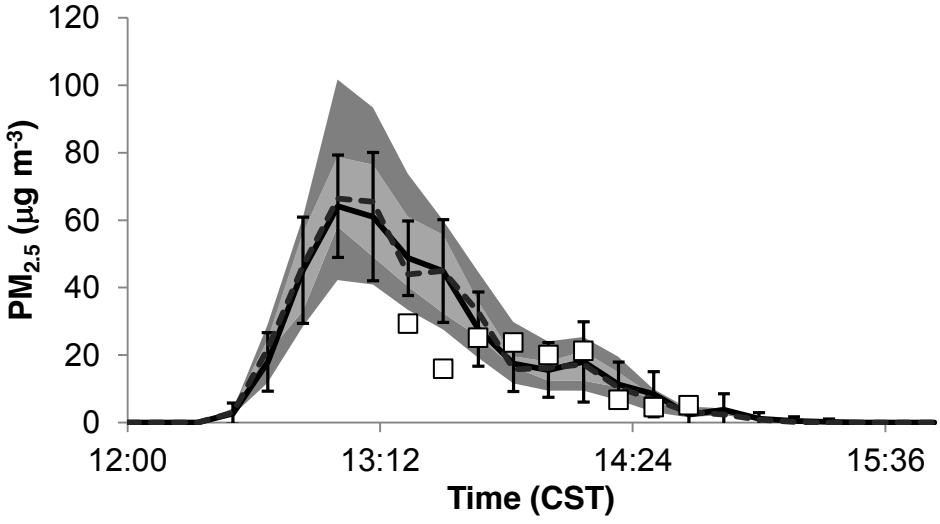

(b)

Figure 2.8: Comparison of 10-minute average ground concentration predictions with measurements at 4.0 km (a) and 9.2 km (b) away from the burn. The lines show the mean of 40 Daysmoke runs using measurement-derived emissions (solid) and modeled emissions (dotted). Shaded areas are the uncertainty ranges due to the uncertainty in measured emission variables (light grey) and due to modeled emission variability (dark grey). Error bars show the concentration standard deviations from the 40 Daysmoke runs with measurement-derived emissions.

2.4.2 Uncertainty Analysis

Measured and modeled fuel loadings were different only by 11% (Table 2.2). Estimating fuel loading and fuel consumption is usually one of the most difficult parts in estimating emissions. However, since the burn unit in this study had a relatively small amount of fuel with very little coarse woody debris and duff, the fuel loading and fuel consumption were estimated with great accuracy (Table 2.1 and Table 2.2). For other cases, the uncertainty associated with fuel loading can be much larger [*Keane*, 2012]. The greatest difference between modeled and measured variables out of the three studied was in fuel consumption (Table 2.2). The net difference between the modeled and the measured total emissions was 7%. The RMSE and MFE of Daysmoke simulations against the AeroTrak measurements averaged for both measurement sites are shown in Table 2.5. The modeled emissions case has 7% larger total emissions and 3% higher plume height than the measurement-derived emissions case. The Daysmoke predicted ground level $PM_{2.5}$ concentrations using modeled emissions were closer to the observations with 2% lower MFE than the concentrations predicted using measurement-derived emissions.

Daysmoke's stochastic formulation led to a large variability in simulated ground level concentrations. The bars in Figure 2.8 represent the standard deviation of 40 Daysmoke predictions with the same emission inputs at a particular time. The standard deviation represents, in part, the uncertainty inherent to turbulence. Daysmoke's standard deviation at these two sites was usually half of estimated $PM_{2.5}$ concentrations and was as large as 19.0 $\mu g\ m^{-3}$ for concentrations around 20 $\mu g\ m^{-3}$. Daysmoke's standard deviation

was as large as or even larger than the uncertainties from input emissions (the grey shaded areas in Figure 2.8) especially at lower concentrations.

Table 2.5: Root mean squared error (RMSE) and mean fractional error (MFE) of Daysmoke $PM_{2.5}$ predictions with measurement-based emissions (top row) and model-based emissions (bottom row) against both sets of AeroTrak measurements, total input emission uncertainties and their effect on ground concentration uncertainties.

	Error against AeroTrak		Total emission uncertainty	Uncertainty in ground concentration due to emissions uncertainty	
	RMSE ($\mu g\ m^{-3}$)	MFE (%)	(kg)	RMSE ($\mu g\ m^{-3}$)	MFE (%)
Daysmoke-Measured	14.0	44	Std. error 1.02×10^4 (18%)	7.3	20
Daysmoke-Modeled	13.0	42	Std. dev. 2.20×10^4 (36%)	14.4	42

Uncertainty introduced in total $PM_{2.5}$ emissions due to fuel consumption and emission factor measurement uncertainties was 1.02×10^4 kg, or 18% of the total emissions (Table 2.5). The effect of emission measurement uncertainty in Daysmoke concentration simulation (lighter grey in Figure 2.8) is 7.3 $\mu g\ m^{-3}$ in the RMSE and 20% in the MFE. Uncertainty in total emissions due to modeling uncertainty was calculated from the differences in modeled and measured values listed in Table 2.2. The difference between the modeled and the measured values increased from fuel loading to fuel consumption, but decreased for emission factor. The difference in fuel consumption (0.07 $kg\ m^{-2}$) and the difference in emission factor (1 $g\ kg^{-1}$ plus one standard deviation of 3.4 $g\ kg^{-1}$) led to 2.20×10^4 kg difference in total emissions (36% of total emissions). The difference in total emissions was larger than the field measurement uncertainty. The emissions modeling variability affected Daysmoke predictions (darker grey in Figure 2.8)

by RMSE of 14.4 μg m^{-3} and MFE of 42%, which is almost twice as large as the uncertainty introduced by measurements.

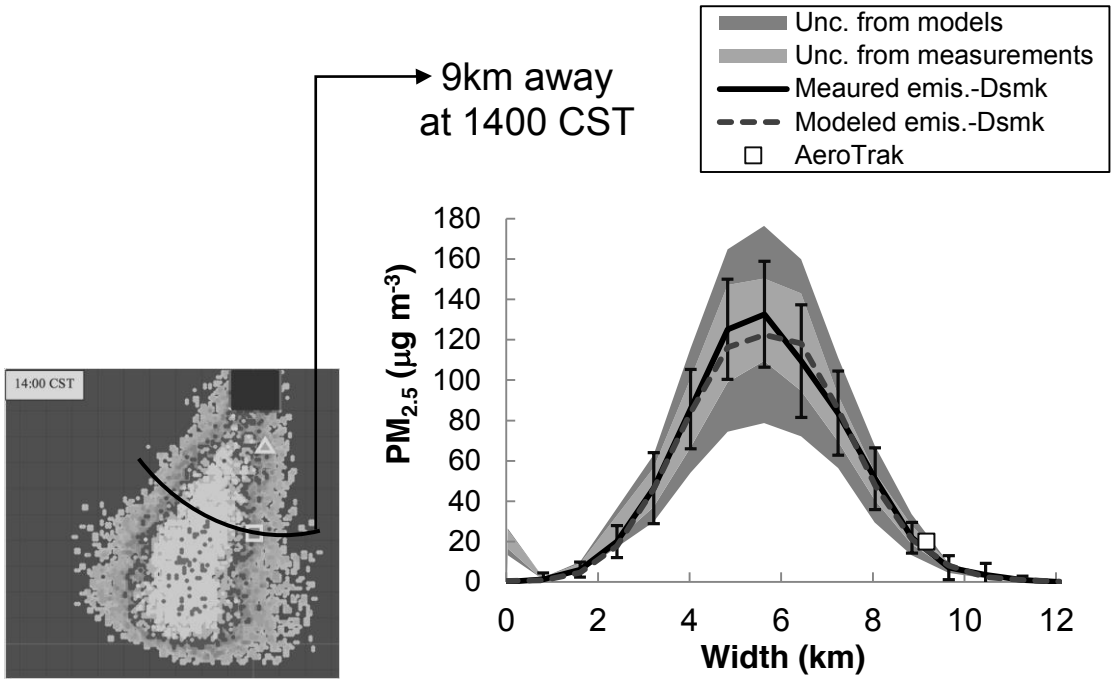

Figure 2.9: Bird's eye view from Daysmoke at 1400 CST on 8 February 2011 (left) with an arc representing where the cross sectional analyses were performed. Comparison of 10-minute averaged ground concentration predictions with measurements at 1400 CST, 9.2 km (right) away from the burn. The lines show the mean of 40 Daysmoke runs using measurement-derived emissions (solid) and modeled emissions (dotted). Shaded areas are the uncertainty ranges due to the uncertainty in measured emission variables (light grey) and due to modeled emission variability (dark grey). Error bars show the concentration standard deviations from the 40 Daysmoke runs with measurement-derived emissions.

It can be seen from the snapshot of the plume at 1400 CST (Figure 2.9) that the measurements were sometimes taken at the edge of the plume due to the plume rotating. Similar uncertainty analyses were also conducted across the plume for the duration of the burn at 9.2 km downwind. An example analysis at 1400 CST is show in Figure 2.9. As expected, the concentration increased towards the center of the plume. Simulations using modeled emissions led to slightly lower concentrations. Uncertainty in ground

concentration introduced from emission measurement uncertainty could be as large as 24.1 μg m^{-3} at the center of the plume. Uncertainty in ground concentration due to modeled emission variability could be even larger, 48.9 μg m^{-3}. Daysmoke's standard deviation was at times as large as 27.9 μg m^{-3} at the center of the plume, but was only 26% of predicted concentration at the center of the plume. Although Daysmoke's standard deviation was larger than the uncertainty in ground concentrations due to measurement and modeling uncertainty in emissions at the edge of the plume, the dispersion model's standard deviation was smaller than the uncertainty from the emissions near the center of the plume. Therefore, measurement and modeling uncertainties in emissions are just as important as inherent Daysmoke uncertainty due to turbulence.

2.5 Conclusion

Uncertainties in fuel loading, fuel consumption, emission factors, and their effect on simulated ground concentrations were analyzed in the present study. In this case study, the models predicted fuel loading and fuel consumption within 15% of measured values. Although the previously published emission factors applicable for the study area ranged from 6.9 to 19 g kg^{-1}, their mean was only 7% lower than the emission factor measured in our study. The calculated total $PM_{2.5}$ emissions from modeled values differed from the measured emissions values by 7%. Daysmoke results had a large uncertainty due to the meteorological and model related uncertainties. By adjusting the WRF-simulated wind speed and wind direction with the field-measured values, the errors introduced through meteorological inputs were minimized. The dispersion model's performance was evaluated by comparing plume heights and downwind smoke

concentrations against measurements. Simulated plume heights had a slightly low bias compared to the measurements and MFE of 16%. Daysmoke was able to predict the ground concentrations with a RMSE of 14.5 $\mu g\ m^{-3}$.

Variability in modeled emissions was larger than measurement uncertainty. Measurement uncertainties in fuel loading, fuel consumption, and emission factor were combined using propagation of error and resulted in 18% uncertainty in total $PM_{2.5}$ emissions. The differences between the modeled and measured values in fuel loading, fuel consumption, emission factor, and the large variability in modeled emission factors led to a 36% uncertainty in modeled total emissions. Measurement uncertainty in the input emissions led to 20% uncertainty in simulated $PM_{2.5}$ concentrations, and variability in modeled emissions led to 42% concentration uncertainty. Predicted concentrations and emission-related uncertainties increased towards the center of the plume. This study found that uncertainty derived from input emissions had a greater contribution to the overall uncertainty in concentrations predicted by the smoke dispersion model when compared with the model's inherent uncertainty attributed to the stochastic nature of turbulence.

Fire emission uncertainties had a significant influence on plume transport and downwind $PM_{2.5}$ concentration predictions, Future studies should investigate if downwind smoke predictions, with Daysmoke or other models, for various burns are subject to similar levels of uncertainty due to emission uncertainties. While existing fire and plume transport models are useful for predicting smoke impacts downwind, practitioners of prescribed burning should make firing decisions considering the

magnitude of uncertainties associated with concentration predictions due to various sources of uncertainty in emissions.

2.6 References

Achtemeier, G. (2008), Effects of Moisture Released during Forest Burning on Fog Formation and Implications for Visibility, *Journal of Applied Meteorology and Climatology*, *47*(5), 1287-1296, doi:10.1175/2007JAMC1721.1.

Achtemeier, G., S. Goodrick, and Y. Liu (2012), Modeling Multiple-Core Updraft Plume Rise for an Aerial Ignition Prescribed Burn by Coupling Daysmoke with a Cellular Automata Fire Model, *Atmosphere*, *3*(3), 352-376.

Achtemeier, G., S. Goodrick, Y. Liu, F. Garcia-Menendez, Y. Hu, and M. T. Odman (2011), Modeling Smoke Plume-Rise and Dispersion from Southern United States Prescribed Burns with Daysmoke, *Atmosphere*, *2*(3), 358-388, doi:10.3390/atmos2030358.

Anderson, G., D. Sandberg, and R. Norheim (2004), Fire Emission Production Simulator (FEPS) User's Guide, *1.0*.

Andrews, P. L., C. D. Bevins, and R. C. Seli (2003), *BehavePlus Fire Modeling System: Version 2.0: User's Guide*, US Department of Agriculture, Forest Service, Rocky Mountain Research Station.

Aurell, J., and B. K. Gullett (2013), Emission Factors from Aerial and Ground Measurements of Field and Laboratory Forest Burns in the Southeastern U.S.: PM2.5, Black and Brown Carbon, VOC, and PCDD/PCDF, *Environmental Science & Technology*, *47*(15), 8443-8452, doi:10.1021/es402101k.

Boylan, J. W., and A. G. Russell (2006), PM and light extinction model performance metrics, goals, and criteria for three-dimensional air quality models, *Atmospheric Environment*, *40*(26), 4946-4959, doi:http://dx.doi.org/10.1016/j.atmosenv.2005.09.087.

Brown, J. K. (1974), *Handbook for inventorying downed woody material*, Intermountain Forest and Range Experiment Station Ogden, Utah.

Fernandes, P. M., G. M. Davies, D. Ascoli, C. Fernández, F. Moreira, E. Rigolot, C. R. Stoof, J. A. Vega, and D. Molina (2013), Prescribed burning in southern Europe: developing fire management in a dynamic landscape, *Frontiers in Ecology and the Environment*, *11*(s1), e4-e14, doi:10.1890/120298.

French, N., P. Goovaerts, and E. Kasischke (2004), Uncertainty in estimating carbon emissions from boreal forest fires, *Journal of Geophysical Research-Atmospheres*, *109*(D14), doi:10.1029/2003jd003635.

Garcia‐Menendez, F., Y. Hu, and M. T. Odman (2013), Simulating smoke transport from wildland fires with a regional‐scale air quality model: Sensitivity to uncertain wind fields, *Journal of Geophysical Research: Atmospheres*, *118*(12), 6493-6504, doi:10.1002/jgrd.50524.

GoogleEarth7.1 (2013), Eglin Air Force Base, Florida USA 30°38'46.17"N, 86°16'36.03"W, elevation 52M.

Grandesso, E., B. Gullett, A. Touati, and D. Tabor (2011), Effect of Moisture, Charge Size, and Chlorine Concentration on PCDD/F Emissions from Simulated Open Burning of Forest Biomass, *Environmental Science & Technology*, *45*(9), 3887-3894, doi:10.1021/es103686t.

Holton, J. R. (2004), *An Introduction to Dynamic Meteorology*, Fourth ed., 129-131 pp., Elsevier/Academic Press, London.

Hu, Y., M. T. Odman, M. E. Chang, W. Jackson, S. Lee, E. S. Edgerton, K. Baumann, and A. G. Russell (2008), Simulation of air quality impacts from prescribed fires on an urban area, *Environmental Science & Technology*, *42*(10), 3676-3682.

Jain, R., J. Vaughan, K. Heitkamp, C. Ramos, C. Claiborn, M. Schreuder, M. Schaaf, and B. Lamb (2007), Development of the ClearSky smoke dispersion forecast system for agricultural field burning in the Pacific Northwest, *Atmospheric Environment*, *41*(32), 6745-6761, doi:10.1016/j.atmosenv.2007.04.058.

Keane, R. E. (2012), Describing wildland surface fuel loading for fire management: a review of approaches, methods and systems, *International Journal of Wildland Fire*.

Larkin, N. K., S. M. O'Neill, R. Solomon, S. Raffuse, T. Strand, D. C. Sullivan, C. Krull, M. Rorig, J. Peterson, and S. A. Ferguson (2009), The BlueSky smoke modeling framework, *International Journal of Wildland Fire*, *18*(8), 906-920, doi:http://dx.doi.org/10.1071/WF07086.

Laursen, K. K., R. J. Ferek, P. V. Hobbs, and R. A. Rasmussen (1992), Emission factors for particles, elemental carbon, and trace gases from the Kuwait oil fires, *Journal of Geophysical Research: Atmospheres*, *97*(D13), 14491-14497, doi:10.1029/92jd01370.

Liu, Y., S. Goodrick, G. Achtemeier, K. Forbus, and D. Combs (2013), Smoke plume height measurement of prescribed burns in the south-eastern United States, *International Journal of Wildland Fire*, *22*(2), 130-147, doi:http://dx.doi.org/10.1071/WF11072.

Liu, Y., S. Goodrick, G. Achtemeier, W. A. Jackson, J. J. Qu, and W. Wang (2009), Smoke incursions into urban areas: simulation of a Georgia prescribed burn, *International Journal of Wildland Fire*, *18*(3), 336-348, doi:http://dx.doi.org/10.1071/WF08082.

Mercer, G., and R. Weber (2001), Fire Plumes, in *Forest fires : behavior and ecological effects*, edited by E. A. Johnson and K. Miyanishi, pp. 229-251, Academic Press, Inc., San Diego, Calif.

Montiel, C., and D. T. Kraus (2010), *Best Practices of Fire Use: Prescribed Burning and Suppression: Fire Programmes in Selected Case-study Regions in Europe*, European Forest Institute.

Ottmar, R., R. Vihnanek, and J. Mathey (2003), Stereo photo series for quantifying natural fuels. Volume VIa: sand hill, sand pine scrub, and hardwood with white pine types in the Southeast United States with supplemental sites for Volume VI. , edited, p. 78, National Wildfire Coordinating Group, National Interagency Fire Center, Boise, ID.

Ottmar, R. D. (2014), Wildland fire emissions, carbon, and climate: Modeling fuel consumption, *Forest Ecology and Management*, *317*, 41-50.

Pouliot, G., T. Pierce, W. Benjey, S. M. O'Neill, and S. A. Ferguson (2005), Wildfire emission modeling: integrating BlueSky and SMOKE, paper presented at 14th Annual Emissions Inventory Conference, Las Vegas, Nevada, April 11 - 14, 2005.

Prichard, S., R. Ottmar, and G. Anderson (2007), Consume 3.0 user's guide and scientific documentation, edited by U. F. Service, Pacific Wildland Fire Sciences Laboratory, Seattle.

Reid, J., R. Koppmann, T. Eck, and D. Eleuterio (2005), A review of biomass burning emissions part II: intensive physical properties of biomass burning particles, *Atmospheric Chemistry and Physics*, *5*(3), 799-825.

Seiler, W., and P. Crutzen (1980), Estimates of gross and net fluxes of carbon between the biosphere and the atmosphere from biomass burning, *Climatic Change*, *2*(3), 207-247, doi:10.1007/BF00137988.

Skamarock, W. C., J. B. Klemp, J. Dudhia, D. O. Gill, D. M. Barker, M. G. Duda, X.-Y. Huang, W. Wang, and J. G. Powers (2008), A description of the Advanced Research WRF version 3, Tech. Note, NCAR/TN-475+STR*Rep*., Natl. Cent. for Atmos. Res., Boulder, Colorado, USA.

Stevens, W. R., W. Squier, W. Mitchell, B. K. Gullett, and C. Pressley (2013), Measurement of Motion Corrected Wind Velocity Using an Aerostat Lofted Sonic Anemometer, *Atmospheric Measurement Techniques*, *in press*.

Tian, D., Y. Hu, Y. Wang, J. W. Boylan, M. Zheng, and A. G. Russell (2008), Assessment of biomass burning emissions and their impacts on urban and regional PM2. 5: A Georgia case study, *Environmental Science & Technology*, *43*(2), 299-305.

Urbanski, S., W. Hao, and B. Nordgren (2011), The wildland fire emission inventory: western United States emission estimates and an evaluation of uncertainty, *Atmospheric Chemistry and Physics*, *11*(24), 12973-13000, doi:DOI 10.5194/acp-11-12973-2011.

Urbanski, S. P., W. M. Hao, and S. Baker (2008), Chemical composition of wildland fire emissions, *Developments in Environmental Science*, *8*, 79-107.

US-EPA (1995), Compilation of Air Pollutant Emission Factors, AP-42, fifth Edition, Vol. 1: Stationary Point and Area Sources*Rep*. *2060-AP63*, 13.11 17 pp, U.S. Environmental Protection Agency, Research Triangle Park, NC.

US-EPA (2013), The 2011 National Emissions Inventory, edited, US-EPA.

Weise, D. R., and C. S. Wright (2014), Wildland fire emissions, carbon and climate: Characterizing wildland fuels, *Forest Ecology and Management*, *317*, 26-40.

Wiedinmyer, C., B. Quayle, C. Geron, A. Belote, D. McKenzie, X. Y. Zhang, S. O'Neill, and K. K. Wynne (2006), Estimating emissions from fires in North America for air quality modeling, *Atmospheric Environment*, *40*(19), 3419-3432, doi:10.1016/j.atmosenv.2006.02.010.

Wilson, J., and B. Sawford (1996), Review of Lagrangian stochastic models for trajectories in the turbulent atmosphere, *Boundary-Layer Meteorol*, *78*(1-2), 191-210, doi:10.1007/BF00122492.

CHAPTER 3

Prescribed Burning Plume Dispersion Simulation in an Air Quality Model using Ground and Satellite Data[1]

Abstract

Fire emissions are often predicted using site-specific ground observations, however it is difficult to detect fire spread. Satellites can detect fire spread; however temporal filtering applied to reduce false fire detection can lead to an underestimation of emissions from short, small fires. $PM_{2.5}$ emission rates from a prescribed burn were estimated by two methods: one using ground measurements and the other using satellite data. Redistribution of emissions from site-specific ground measurements by fractional emission rate derived from satellite retrievals was also studied. Daysmoke was used to simulate the three sets of emission rates, which were compared to measurements taken by aircraft during a prescribed burn. The ground-based approach estimated more $PM_{2.5}$ emissions, while the satellite-based approach had the similar plume shape to what the aircraft measured. The emission rate derived from assimilation of ground and satellite data simulated plume rise and downwind concentration was closest to the aircraft measurements.

This chapter will be submitted to Geophysical Research Letters. Co-authors are Yongtao Hu, Armistead Russell, M. Talat Odman, David Lavoue, Robert Yokelson, Shawn Urbanski, Xiaoyang Zhang, Fernando Garcia-Menendez

3.1 Introduction

Biomass burning (including wildfire and prescribed burning) affects climate and air quality by emitting trace gases, $PM_{2.5}$ (i.e. particulate matter less than 2.5 μm in aerodynamic diameter), species that can lead to $PM_{2.5}$, ozone, and other harmful pollutants [*Crutzen and Andreae*, 1990]. Emissions from biomass burning are expected to increase with change in climate [*Stocks et al*., 1998; *Westerling et al*., 2006]. One way to reduce wildfire risk is by performing prescribed burning. Prescribed burning not only consumes accumulated wildland fuels, but also restores and maintains ecosystems that benefit from fire. Although prescribed burnings are controlled, the emitted smoke can travel to nearby populated areas and cause regional haze and air quality deterioration [*Hu et al*., 2008]. United States Environmental Protection Agency (EPA) 2011 National Emission Inventory [2013] reported that 15% (8.4×10^8 kg) of $PM_{2.5}$ emissions in the United States (US) are attributed to prescribed burnings.

Fire emissions are frequently estimated using bottom-up approach with inventories of previous ground measurements. Models such as Photo Series [Ottmar et al., 2000] and the Fuel Characteristic Classification System (FCCS) [*Prichard et al*., 2013] use previously recorded data to predict fuel loadings. First Order Fire Effects Model (FOFEM) [*Reinhardt et al*., 1997], Behave Plus [*Andrews et al*., 2003], and Consume [*Prichard et al*., 2007] are some of the commonly used fuel consumption models that have recorded fuel loadings or takes in the results from fuel loading models to calculate consumption and emissions based on environmental parameters that users define. Many measurements taken on site throughout the US have been combined in these models. These models have the capability of predicting fuel consumption and

emissions accurately if the fuel types and environmental parameters are accurate. The down side to predicting emissions using measurements at ground level is that data is not available for sites that have not been studied.

Biomass burning emissions can also be estimated using data retrieved from satellites. The global Fire Emissions Database (GFED) [*van der Werf et al*., 2010], the Global Fire Assimilation System (GFAS) [*Kaiser et al*., 2012], the Fire Locating and Modeling of Burning Emissions (FLAMBE) [Reid et al., 2009], the Fire Inventory from NCAR (FINN) [*Wiedinmyer et al*., 2011], and GBBEP-Geo [*Zhang et al*., 2012] are some of the biomass burning emissions inventories derived from satellite-derived data, such as fire pixel count, burn area, and fire radiative power (FRP). These methods partially follow the bottom-up approach and incorporate emission factors to calculate fire emissions [*Ichoku and Ellison*, 2013]. Biomass burning emission inventories derived from satellite data can be created for any location and do not require on-site measurements. Satellites can detect temporal burn rate, with one-hour increments from the GOES biomass burning emission algorithm [*Zhang et al*., 2012]. Some studies found that this bottom-up approach with satellite data result in a severe underestimates of PM emissions [*Ichoku and Ellison*, 2013; *Kaiser et al*., 2012; *Liousse et al*., 2010; *Petrenko et al*., 2012]. *Petrenko et al*. [2012] found that burned area estimates are usually the largest source of disagreement between satellite derived emissions and other inventories. Small, short biomass burning events are often not captured by the satellites, or the temporal filtering used in The Wildfire Automated Biomass Burning Algorithm (WF_ABBA), which uses geostationary satellite data to detect and characterize biomass burning, may lead to an underestimate in fuel consumed [Petrenko et al., 2012]. Also, limited emission

factors that can be applied to wide range of fuel types are used in the emission algorithms using satellite retrievals [Ichoku and Ellison, 2013].

Both methods to predict fire emissions have pros and cons, and combining the two datasets may reduce error in emissions. *Sofiev et al*. [2009] estimated emission rates by using both ground measurements and satellite retrieval for larger fires where the burn events lasted for more than a week. This study applies a similar approach but focuses on a smaller and shorter biomass burning event where the discrepancy in emissions calculated by the two methods is known to be severe. This study compares the $PM_{2.5}$ emissions estimated by ground measurements to the emissions estimated by satellite retrievals for a prescribed burning case. Hybrid of the two methods, where the total $PM_{2.5}$ emissions from the ground measurements were redistributed with fractional emission rates from the satellite method, was also studied. Differences in emission rates and their importance on plume behavior were examined through plume dispersion and chemical transport models.

3.2 Burn Description

The Williams prescribed fire (34.6958N, 120.2064W) occurred on a hillside with 81 hectares of coastal sage shrub in southern California on 17 November 2009. The case was chosen since satellites detected the burn and various airborne data were collected during the burn event. The burn started at 1000 LST and lasted for 4.5 hours. Live and dead fuel moistures and ground level relative humidity were below average. The top of the boundary layer was reported to be 450 m above ground, which allowed the bulk of the smoke to be buoyancy driven and penetrate the temperature inversion layer. Most of the plume traveled to the northeast at higher altitudes, but small portion of the plume at

lower altitudes traveled to the southeast from the burn site. Additional details of the burn conditions are in Akagi et al. [2012].

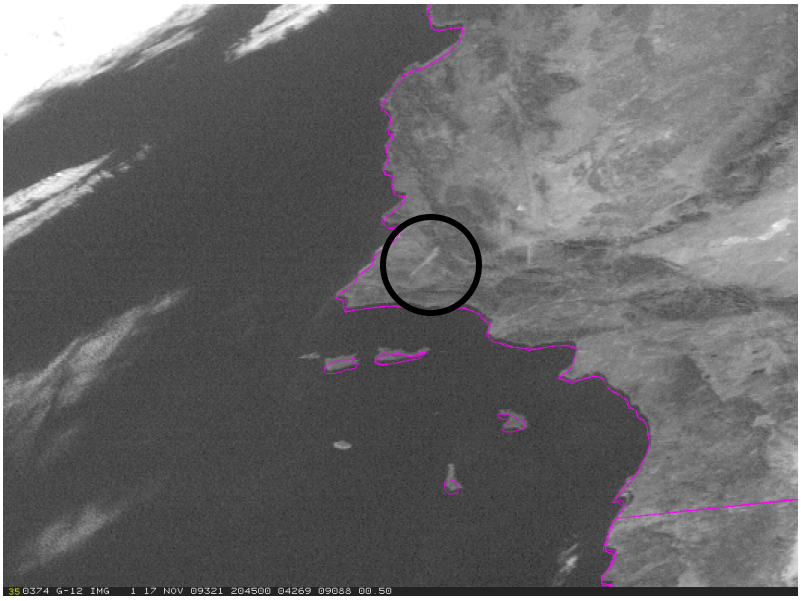

Figure 3.1: GOES12 VIS image at 1245 LST (2045Z). Williams Fire smoke plume circled in black.

The US Forest Service (USFS) Twin Otter aircraft was used to fly through the smoke plume. The aircraft measured meteorological data and concentrations of trace gases and particles [*Akagi et al*., 2012; *Burling et al*., 2011]. Wind speed and wind direction were measured every second. $PM_{2.5}$ concentration inside the plume was derived from dry particle light scattering coefficient (bscat) that was measured every other second. The factor to convert bscat to $PM_{2.5}$ concentration is obtained by a gravimetric calibration; as explained in detail by *Akagi et al*. [2012]. Since the conversion factor was derived for a freshly emitted smoke, the factor was suitable for smoke plumes near the burn site. This study used the data from the first flight, flying between 1019 LST to 1311 LST, which hovered near the burn site and traveled up to 20 km downwind.

3.3 Methods

The modeling system developed for this study requires multiple models with two main components; emissions modeling and plume dispersion/transport modeling. Figure 3.2 shows the required variables, the models used to obtain them, and how they are linked to one another. The differences in ground-based and satellite-based approaches are shown in different colored arrows, as well as explained in the following sections.

Bottom-up emission calculation approach often follows the following equation [*Seiler and Crutzen*, 1980]:

$$E = \mathrm{A} \times \mathrm{FL} \times \mathrm{C} \times \mathrm{EF} \quad (1)$$

where the emission (E) can be calculated by multiplying the area burned (A) by the mass of vegetation available to burn per unit area (FL), consumption efficiency (C), and an emission factor (EF; mass of compound emitted per mass of burned vegetation). Fuel loading and combustion efficiency is often combined and referred to as fuel consumption.

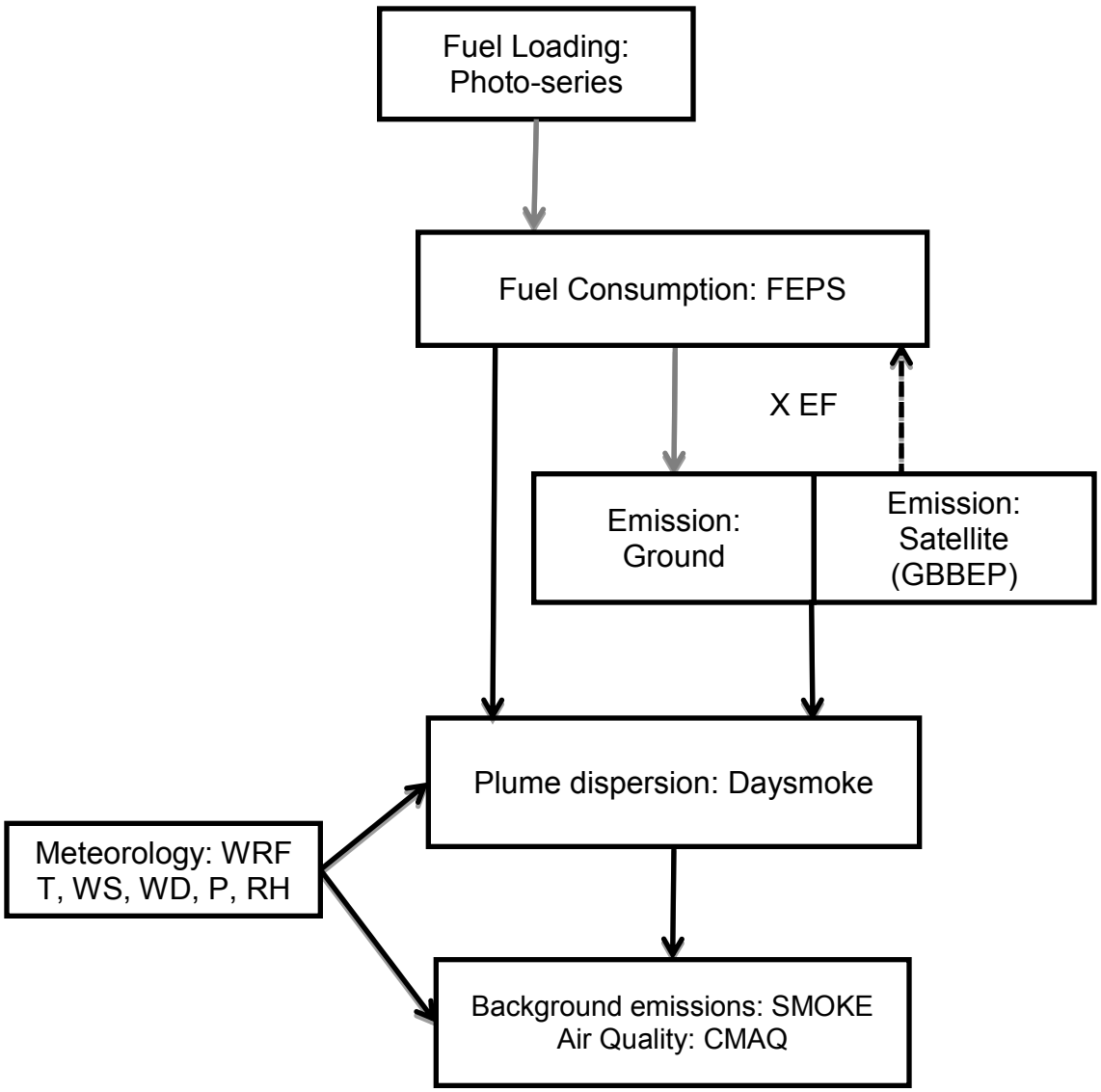

Figure 3.2: Framework used to simulate fire emissions and its dispersion and transport. Grey line represents the path used for ground measurement based emissions and dotted line shows the path taken to obtain fuel consumption.

3.3.1 Ground-Based Emissions

Fuel loading was obtained from the USFS Pacific Northwest Research Station's Photo Series (http://depts.washington.edu/nwfire/dps/). The Photo Series is an inventory of previously measured, site-specific fuel and vegetation conditions [Ottmar et al., 2000]. The Digital Photo Series allows the user to interact with the map of continental US, and

obtain fuel-loading information with an image of each measurement site. Akagi et al. [2012] classified the burned fuels as coastal sage shrub. Since the age of the fuel was unknown, aggregation of Series IV CH: SW US Chaparral CH1 (age 30yr), CH2 (14yr), & CH3 (18yr) (SRM205) was used. Individually, these have fuel loadings (tons/acre) of 6.7, 7.9, 9.6 for shrubs and 3.8, 16.5, 7.4 for litter. The averages, 8.1 ton/acre for shrubs and 9.2 ton/acre for litter, were used to calculate fuel consumption.

Fuel consumption was calculated by a fire emission model called Fire Emission Production Simulator (FEPS) [*Anderson et al*., 2004]. Fuel moisture for wet and dry fuels, area burned, duration of the burn, and other meteorological conditions mentioned in *Akagi et al*. [2012] were included in FEPS. All of the reported area was assumed to have burned. Although FEPS already contains a database of typical fuels, the fuel loading section was modified to include values from the Photo Series. For the ground-based approach, the total area burned was linearly interpolated for the duration of the burn using the default setting. Hourly flaming and smoldering fuel consumption rates from FEPS were multiplied by the $PM_{2.5}$ emission factor specific to this burn case to calculate $PM_{2.5}$ emission rates for the ground-based approach. *Burling et al*. [2011] derived emission factors from the data collected by the aircraft and found the $PM_{2.5}$ emission factor to be 8.59 g/kg, which was the emission factor used in this study. Hourly heat release, another output from FEPS, was used for plume dispersion modeling (explained in 3.3.4 Plume Dispersion Modeling).

3.3.2 Satellite-Based Emissions

Williams fire emissions were also calculated using the Global Biomass Burning Emission Product (GBBEP, ftp://satepsanone.nesdis.noaa.gov/EPA/GBBEP/) [*Zhang et*

al., 2008]. GBBEP derives fire emissions from satellite-retrieved vegetative fuel loading, fuel moisture, and burned area. Fuel loading is calculated from Moderate-Resolution Imaging Spectroradiometer (MODIS) data including land cover type, vegetation field, and monthly leaf area index. Fuel combustion efficiency and emission factor are selected based on ecological region and fuel moisture category retrieved from the Advanced Very High Resolution Radiometer (AVHRR) Global Vegetation Index (GVIx). Fire sizes obtained from the Geostationary Operational Environmental Satellites (GOES) Wildfire Automated Biomass Burning Algorithm (WF_ABBA) are used to determine the fire spread rate. Integration of these parameters results in hourly $PM_{2.5}$ emissions calculated for each individual fire [Zhang et al., 2008].

GBBEP from Geostationary satellites (GBBEP-geo), the most current version [*Zhang et al*., 2012], uses Fire Radiative Power (FRP) from multiple Geostationary satellites. Because the study case occurred before GBBEP-geo was available, the products from the earlier version were used. Satellites detected a fire at 34.7N, 120.23W on the day of the burn. GBBEP used the $PM_{2.5}$ emission factor for shrubs, 10.6 g/kg [*Zhang et al*., 2008], and reported hourly $PM_{2.5}$ emissions. Since GBBEP follows Equation (1) to derive emission rates, the hourly fuel consumption for the satellite-based approach was assumed to be the emission rate divided by the emission factor hence the upward arrow in Figure 3.2. Heat release for the satellite-based approach was calculated in FEPS by controlling the fuel loading profile and burn area rates to match the hourly fuel consumption for the satellite case. All other parameters remained the same as ground-based case.

3.3.3 Hybrid Emissions

The third set of emission rates combines the benefits of the two previous methods. Total emissions from the ground-based approach were redistributed by satellite retrieved fractional emission rates. The hybrid emission rates were divided by the measurement-derived $PM_{2.5}$ emission factor to obtain hourly fuel consumption. For hybrid heat release rates, fuel loadings in FEPS were manipulated until the calculated hybrid hourly fuel consumption rates matched with the output fuel consumption rates in FEPS.

3.3.4 Plume Dispersion Modeling

The simulation of plume transport was done using Daysmoke, an empirical-stochastic Lagrangian plume dispersion model designed for prescribed burnings. Daysmoke consists of entraining turret model that calculates plume pathway and a particle trajectory model that simulates smoke transport through the plume pathway [*Achtemeier et al*., 2011]. Daysmoke requires $PM_{2.5}$ emission rates, total burn area, gridded meteorological data, and a plume core number. The core number was set as two in accordance with Figure 3.3, where the plume shows a split into two: one at upper altitude and the other at lower altitude.

Figure 3.3: A photograph of the high- and low-altitude smoke plumes from the Williams Fire taken at 12:20 LT on 17 November 2009 from the USFS Twin Otter aircraft, reprinted with permission from Akagi et al. [2012].

Daysmoke also requires the initial effective plume diameter derived from heat release rate. The hourly heat release (Q) from FEPS was used to calculate the effective fire diameter (D_o):

$$w_o D_o^2 = \frac{4Q}{\pi C_p \rho \Delta T_o} \quad (2)$$

where w_0 is the vertical velocity entering the plume (m s^{-1}), C_p is the specific heat (J kg^{-1} K^{-1}), ρ is the air density (kg m^{-3}), and ΔT_0 is the temperature difference between the plume air and ambient conditions. The default value of ΔT_0, 40 K, was used. The plumes were driven by buoyancy; therefore the vertical velocity entering the plume was adjusted accordingly. An increase in initial fire diameter decreases the impact of plume entrainment [*Achtemeier et al*., 2011] and leads to the plume to be buoyancy driven. With conservation of heat flux, the initial vertical wind velocity was reduced to 3 m s^{-1} to

obtain a larger initial fire diameter. Daysmoke simulates the location of each particle that represents 1 kg of $PM_{2.5}$, which are reported every 15 minutes, and those particles were converted to concentration using an air quality model described below.

Meteorological parameters required for plume dispersion modeling were predicted by the Weather Research and Forecasting Model (WRF) [Skamarock et al., 2008] using Unified Noah land-surface model, YSU boundary layer scheme, and Kain-Fritsch (new Eta) cumulus scheme. Meteorological fields produced by WRF were nested to 1 km resolution with 112 by 112 grid cell domain to better capture plume physics in a plume transport model. The vertical layers were in 34 sigma levels that increase in thickness by height with lowest layer being around 20 m thick. WRF winds were more easterly than the measurements in the upper atmosphere. The difference between modeled and observed wind directions increased at higher altitudes. To mimic the correction in wind direction domain wide, the aircraft path was shifted counterclockwise by 30 degrees at the fire center. All three simulated plumes aligned well with the aircraft path after the adjustment.

The Community Multiscale Air Quality (CMAQ) modeling system [Byun and Schere, 2006] simulates transport, diffusion, and reaction of emissions from various sectors. CMAQ used the same grid domain in WRF. The background emissions were estimated by the Sparse Matrix Operator Kernel Emissions Modeling System (SMOKE) [*Coats*, 1996] using National Emission Inventories 2005 (NEI05, http://www.epa.gov/ttn/chief/net/2005inventory.html#inventorydata) with SAPRC-99 atmospheric chemical mechanism.

Although CMAQ has multiscale capabilities that can reduce the effect of numerical dilution due to gridded cells, the model does not contain fire plume specific physics. Therefore, the dispersion of the plume was done only in Daysmoke. In order for

Daysmoke to be simulated in sync with CMAQ, Daysmoke was integrated into CMAQ as a subroutine. The volume of CMAQ's grid cells was used to convert the $PM_{2.5}$ particle mass to a gridded concentration. This additional $PM_{2.5}$ concentration from the fire was included without going through CMAQ's advection, diffusion, reaction, and deposition processes.

The concentrations obtained from CMAQ were extracted every 15 minutes. Model outputs were interpolated temporally at the location of the aircraft. On average the aircraft took 20 seconds to travel 1 km, the length of a grid cell in CMAQ. 20-second running averages of the aircraft data were used to evaluate modeled plume concentrations. The height of the plume center was calculated by taking the average of particle heights in a section of a Daysmoke plume. Measured plume height was defined as the average height of aircraft locations when the concentration was larger than 50 μg m^{-3}.

3.4 Results and Discussion

3.4.1 Emission and Fuel Consumption Rates

The emission rates and the fuel consumption rates were compared for the three approaches: the ground-based, the satellite-based, and the hybrid method (Figure 3.4). The ground-based approach using Photo Series, FEPS, and burn specific emission factor estimated that 27.37 metric tons of $PM_{2.5}$ were emitted from the burn. The satellite-based approach estimated the total $PM_{2.5}$ emitted to be 11.65 metric tons, 43% of the ground-base prediction. Due to the satellite-based approach having a larger $PM_{2.5}$ emission factor than that of ground-based, the total fuel consumed was severely lower compared to the ground-based case. The ground-based fuel consumption, which is the same for the

aggregated method's fuel consumption, was 3215.4 metric tons whereas the satellite-based fuel consumption was only 1093.2 metric tons.

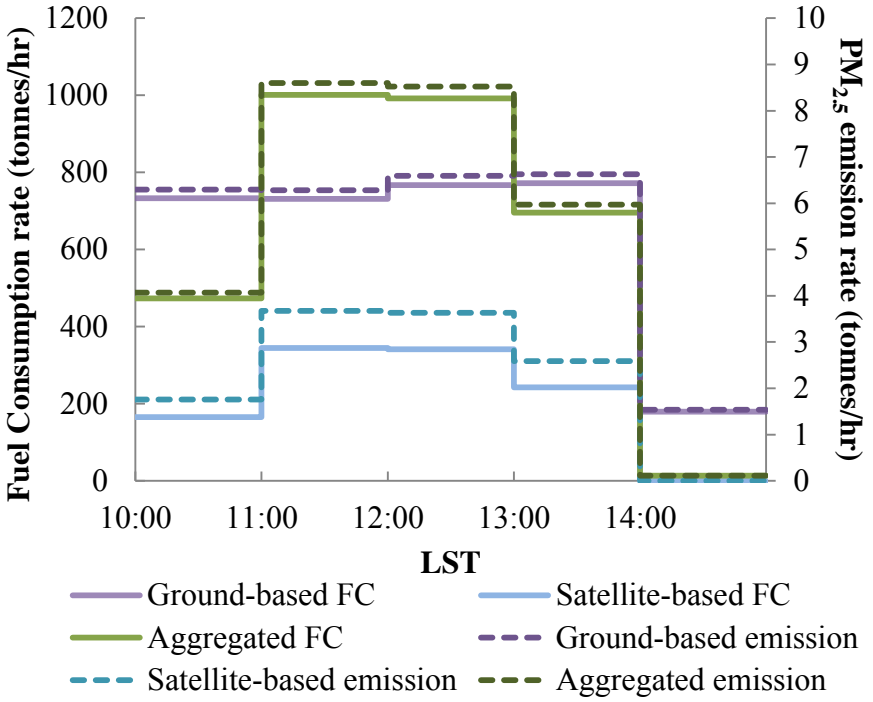

Figure 3.4: Hourly $PM_{2.5}$ emission rate (right axis with dotted lines) and hourly fuel consumption (FC) rate (left axis with solid lines) for the Williams fire case; obtained by ground-based (purple), satellite-based (blue), and hybrid (labeled as aggregated) or ground-based total emissions redistributed by Satellite's fractional emission rate (green).

Both emission rates and fuel consumption rates had a similar profile for each emission calculation method due to the linear relationship between the two (see Equation (1). Because the area of the burn was assumed to grow linearly for the ground-based approach, the hourly emission rates remained steady for the duration of the burn, tapering off during the smoldering stage. The satellite-based approach captured an increase in fire intensity towards the middle of the burn but did not detect any smoldering emissions after the fourth hour. The hybrid emission rates had a similar profile to that of satellite-based

but at a larger magnitude. The hybrid approach had the highest maximum emissions and fuel consumption rates.

3.4.2 Plume Rise

The three sets of emission/fuel consumption rates showed different plume behaviors (Figure 3.5). The ground-based approach had the largest emission rate and fuel consumption rate for the first hour, which resulted in the ground-based approach having the highest end of the plume. By three hours into the burn, the plume calculated using the ground-based method was 233 m lower (Table 3.1) than the observed plume height, which is based on the aircraft altitude when measured concentrations were above the back ground concentration. The aircraft was maneuvered to follow the center of the plume. The plume using satellite-based emissions was even lower, by 335 m, and did not reach the height of the aircraft path. The hybrid plume center was only 65 m lower than the observed.

Table 3.1: Daysmoke-predicted plume height near 15 km downwind, bias and mean fractional error against the average aircraft altitude when measured concentrations were above the background concentration between 1230 and 1300 LST.

	Average plume-center height (m)	Bias ($\mu g/m^3$)	Mean Fractional Error* (%)
Ground-based emissions	643	-86.3	188
Satellite-based emissions	541	-101.2	196
Assimilated emissions	811	-13.6	163
Aircraft altitude	876		

$$*MFE = \frac{1}{n}\sum_{i=1}^{n}\frac{|P_i - O_i|}{\left(\frac{P_i + O_i}{2}\right)}$$

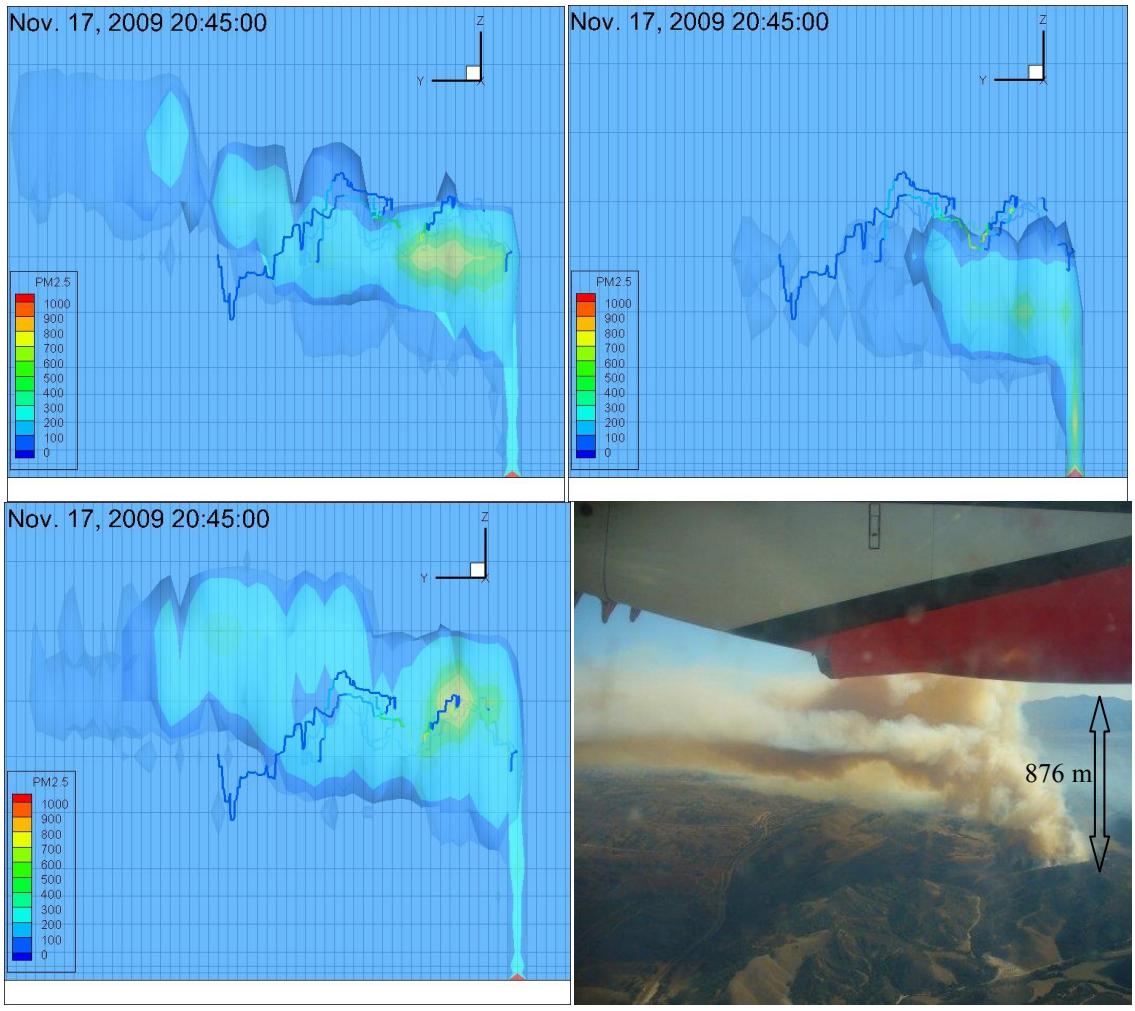

Figure 3.5: Snap shots of simulated plume in CMAQ using ground based emissions (top left), satellite based emissions (top right), and hybrid of ground and satellite data (bottom left) three hour into the burn. Isosurface of the plume drawn at where $PM_{2.5}$ concentration is 50 μg m^{-3}. Aircraft path shown in a line and color-coded according to the measured concentration. Another photograph of the smoke plume from the Williams Fire taken from the USFS Twin Otter.

3.4.3 Downwind Concentration

Concentration analysis was done when the aircraft traversed through the plume. From 1230-1300 LST, the aircraft flew in and out of the plume traveling away from the fire (Figure 3.6). The simulated plumes were narrower, therefore the modeled concentrations spiked more rapidly when compared to the observations. The

concentration peaks from the satellite-based plume were too low because the center of the plume was too low to be captured by the aircraft. The aircraft descended closer to the ground for the fourth peak. This allowed the aircraft to reach the center of the plume using ground-based method; therefore the simulated concentration was even larger than the observation. The fifth peak was missed by all three simulations simulated plumes were less wide than observed. The concentrations from hybrid plume closely followed the measured concentrations.

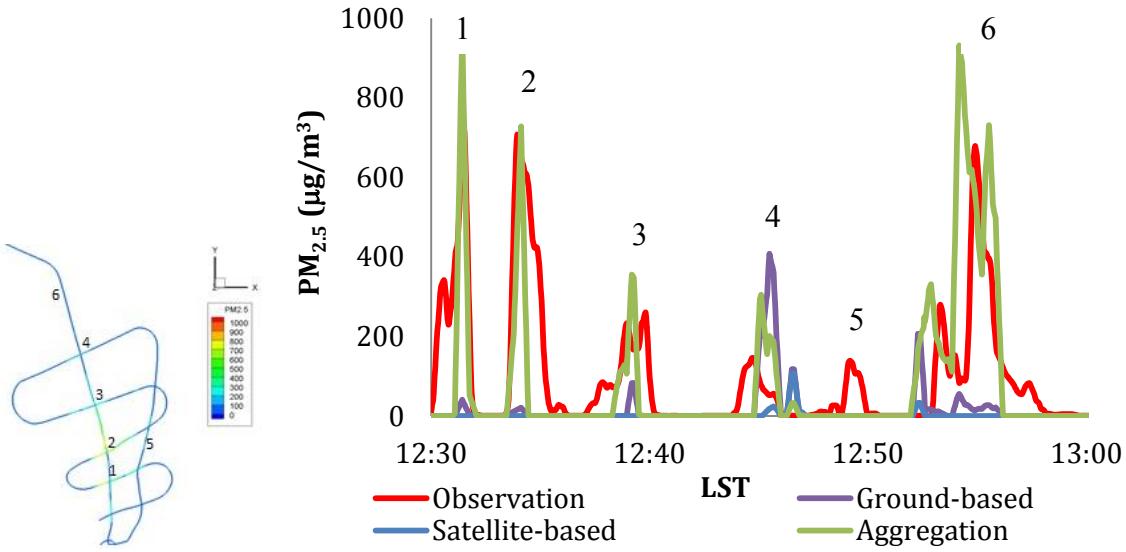

Figure 3.6: 20-second running average of $PM_{2.5}$ concentration along the aircraft path focusing between 1230 LST to 1300 LST: simulations with emissions from ground-based (purple), satellite-based (blue), and hybrid (labeled as Aggregation in green) and measured (red).

For the 30-minute segment of the flight simulated, all three simulations had negative biases (Table 3.1). The satellite-based approach has the largest bias and error, followed by the ground-based approach. The difference between the satellite-based approach and the hybrid approach was the total amount of $PM_{2.5}$ emitted, and that improvement reduced the bias by 87.6 µg m^{-3} and the mean fractional error by 33%.

When the same total emissions were redistributed using satellite-retrieved fractional emission rate for the hybrid method, the bias in the hybrid method was reduced by 72.7 $\mu g\ m^{-3}$ and the mean fractional error by 25 %.

3.5 Conclusion

Comparisons of $PM_{2.5}$ emission rates and downwind concentrations derived from the ground-based and satellite-based data showed that the satellite-based approach underpredicted emissions for the studied prescribed burning case. Total $PM_{2.5}$ emissions from the satellite-based approach were only 43% of the ground-based emission. Satellite-based fuel consumption was only one-third of the fuel consumption predicted by the ground-based approach. Relationships of fuel consumption/emission rates to plume rise and downwind concentrations were studied. Hybrid of ground-based emissions with satellite-derived fractional emission rates predicted the downwind concentrations closer to the aircraft measurements than the other two emission sets. The improvement in total emissions decreased the downwind concentration error by 33 %. The improvement in fractional emission rates decreased the error by 25%. This study showed the strength in combining ground based emissions and satellite based fire growth can improve plume dispersion modeling for smaller biomass burnings.

3.6 References

Achtemeier, G. L., S. A. Goodrick, Y. Liu, F. Garcia-Menendez, Y. Hu, and M. T. Odman (2011), Modeling smoke plume-rise and dispersion from southern United States prescribed burns with Daysmoke, *Atmosphere*, *2*(3), 358-388, doi:10.3390/atmos2030358.

Akagi, S., J. Craven, J. Taylor, G. McMeeking, R. Yokelson, I. Burling, S. Urbanski, C. Wold, J. Seinfeld, and H. Coe (2012), Evolution of trace gases and particles emitted by a chaparral fire in California, *Atmospheric Chemistry and Physics*, *12*(3), 1397-1421.

Anderson, G., D. Sandberg, and R. Norheim (2004), Fire Emission Production Simulator (FEPS) User's Guide (version 1.0), *Prepared by the USDA Forest Service, Pacific Northwest Research Station, Seattle, WA*.

Andrews, P. L., C. D. Bevins, and R. C. Seli (2003), *BehavePlus Fire Modeling System: Version 2.0: User's Guide*, US Department of Agriculture, Forest Service, Rocky Mountain Research Station.

Burling, I., R. J. Yokelson, S. Akagi, S. Urbanski, C. E. Wold, D. W. Griffith, T. J. Johnson, J. Reardon, and D. Weise (2011), Airborne and ground-based measurements of the trace gases and particles emitted by prescribed fires in the United States, *Atmospheric Chemistry and Physics*, *11*(23), 12197-12216.

Byun, D., and K. L. Schere (2006), Review of the governing equations, computational algorithms, and other components of the models-3 Community Multiscale Air Quality (CMAQ) modeling system, *Appl. Mech. Rev.*, *59*(2), 51-77, doi:10.1115/1.2128636.

Coats, C. J. (1996), High-performance algorithms in the Sparse Matrix Operator Kernel Emissions (SMOKE) modeling system, paper presented at Proc. Ninth AMS Joint Conference on Applications of Air Pollution Meteorology with A&WMA, Amer. Meteor. Soc., Atlanta, GA.

Crutzen, P. J., and M. O. Andreae (1990), Biomass burning in the tropics: Impact on atmospheric chemistry and biogeochemical cycles, *Science*, *250*(4988), 1669-1678.

Hu, Y., M. T. Odman, M. E. Chang, W. Jackson, S. Lee, E. S. Edgerton, K. Baumann, and A. G. Russell (2008), Simulation of air quality impacts from prescribed fires on an urban area, *Environmental Science & Technology*, *42*(10), 3676-3682.

Ichoku, C., and L. Ellison (2013), Global top-down smoke aerosol emissions estimation using satellite fire radiative power measurements, *Atmospheric Chemistry and Physics Discussions*, *13*(10), 27327-27386.

Kaiser, J., A. Heil, M. Andreae, A. Benedetti, N. Chubarova, L. Jones, J.-J. Morcrette, M. Razinger, M. Schultz, and M. Suttie (2012), Biomass burning emissions estimated with a global fire assimilation system based on observed fire radiative power, *Biogeosciences*, *9*(1), 527-554.

Liousse, C., B. Guillaume, J. Grégoire, M. Mallet, C. Galy, V. Pont, A. Akpo, M. Bedou, P. Castéra, and L. Dungall (2010), Updated African biomass burning emission inventories in the framework of the AMMA-IDAF program, with an evaluation of combustion aerosols, *Atmospheric Chemistry and Physics*, *10*(19), 9631-9646.

Ottmar, R., R. Vihnanek, and J. Regelbrugge (2000), Stereo photo series for quantifying natural fuels, Vol. IV: pinyon-juniper, chaparral, and sagebrush types in the southwestern United States, *National Wildfire Coordinating Group, National Interagency Fire Center# PMS*, *833*.

Petrenko, M., R. Kahn, M. Chin, A. Soja, T. Kucsera, and Harshvardhan (2012), The use of satellite-measured aerosol optical depth to constrain biomass burning emissions source strength in the global model GOCART, *Journal of Geophysical Research-Atmospheres*, *117*, doi:D18212
10.1029/2012jd017870.

Prichard, S., R. Ottmar, and G. Anderson (2007), Consume 3.0 user's guide and scientific documentation, edited by U. F. Service, Pacific Wildland Fire Sciences Laboratory, Seattle.

Prichard, S., D. Sandberg, R. Ottmar, E. Eberhardt, A. Andreu, P. Eagle, and K. Swedin (2013), Fuel Characteristic Classification System version 3.0: technical documentation.

Reid, J. S., E. J. Hyer, E. M. Prins, D. L. Westphal, J. Zhang, J. Wang, S. A. Christopher, C. A. Curtis, C. C. Schmidt, and D. P. Eleuterio (2009), Global monitoring and forecasting of biomass-burning smoke: Description of and lessons from the Fire Locating and Modeling of Burning Emissions (FLAMBE) program, *Selected Topics in Applied Earth Observations and Remote Sensing, IEEE Journal of*, *2*(3), 144-162.

Reinhardt, E. D., R. E. Keane, and J. K. Brown (1997), First order fire effects model: FOFEM 4.0, user's guide.

Seiler, W., and P. Crutzen (1980), Estimates of gross and net fluxes of carbon between the biosphere and the atmosphere from biomass burning, *Climatic Change*, *2*(3), 207-247, doi:10.1007/BF00137988.

Skamarock, W. C., J. B. Klemp, J. Dudhia, D. O. Gill, D. M. Barker, M. G. Duda, X.-Y. Huang, W. Wang, and J. G. Powers (2008), A description of the Advanced Research WRF version 3, Tech. Note, NCAR/TN-475+STR*Rep*., Natl. Cent. for Atmos. Res., Boulder, Colorado, USA.

Sofiev, M., R. Vankevich, M. Lotjonen, M. Prank, V. Petukhov, T. Ermakova, J. Koskinen, and J. Kukkonen (2009), An operational system for the assimilation of the satellite information on wild-land fires for the needs of air quality modelling and forecasting, *Atmos Chem Phys*, *9*(18), 6833-6847.

Stocks, B. J., M. Fosberg, T. Lynham, L. Mearns, B. Wotton, Q. Yang, J. Jin, K. Lawrence, G. Hartley, and J. Mason (1998), Climate change and forest fire potential in Russian and Canadian boreal forests, *Climatic Change*, *38*(1), 1-13.

US-EPA (2013), The 2011 National Emissions Inventory, edited, US-EPA.

van der Werf, G. R., J. T. Randerson, L. Giglio, G. Collatz, M. Mu, P. S. Kasibhatla, D. C. Morton, R. DeFries, Y. v. Jin, and T. T. van Leeuwen (2010), Global fire emissions and the contribution of deforestation, savanna, forest, agricultural, and peat fires (1997–2009), *Atmospheric Chemistry and Physics*, *10*(23), 11707-11735.

Westerling, A. L., H. G. Hidalgo, D. R. Cayan, and T. W. Swetnam (2006), Warming and earlier spring increase western US forest wildfire activity, *science*, *313*(5789), 940-943.

Wiedinmyer, C., S. Akagi, R. Yokelson, L. Emmons, J. Al-Saadi, J. Orlando, and A. Soja (2011), The Fire INventory from NCAR (FINN): A high resolution global model to estimate the emissions from open burning, *Geoscientific Model Development*, *4*(3), 625-641.

Zhang, X., S. Kondragunta, J. Ram, C. Schmidt, and H.-C. Huang (2012), Near-real-time global biomass burning emissions product from geostationary satellite constellation, *Journal of Geophysical Research: Atmospheres (1984–2012)*, *117*(D14).

Zhang, X., S. Kondragunta, C. Schmidt, and F. Kogan (2008), Near real time monitoring of biomass burning particulate emissions (PM2. 5) across contiguous United States using multiple satellite instruments, *Atmospheric Environment*, *42*(29), 6959-6972.

CHAPTER 4

Coupling of Smoke Dispersion Model with Air Quality Model: Combining Lagrangian Model with Eulerian Model

Abstract

Fire plumes chemically and physically evolve over time as they are transported, sometimes traveling for thousands of kilometers across continents. Chemical transport models have been developed to simulate atmospheric transport and chemical reactions from the local to the global scale, yet they cannot accurately simulate fire plumes because of numerical diffusion and/or lack of fire-specific physics. Fire plume transport models, such as Lagrangian particle models, can predict plume dispersion in detail but only at a local scale.

A new approach for estimating the smoke plume concentration in a chemical transport model using a Lagrangian stochastic particle model is described in this study. Details of a smoke plume are preserved by implementing the sub-grid plume model (i.e. Daysmoke) and in a chemical transport model (i.e. CMAQ) until the plume travels to a certain distance away from the source. Compared to injecting plume emissions at the source, including Daysmoke in CMAQ significantly increased the model's performance. Two attempts were made to minimize the effect of numerical diffusion in CMAQ: by controlling grid size and vertical diffusivity coefficient. Results showed that CMAQ's vertical diffusivity coefficient is insignificant in plume dispersion,

and increasing grid resolution helps maintain the plume's strong concentration gradient farther downwind.

4.1 Introduction

Many modeling tools for the prediction of fire emissions, fire behavior, and plume transport from agricultural and forest burns have been developed over the last few decades. Smoke dispersion models usually require emissions and heat release to simulate plume behavior and plume height. The models are theoretical or empirical, and come in Gaussian Plume, Lagrangian (puff and particle) and Eulerian grid models [*Goodrick et al.*, 2013]. The models have governing equations specific to fire plumes at the local scale, and some also include equations associated with chemical reactions occurring inside the smoke plumes such as CALPUFF. A few also account for two way interaction between fire and its surrounding atmospheric conditions such as WRF-FIRE. Typically, the more detailed and complex a smoke model is, the more it becomes computationally burdensome. A model like Daysmoke [*Achtemeier et al.*, 2011], a Lagrangian particle model, falls in the middle of the complexity spectrum since it is an empirical model (not a full physics model) that includes key fire physics equations.

Eulerian meteorological models and chemical transport models (CTMs) are also used to predict the effects of biomass burning smokes. The Weather Research and Forecasting model (WRF), which is a meteorological model, now includes a fire growth model inside and is called WRF-FIRE [*Coen et al.*, 2013]. The effect of fire on its environment can also be studied in WRF-FIRE since they are two-way coupled. In CMAQ, annual fire emissions are usually interpolated and emitted in the lowest layer [*Hu et al.*, 2008; *Tian et al.*, 2009]. *Tian et al.* [2009] found that details (spatially and

temporally) of fire emissions are important to CMAQ. *Liu et al.* [2008] found that CMAQ performance improved when a plume was injected at an appropriate height rather than on the ground layer. On the other hand, *Yang et al.* [2011] found that plume injection height was not as significant to CMAQ performance as long as they were within the mixing height because the fire emissions became well mixed throughout the mixing layer height. Coarse resolutions in CTMs introduce numerical diffusion to the plume's concentration gradient [*Karamchandani et al.*, 2011]. In addition, without including fire specific physics CTMs cannot preserve the smoke plume well, leading to a stronger vertical mixing.

Different approaches have been used to preserve smoke plume concentrations in CTMs. One approach is to increase the resolution of the grid cells [*Garcia-Menendez and Odman*, 2011]. Another approach is Plume-in-Grid (PinG), where a Lagrangian puff smoke model calculates the plume transport until the puff grows to be as large as the grid cell or the plume has chemically matured [Karamchandani et al., 2011]. PinG currently exists inside the Comprehensive Air-quality Model with extensions (CAMx, http://www.camx.com) and CMAQ. In this study, Daysmoke was coupled with CMAQ. Daysmoke can capture smoke development specific to prescribed burnings and includes buoyancy and entrainment of a plume. A plume is assumed to be inert in Daysmoke, and the model is designed to simulate plumes up to 16 km downwind. On the other hand, CMAQ simulates complex chemical reactions in domains ranging from the local to the continental scale. The coupling was performed to preserve the benefits of both models. Daysmoke, as a subroutine in CMAQ, carried the plume until it reached a certain distance away from the source, and then the plume from Daysmoke was inserted into the

appropriate vertical layers in CMAQ. Two approaches were tested to reduce the numerical diffusion in CMAQ: by reducing vertical diffusivity and grid resolution by applying adaptive grid [*Garcia-Menendez et al.*, 2010].

4.2 Methods

Daysmoke was included in CMAQ in a similar way as the developed system describe in Chapter 3. In other studies mentioned previously where CMAQ was used to simulate biomass burning plumes, the plume concentrations were typically injected either at the surface level or by vertically distributing fire emissions directly at the source. For this study, the smoke particles remained inside Daysmoke until it reached the wall, which is the interface between Daysmoke and CMAQ where the particles are handed over to CMAQ (Figure 4.1). The wall was set at various distances to study the effect of plume concentration dilution between Daysmoke and CMAQ. Daysmoke became a new subroutine in CMAQ before going through advection, diffusion, and reaction processes; therefore the plume does not go through CMAQ's processes until after the wall. The Daysmoke parcels were handed over in CMAQ at every output time interval in CMAQ, which was set at every 15 minutes for this study. The particles were converted into concentrations using the grid cells from CMAQ.

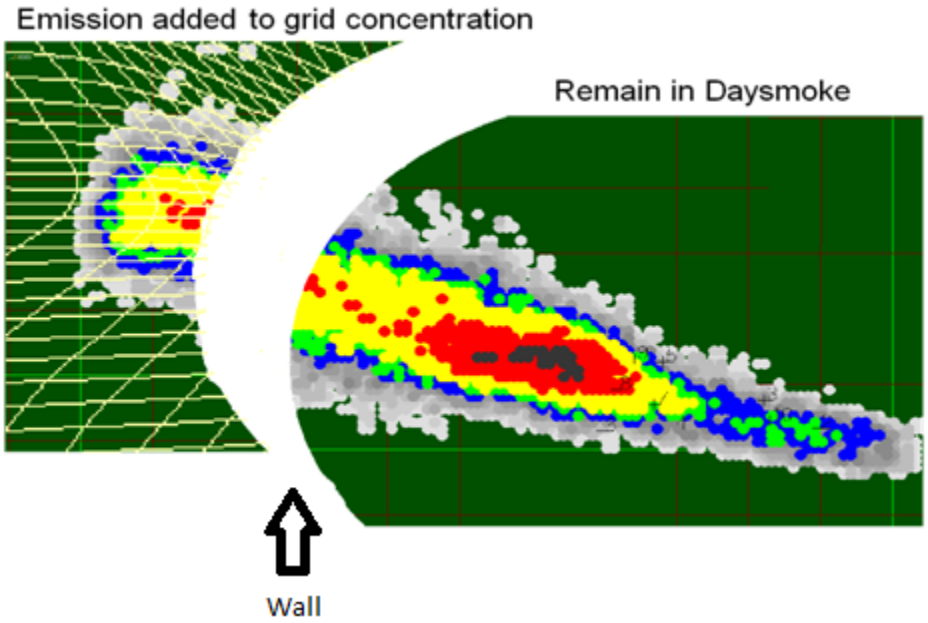

Figure 4.1: Transition between Daysmoke to CMAQ. For a plume traveling northwest, any particles farther than the wall are injected in 3-D concentration array inside CMAQ (left hand side). The remaining particles stay inside Daysmoke until they travel further than the wall (right hand side).

Since CMAQ is known to dilute plume concentrations, two approaches were made to minimize this dilution issue. One method was by decreasing the vertical diffusivity inside CMAQ. In the latest version of CMAQ, the minimum vertical diffusivity coefficient is only a tenth of the minimum vertical diffusivity coefficient that is in CMAQ version 4.5. Another reason why CMAQ dilutes the plume concentration to a greater extent than reality is because CMAQ does not account for buoyancy and entrainment where the plume does not actually mix as well with its surrounding in reality. To account for these differences, the vertical diffusivity coefficients (K_z) were reduced by 90% at every grid cell and the effect of that variable on simulated plume concentrations was studied.

Another method to reduce the numerical diffusion of plume concentrations in CMAQ was to use an adaptive grid in CMAQ. The idea of dynamic adaptive grids in atmospheric modeling was introduced by *Skamarock et al.* [1989] in a 3-D meteorological model. Adaptive grid CMAQ was introduced by *Srivastava et al.* [2000]. The adaptive grid algorithm was designed to increase grid resolution at the locations of interest by clustering grid nodes at these locations. In this study, the grids were adapted to $PM_{2.5}$ concentrations from the fire. In *Achtemeier et al.* [2011], grid adaptation was performed on surface level $PM_{2.5}$ concentrations and only the horizontal grid domain was dynamically changing. Since the majority of the plume concentration is above ground, the 2-D grid adaptation was performed on $PM_{2.5}$ concentrations in all vertical layers (i.e., vertical columns) in this study. The vertical layers remained in sigma coordinates, and vertical size gradually increased with height starting from the ground with 20 m thickness.

Grid adaptation was first performed on the entire plume. This led to very fine grid refinement near the fire and coarsening at the end of the plume, which caused the grids to be larger than its original uniform grid size. When the plume remains inside Daysmoke, the grid size in CMAQ does not affect the plume distribution. Therefore, grid adaptation was performed only for the portion of the plume outside of Daysmoke-CMAQ interface or the "wall".

4.3 Burn Description

The Williams Fire case on November 17, 2009 from Chapter 3 was used for this study. The second flight that flew back out at 2200 GMT (1400 LST) for two hours was used since it flew along the plume as far as 60 km away from the fire and long-range

plume transport is of interest in this study (Figure 4.2). Since the aggregated emissions produced the downwind concentrations closest to the observations in Chapter 3, the same parameters used for the aggregated case were utilized in this study. The same emission rates and fire diameters were used for all simulations in this chapter.

Figure 4.2: A picture of the end of Williams Fire plume taken from USFS Twin Otter.

The wind speed predicted by WRF and the wind speed measured by the aircraft were compared for the duration of Flight 2 (Figure 4.3). Since WRF overpredicted the wind speed, the modeled wind speed field was reduced by a constant percentage throughout the domain. A 28% reduction in wind speed had the least squared fit. Daysmoke used this reduced wind speed for plume dispersion modeling. To account for the difference between modeled and measured wind directions, the aircraft path was shifted using a method similar to the one described in Chapter 3 where the aircraft path was rotated at a constant degree until the simulated plume aligned with the aircraft path.

For the latter portion of the burn, the plume aligned with the aircraft path with a 20 degree counterclockwise rotation.

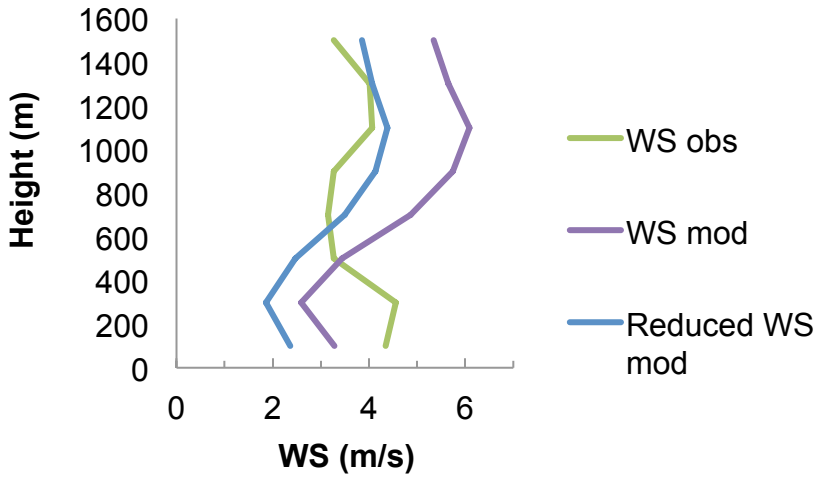

Figure 4.3: Wind speed comparison between averages of aircraft observation by altitude (green) and WRF prediction (purple). The reduced modeled wind speed (blue) was used in Daysmoke simulation.

The present study also focused on the 5 minutes between 2255 and 2300 GMT when the aircraft flew between 50 km to 60 km downwind from the fire. Using the observed wind speed, the smoke near the area 50 km downwind was expected to be 3.5 to 4 hours old. 20-second running average was applied to the aircraft data that was sampled every 2 seconds. The gridded concentrations from the model were interpolated over time and extracted at the location that the aircraft was at every 2 seconds. 20-second running average was also applied to these concentration extractions from the simulated concentrations, and time series comparisons were performed.

During the 5 minutes, the aircraft circled the same location twice at various altitudes, which provided the data for the concentration distribution across the plume. The concentrations were grouped in 50 m vertical increments between 700 m and 1300 m above the ground. Horizontally across the plume, the concentrations were averaged for every 400 m of the plume. The standard deviation of the concentration profile across the plume was calculated assuming that the extracted data would fit a Gaussian distribution curve.

4.4 Results

4.4.1 Wall Distance Analysis

Daysmoke-CMAQ simulations of Williams Fire successfully captured the plume traveling north initially then shifting clockwise throughout the burn period. Figure 4.4 shows three of the plumes simulated in uniform grids with the wall between Daysmoke and CMAQ set at various distances. All three plumes traveled in the same direction. The portion of the plume inside CMAQ was well mixed and made the isosurface smoother in Figure 4.4. Plume characteristics such as the width and the length of the plume vary in all three snapshots. The plume traveled farther when the wall was placed farther away from the fire.

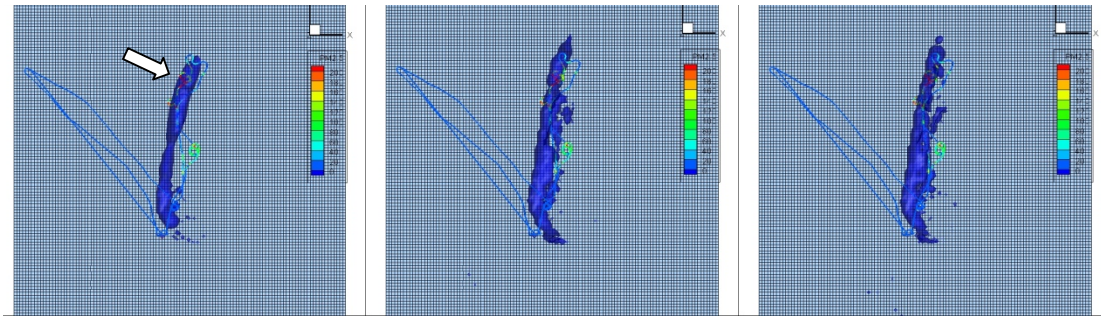

Figure 4.4: Bird's eye view of the simulated plumes at 5 hours after ignition with various wall distances: (from left to right) 16 km, 45 km, 60 km (case when CMAQ does not take over plume dispersion). Isosurface plot at 20 micrograms per cubic meters. The aircraft path shown in a line with colors representing measured $PM_{2.5}$ concentration. White arrow points to the studied loop.

A time series concentration comparison between the different simulations with various wall distances did show a large difference in the magnitude of concentration peaks (Figure 4.5). The aircraft flew in and out of the plume during the 5 minutes, allowing the analysis to be performed on four concentration peaks. As the wall was placed closer to the 5-minute loop, higher plume concentrations were predicted. Out of the uniform grid simulations, the case with the wall set at 45 km downwind captured the concentration peaks closest to the observations. The 45 km wall simulation had the lowest mean fractional error (MFE) between the measurement and the modeled $PM_{2.5}$ concentrations during the 5 minutes when the aircraft circled around 55 km downwind with a MFE of 39% (Figure 4.6). The wall placement at 2 km was assumed to represent the typical method of emitting smoke emissions at the fire location with Daysmoke predicted vertical profile. The MFE was reduced by 67% by moving the wall from 2 km to 45 km. Whether Daysmoke carried the plume up to 2 km, 16 km or 30 km away from the fire, the plume concentration in CMAQ was well mixed to its surrounding grid cells

so that the plume concentrations were too diluted by the time the plume traveled 50 km downwind. The MFEs remained greater than 120% for wall distances less than 40 km. A significant reduction in the MFE was observed when the wall was set at 40 km, which was also when the concentration peaks were larger and more apparent in Figure 4.5.

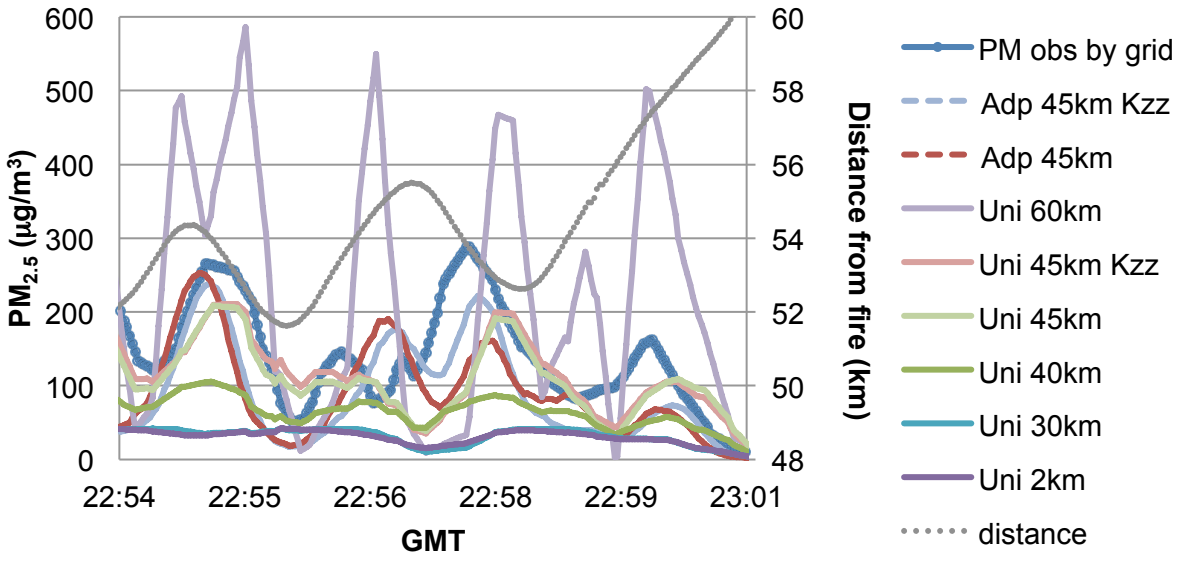

Figure 4.5: Time series $PM_{2.5}$ concentration comparison from 2255 to 2300 GMT between simulations using various wall distances (2 km to 60 km) using uniform grid (solid lines) and adaptive grid (dashed lines). Cases labeled K_{zz} were when the vertical diffusivity coefficient was reduced by 90%. The aircraft measurements are in dark blue (lines with circles). The axis on the right is for the aircraft distance away from the fire in km (dotted grey).

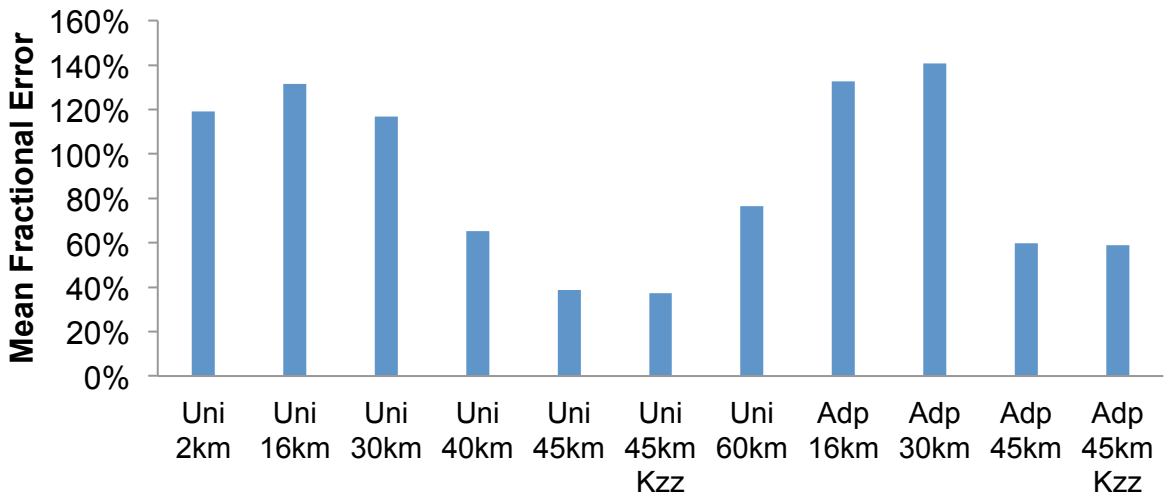

Figure 4.6: Mean fractional error of the simulated time series $PM_{2.5}$ concentration using various wall distance (2km to 60km) against the aircraft measurements between 2255 to 2300 GMT. 45km K_{zz} cases were when the vertical diffusivity coefficients were reduced by 90%.

Once the plume was handed over to CMAQ, the concentration gradient that existed inside the plume continued to decrease over time (Figure 4.7). Similar to the findings from [*Yang et al.*, 2011], the concentrations in CMAQ decreased at the rate of 2/3 over distance no matter where the wall was placed. The concentration gradient reached its plateau by 17 km away from the wall. One cause of the dilution effect may be due to the advection scheme used in CMAQ. CMAQ uses the Piecewise Parabolic Method (PPM) advection scheme which cannot hold the ideal concentration solution over the time it travels in the domain, which was proven in *Odman and Russell* [1998].

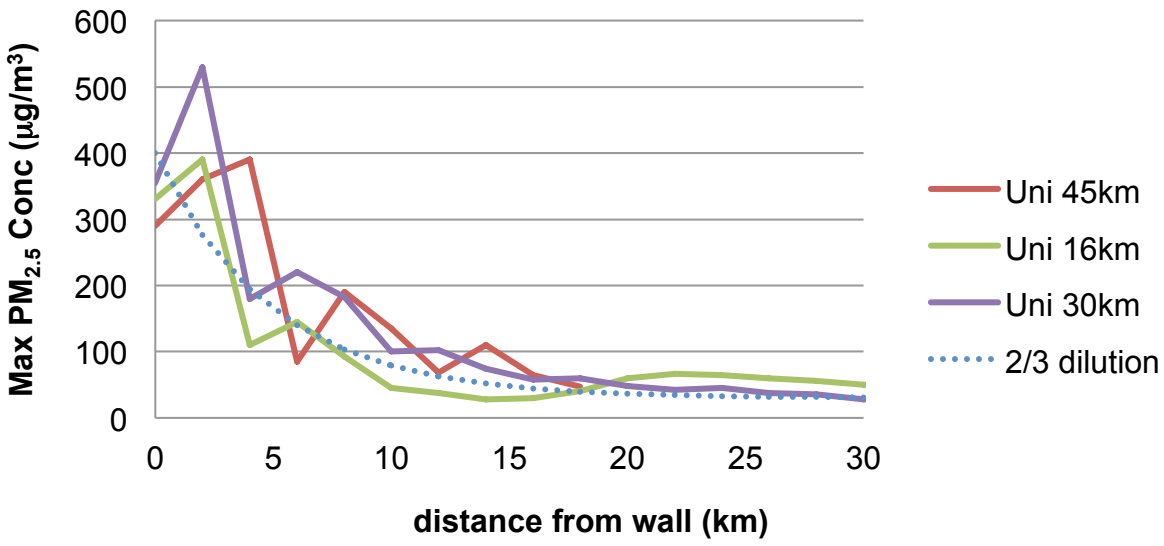

Figure 4.7: The maximum $PM_{2.5}$ concentration observed in CMAQ at a certain distance beyond the wall (16 km, 30 km, and 45 km). The dotted blue line is an example where 400 µg/m^3 decreases at the rate of 2/3 over distance.

4.4.2 Grid Resolution

Applying grid adaptation to the fire plume allowed the grid cells to be as small as hundreds of meters. Figure 4.8 shows the cross sectional $PM_{2.5}$ concentrations of the plume at 55km downwind. With the uniform grid, the concentration decreased after the plume reached the wall. However in the adaptive grid, the concentration remained above 100 µg m^{-3} 15 kilometers beyond the wall. Even for cases with walls set at 30 km and 45 km, the simulations with the adaptive grid preserved the concentration gradient farther than in the uniform grid cases. Maximum concentrations obtained along the aircraft path were higher in adaptive grid simulations (Figure 4.5, Table 4.1).

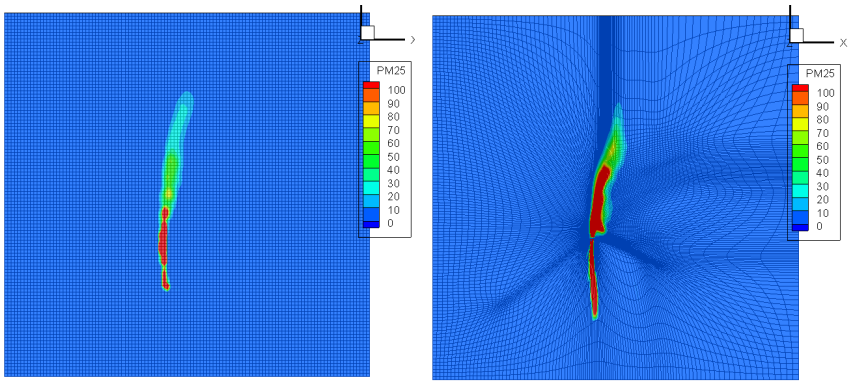

Figure 4.8: Uniform grid (left) vs. adaptive grid (right) $PM_{2.5}$ concentration at 1000 m above ground at 2115 GMT, both walls at 16km.

Both uniform and adaptive grid simulations with walls set at 16 km had similar MFEs (Figure 4.6). The MFEs for adaptive grid cases with 30 km and 45 km walls were greater than the same simulations using a uniform grid because Daysmoke was designed to simulate plume dispersion for 16 km and carried the large concentration gradient that exist at 16km downwind farther than 30 km downwind. Therefore, dividing the pollutant mass by a larger volume in uniform grid counteracted the overestimated concentration gradient inside the plume. For the case where only Daysmoke was used for plume transport (the case with a 60 km wall), the width of the normal distribution curve for the Daysmoke only plume was narrower than the curve based on measurements (Figure 4.9) because the plume did not go through diffusion processes inside CMAQ. The standard deviation of the normal distribution curve in Table 4.1 is another indication of the width of the plume. The Daysmoke-only plume had a standard deviation of 696 m, which is much smaller compared to the standard deviation of what was observed, which was 1118 m. Plume dispersion in Daysmoke was not sufficient that the maximum concentration was much higher than the maximum concentration measured by the aircraft. The standard

deviation of the width of the plume for the uniform grid with a 45 km wall was the closest to the standard deviation of the measurements (Table 4.1), therefore the plume width was simulated the best and the concentration peaks were in sync over time in Figure 4.5.

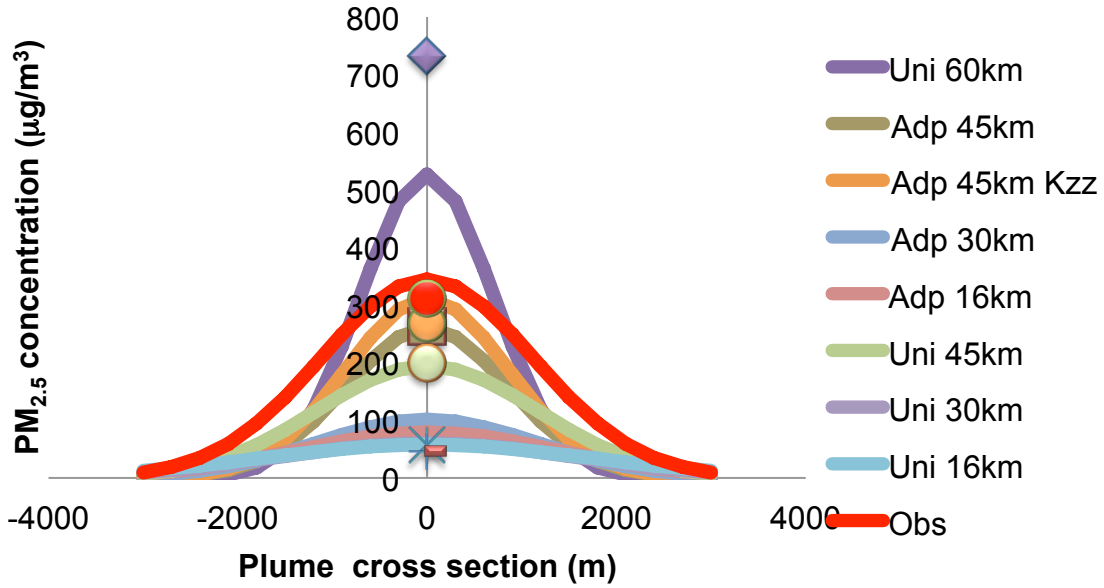

Figure 4.9: $PM_{2.5}$ concentration distribution across the plume near 55 km downwind for various wall distances. Plume's cross-section was converted to fit the Gaussian distribution deriving from the area under the curve that connects 16 measured or simulated concentrations. Maximum measured/predicted concentrations are shown in markers.

Table 4.1: Average and maximum concentration at 55 km downwind and standard deviation of the simulated and observed concentration profile across the plume.

	Uni 16km	Uni 30km	Uni 45km	Uni 60km	Adp 16km	Adp 30km	Adp 45km	Adp 45km Kzz	Obs
C_{avg} (µg/m^3)	36.8	35.7	88.6	145.9	34.6	46.5	88.9	105.9	152.5
C_{max} (µg/m^3)	47.2	45.9	199.3	732.7	57.4	58.2	261.9	267.9	310.9
St. dev. (m)	1708	1551	1152	696	1370	1164	861	855	1118

Despite the disagreement with observations, the result from the case with only Daysmoke transporting the plume is the ideal solution to the portion of the plume beyond the wall for all Daysmoke-CMAQ simulations. Therefore, the case with less numerical diffusion should have similar plume characteristics to the simulation with a 60 km wall. The time series concentration MFE was larger for the adaptive grid case with a 45 km wall than the same case using a uniform grid, however the plume width (standard deviation of 861 m) and the concentration peak (261.9 $\mu g\ m^{-3}$) for the adaptive grid case were the closest to the Daysmoke only plume (with standard deviation of 696 m and maximum concentration of 732.7 $\mu g\ m^{-3}$) (Figure 4.9, Table 4.1). Therefore, increasing the grid resolution along the centerline of the plume showed a reduction in numerical diffusion and preserved the plume closer to the output straight from the sub-grid plume model at the wall.

4.4.3 Vertical Diffusivity

Vertical diffusivity coefficient was studied to understand its effect on well-mixed vertical diffusion in the PBL in CMAQ. The grid-specific vertical diffusivity coefficients throughout the domain were modified in the code to be multiplied by 0.1. The adaptive grid case with 45 km wall and vertical diffusivity coefficient reduced by 90% had the largest maximum concentration and the closest standard deviation to those from the Daysmoke-only plume (Table 4.1). However, the maximum concentration increased only by 6 $\mu g\ m^{-3}$ and the standard deviations differed only by 0.6% between with and without a reduced vertical diffusivity coefficient. 90% reduction in vertical diffusivity coefficients reduced the MFE by 1% for simulations with the adaptive grid and by 2% for

uniform grids (Figure 4.6). The vertical diffusivity coefficient had very little effect on vertical and horizontal plume dispersion in CMAQ.

4.5 Conclusion

Coupling a sub-grid plume model inside CMAQ improved CMAQ's ability to simulate a fire plume. In this study, including Daysmoke inside CMAQ reduced the mean fractional error by 67%. The magnitude of a concentration in CMAQ typically decreases at a rate of 1/3 going from one grid cell to next, and the plume's concentration gradient is lost by 20 km downwind. Therefore Daysmoke-CMAQ's performance improved when the wall was placed within 20 km from the point of interest. An adaptive grid was able to reduce the effect of numerical diffusion in CMAQ and carry the large concentration gradient in the plume farther than a uniform grid could. Reduction in the vertical diffusivity coefficient did not have a significant improvement to preserving the plume's concentration gradient. This result also implies that the concentration gradient issue is in the advection scheme.

There are three major issues in simulating fire plumes in a chemical transport model: numerical diffusion, and the absence of plume physics and plume chemistry. The modeling system introduced here addressed the first two issues. Inclusion of plume chemistry in the system is in plan for future studies. *Alvarado and Prinn* [2009] have included fire specific ozone reactions into another Lagrangian particle model. Similarly, including fire specific reactions of ozone and other reactive species such as organic carbon could further improve fire plume modeling in an Eulerian chemical transport model as well.

4.6 References

Achtemeier, G. L., S. A. Goodrick, Y. Liu, F. Garcia-Menendez, Y. Hu, and M. T. Odman (2011), Modeling smoke plume-rise and dispersion from southern United States prescribed burns with Daysmoke, *Atmosphere*, *2*(3), 358-388.

Alvarado, M. J., and R. G. Prinn (2009), Formation of ozone and growth of aerosols in young smoke plumes from biomass burning: 1. Lagrangian parcel studies, *Journal of Geophysical Research: Atmospheres (1984–2012)*, *114*(D9).

Coen, J. L., M. Cameron, J. Michalakes, E. G. Patton, P. J. Riggan, and K. M. Yedinak (2013), WRF-Fire: Coupled weather–wildland fire modeling with the Weather Research and Forecasting model, *Journal of Applied Meteorology and Climatology*, *52*(1), 16-38.

Garcia-Menendez, F., and M. T. Odman (2011), Adaptive grid use in air quality modeling, *Atmosphere*, *2*(3), 484-509.

Garcia-Menendez, F., A. Yano, Y. Hu, and M. T. Odman (2010), An adaptive grid version of CMAQ for improving the resolution of plumes, *Atmospheric Pollution Research*, *1*(4), 239-249.

Goodrick, S. L., G. L. Achtemeier, N. K. Larkin, Y. Liu, and T. M. Strand (2013), Modelling smoke transport from wildland fires: a review, *International Journal of Wildland Fire*, *22*(1), 83-94.

Hu, Y., M. T. Odman, M. E. Chang, W. Jackson, S. Lee, E. S. Edgerton, K. Baumann, and A. G. Russell (2008), Simulation of air quality impacts from prescribed fires on an urban area, *Environmental Science & Technology*, *42*(10), 3676-3682.

Karamchandani, P., K. Vijayaraghavan, and G. Yarwood (2011), Sub-grid scale plume modeling, *Atmosphere*, *2*(3), 389-406.

Liu, Y., G. Achtemeier, and S. Goodrick (2008), Sensitivity of air quality simulation to smoke plume rise, *J. Appl. Remote Sens.*, *2*, 021503, doi:10.1117/1.2938723.

Odman, M. T., and A. G. Russell (1998), Computational Fluid Dynamic Techniques in Air Quality Modeling, in *Applied computational fluid dynamics*, edited by V. K. Garg, pp. 335-397, CRC Press, New York, NY.

Skamarock, W., J. Oliger, and R. L. Street (1989), Adaptive grid refinement for numerical weather prediction, *Journal of Computational Physics*, *80*(1), 27-60.

Srivastava, R. K., D. McRae, and M. Odman (2000), An adaptive grid algorithm for air-quality modeling, *Journal of Computational Physics*, *165*(2), 437-472.

Tian, D., Y. T. Hu, Y. H. Wang, J. W. Boylan, M. Zheng, and A. G. Russell (2009), Assessment of biomass burning emissions and their impacts on urban and regional PM2.5: A Georgia

case study, *Environmental Science & Technology*, *43*(2), 299-305, doi:10.1021/es801827s.

Yang, E. S., S. A. Christopher, S. Kondragunta, and X. Y. Zhang (2011), Use of hourly Geostationary Operational Environmental Satellite (GOES) fire emissions in a Community Multiscale Air Quality (CMAQ) model for improving surface particulate matter predictions, *J. Geophys. Res.-Atmos.*, *116*, D04303, doi:10.1029/2010jd014482.

CHAPTER 5

An Assessment of Air Quality Deterioration from Prescribed Burning Scenarios in a Southern Pine Forest

Abstract

Fire behavior and downwind smoke concentration from a fire plume varies depending on key parameters such as weather conditions and emission rates, and heat released from the burn. Fire forecasting models that are currently used by land managers often show areas in fire danger depending on fire danger index or ground level $PM_{2.5}$ concentration increase from a fire. Fire forecasting systems are often simplified to be easier for the users, but more important temporal and spatial details of a plume can be obtained with a more complex system with a higher resolution. In this study, the fire modeling system from previous chapters, using a Lagrangian particle model inside an air quality model, was used as a prototype for a detailed smoke prediction tool.

Fire parameters that the experts are interested in are return interval, size, ignition type, time of day, and season of the burn. These scenarios were simulated for a burn case in Fort Benning, Georgia when the plume from a prescribed burning actually reached a nearby city. The results show that ambient relative humidity affects the amount of emissions, and the height of planetary boundary layer can affect the magnitude of the concentration downwind. An increase in burn area resulted in changes in plume structure with slightly higher centerline of the plume. The plume structural change was not

significant enough to place the majority of the plume above mixing layer, instead, significantly increased ground level $PM_{2.5}$ concentrations downwind. The most efficient burn, which was the aerial ignition burn, emitted less and had the lowest impact on downwind concentration on the ground because the plume reached above mixing layer. The plume height changed in respect to the diurnal changes in mixing layer height. Aerial burns or smaller burns while the planetary boundary layer is closer to the ground and releasing enough heat flux to take the plume higher than the planetary boundary layer resulted in lower pollutant concentration on the ground level.

5.1 Introduction

Prescribed burnings can reduce wildfire risks, and they are beneficial especially for pine forests [*Hurteau and North*, 2008]. Though the effects may not be as extreme as from wildfires, prescribed burnings still produce smoke that may deteriorate air quality in local areas. Land managers have the duty to practice prescribed burning effectively and protect safety of citizens nearby. Therefore, prescribed burnings must be performed on days with appropriate weather conditions when the smoke plume does not hit nearby urban areas. Emissions from the fire must be controlled to not exceed US NAAQS (http://www.epa.gov/air/criteria.html) for $PM_{2.5}$, which is 35 $\mu g\ m^{-3}$ for the 24-hour average primary and secondary $PM_{2.5}$ concentrations. A reliable fire forecasting system can help with planning to meet these requirements.

Smoke forecasting system requires the three components of fire behavior triangle; fuel, weather, and topography, and weather is the most significant parameter of the three [*Carlson and Burgan*, 2003]. Wind conditions affect the speed and direction of plume transport. Fuel component is also important since the amount of fuel consumed by a fire

determines the amount of heat release and fire emissions. Topography affects fire spread rate and direction as well, but topography is not addressed in this chapter. Depending on fire intensity, the plume can be trapped within mixing height or penetrate through the planetary boundary layer (PBL) and stay aloft. Smoke forecasting is complex, requiring many parameters that depend on one another.

Both fire weather and fire behavior forecasts are required for smoke predictions. In the US, the National Weather Service creates maps with fire weather watch zones. Fire potential is commonly calculated using Fire Danger Rating or Haines Index; both are based on moisture and weather conditions. FLAMBE [*Reid et al.*, 2009] is a smoke forecasting model which predictions are based on satellite retrievals. The Bluesky framework, a system that connects independent models of fire information, fuel loading, fuel consumption, fire emissions, and smoke dispersion, was initially developed for western US [*Larkin et al.*, 2009] and is now applied in air quality predictions with the Community Multiscale Air Quality (CMAQ) model [*Sullivan et al.*, 2008]. The results from fire forecasting models that are currently used by fire managers are simplified and only show areas that are in danger depending on the fire danger index or ground level $PM_{2.5}$ concentration increase due to a fire. The objective of this study was to provide better temporal and spatial predictions of $PM_{2.5}$ from a burn using the tools and methods mentioned in previous chapters.

Fire managers were asked to list factors that they would live to see varied in fire simulations. The top five factors are age of fuelbed, size, type of ignition, time of the day, and season of a burn. These fire scenarios were simulated using the prototype for a detailed fire-forecasting system from Chapter 4, which is a stochastic plume dispersion

model (Daysmoke) coupled with a chemical transport model (CMAQ). The impacts that the different fire variables have on downwind $PM_{2.5}$ concentration were studied.

5.2 Site Description

Different scenarios were performed based on a burn event that was conducted at Compartment F5 (32.3515 ^{o}N, 84.679 ^{o}W) inside Fort Benning, Georgia, USA on 9 April 2008 (Figure 5.1). Fort Benning is located in a long leaf pine forest that has been maintained by personal at the military base for many years. Compartment F5 was 121 ha (300 acre) and the fuel on the ground in F5 was three years old. Most of the fuel that burned was long leaf pine litter and duff. Winds blew from the east and southeast during the period of the burn. Ignition by hand started at 1230 EDT and was completed by 1445 EDT. Simulation of the actual event is referenced as the base case.

a.

b.

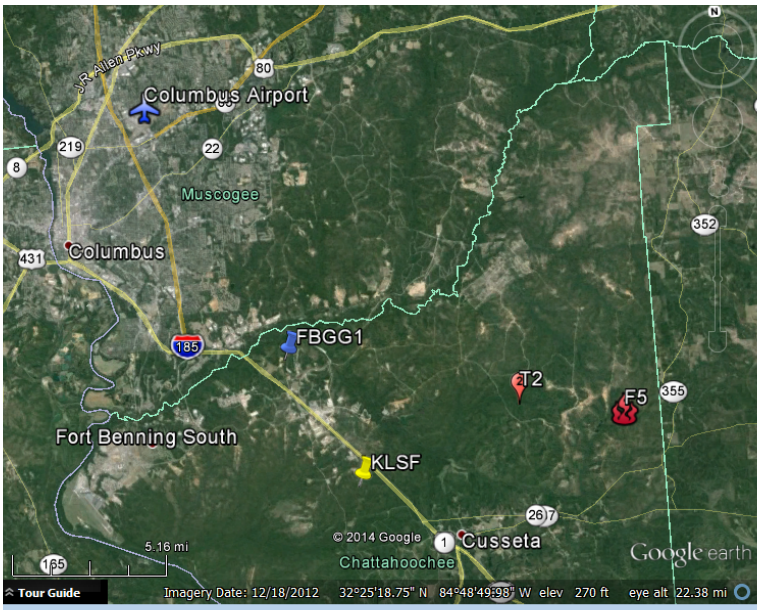

Figure 5.1: a) The 300-acre block (F5) burned on 9 April 2008. b) map of the studied sites: fire center (flame labeled F5), truck location (T2), meteorological stations (KLSF and FBGG1), and Columbus Airport (blue airplane)

Performance of the base case simulation was evaluated with the downwind $PM_{2.5}$ concentration measurements. The sampling truck (T2) was positioned between 2 and 5 km downwind from the burn site (Table 5.1). The experiment was designed so that the truck could be moved if and when wind shifted to blow smoke in different directions. The

latitudes and longitudes of truck locations were measured by the sampling crew using GPS units. The crew also took field notes regarding map locations and times the truck moved during the burn. DustTrak $PM_{2.5}$ sampler on the truck measured the concentration every minute for the duration of the burn on the truck. Hourly $PM_{2.5}$ concentrations at a nearby airport, Columbus Airport, was obtained from Georgia Department of Natural Resources, Environmental Protection Division Ambient Monitoring Program (http://www.georgiaair.org/amp/).

Table 5.1: $PM_{2.5}$ concentration sampling locations, durations, and distances from the fire for the Fort Benning burn event on 9 April 2008.

Lat.	Lon.	Location Name	Time (EDT)	Dist. (km)
32.3535	-84.7125	Truck T2 P1	1212-1333	3.5
32.3518	-84.7012	Truck T2 P2	1340-1412	2.3
32.3580	-84.7140	Truck T2 P3	1425-1513	4.1
32.5163	-84.9389	Columbus Airport		31.0

5.3 Methods

The five scenarios studied changed the 1) age of fuelbed, 2) size of the burn, 3) type of ignition, 4) time of the burn, and 5) season of the burn. First, the base case simulation with a 3 year-old fuel loading was compared to a simulation with a 5 year-old fuel loading. The area of the burn was doubled in the second case. The two ignition types used for prescribed burning are hand-lit, (i.e., all terrain vehicles (ATVs) and torches are used to ignite the fuels), and aerial ignition, (i.e., golf-ball-sized fireballs are dropped from a helicopter to start the fire). Aerial ignition is faster, therefore the aerial ignition

scenario was simulated to have a shorter ignition time. The same burn was simulated with different start times: starting in the morning at 1030 EDT, base case at 1230 EDT, and afternoon at 1530 EDT. To study the effect of seasonal atmospheric conditions on a burn, the same burn was simulated for a winter case using meteorological data from 11 January 2007 and a summer case with data from 2 July 2007.

The emissions and plume dispersion predictions were performed following the Bluesky framework. The key parameters that are different for each scenario are listed in Table 5.2 and are explained in the following sections.

Table 5.2: Values of the parameters differed in each scenario.

Scenario	Base case	5 year old fuel	Double burn area	Aerial ignition	Morning burn	Afternoon burn	Winter burn	Summer burn
Age of Fuel (year)	3	5	3	3	3	3	3	3
Plume core number	4	4	6	4	4	4	4	4
Area burned (ha)	121	121	242	121	121	121	121	121
Ignition time (EDT)	1230-1430	1230-1430	1230-1430	1230-1330	1030-1230	1530-1730	1230-1430	1230-1430
daily Max/Min Temp (F)	78/53	78/53	78/53	78/53	78/53	78/53	63/35	98/73
daily Max/Min RH (%)	89/36	89/36	89/36	89/36	89/36	89/36	66/42	84/29
modeled PBL (m)	950-1450	950-1450	950-1450	950-1450	400-1450	1450-300	350-750	1210-2230
Fuel Consumption (metric ton)	1470.42	1512.49	2914.67	1145.40	1138.17	1733.16	1528.34	1686.61
Heat release (GW)	3.25	3.36	6.52	3.05	3.00	3.47	3.30	3.43
$PM_{2.5}$ Emission (metric ton)	16.90	17.38	33.50	13.16	13.08	19.92	17.57	19.39
Max Fire Diameter (m)	41.23	41.95	58.25	52.32	40.59	43.93	41.88	43.47

5.3.1 Fuel Loading

Fuel loading at Fort Benning was previously studied by *Achtemeier et al.* [2011] and the results for 3 and 5 years old fuels are shown in Table 5.3. Since tall long leaf pines dominate Fort Benning, much of the live fuels were woody fuels and shrubs growing underneath. Litter, such as fallen pine needles, and duff available on ground were what drove the burn. The base case used the fuel loading for 3 years old and the 5 year old fuel loading was used in the first scenario case studying the effect of the age of fuel.

Table 5.3: Fuel loading at Fort Benning, GA by different fuel age, separated by fuel types (in tons/acre).

	Canopy	Shrub	Grass	Woody	Litter	Duff
3 yr old fuel	0.00	2.47	0.20	3.13	3.17	2.08
5 yr old fuel	0.00	2.75	0.23	4.01	2.66	2.55

5.3.2 Fuel Consumption/ Heat Release

Fuel consumption and heat release were calculated for fire emissions and plume transport parameters. Fire Emission Production Simulator, FEPS (introduced in Chapter 2), was used to obtain hourly fuel consumption and heat release rates. The fuel loadings from above were input to FEPS. Fuel moisture for all simulations was assumed to fit the moderate condition in FEPS. Since this was a prescribed burning case with litter and duff being consumed the most, the burn was thought to be efficient with 95% flaming

involvement and 5% smoldering involvement. For all cases but aerial ignition, it was assumed that 97% of the total burn area was burned in the first two hours and smoldered 3% of the total area in the third hour. For the aerial ignition case, 80% of the total area was burned in the first hour and the remaining 20% was burned during the smoldering stage in the second hour. This resulted in less fuel consumed compared to the base case. Since FEPS assumes all simulations start at the top of the hour, ignition times were rounded down from the times listed in Table 5.2.

The modeled meteorology was compared against the hourly data recorded at Fort Benning station KLSF (32.333 ^{o}N, 84.833 ^{o}W), which was the closest to the fire center. The data were obtained from ROMAN (http://raws.wrh.noaa.gov/roman/). The recorded hourly wind speeds and maximum and minimum temperature and relative humidity were input to FEPS.

5.3.3 Emission and Fire Diameter Rates

Emission rates of different species were calculated by multiplying the fuel consumption rates from FEPS by the species specific emission factors from *Achtemeier et al.* [2011], which are also listed in Table 5.4. The hourly fuel consumption from the flaming phase was multiplied by species-specific emission factor for flaming phase, and the smoldering fuel consumption was multiplied by the smoldering phase emission factor. The $PM_{2.5}$ emissions from flaming phase and smoldering phase were combined for every hour to get the emission rates used in the dispersion model. The total $PM_{2.5}$ emissions for each burn case are listed in Table 5.2. Modified combustion efficiency (MCE) was also calculated for fire behavior analysis. MCE is the ratio of CO_2 to the sum of all the calculated carbon species, and it is used to quantify the relative amounts of flaming and

smoldering combustion. MCE is larger for the flaming phase (>0.9) than for the smoldering phase [*Ward and Hardy*, 1991].

Table 5.4: Average emission factors from southeastern prescribed fires [*Achtemeier et al.*, 2011].

Chemical Species	**Emission Factor (g/kg)**	
	Flaming Combustion	Smoldering Combustion
CO_2	1664.00	1649.00
CO	82.00	106.00
CH_4	2.32	3.42
C_2H_4	1.30	1.30
C_2H_2	0.50	0.48
C_2H_6	0.32	0.46
C_3H_6	0.51	0.59
C_3H_8	0.09	0.11
C_3H_4	0.05	0.05
NMHC	2.77	3.00
$PM_{2.5}$	11.51	10.45

The heat release rate from FEPS was applied to a heat flux equation that connects heat flux to burn area size (Equation 15 from *Achtemeier et al.* [2011] and Eqn. 2 from Chapter 3). The fire diameter is calculated assuming that the plume core diameter is circular. The default vertical wind speed in Daysmoke is 25 m/s and this vertical wind speed was used in all of fire diameter calculations. The largest hourly fire diameters calculated from the equation are listed in Table 5.2.

5.3.4 Plume Dispersion Modeling

Gridded meteorological data used in plume dispersion modeling was simulated by the Weather Research and Forecasting model (WRF). WRF simulated meteorology for three different days (i.e., base case date, winter case, and the summer case) near Fort

Benning in a 90 km by 93 km domain. Meteorological fields produced by WRF were nested to 1 km resolution with 34 vertical sigma layers that increase in thickness by height.

Daysmoke coupled with adaptive grid CMAQ was used to simulate plume growth and transportation. The hourly emission rate and hourly fire diameter derived from FEPS outputs were included in Daysmoke. Daysmoke carried the smoke plume until the plume was 16 km away from the fire, which is the distance Daysmoke was designed to carry the plume up to. Beyond 16 km downwind, the plume was carried by CMAQ. The CMAQ grid was adapted to the $PM_{2.5}$ concentration emitted from the burn. The plume concentrations were written out every 15 minutes.

The base case simulation was verified with measured wind speed and ground level $PM_{2.5}$ concentrations downwind. WRF-predicted wind speeds were compared against hourly-recorded wind speeds at FBGG1 (32.3967 ^{o}N, 84.8700 ^{o}W) located downwind in between the fire center and Columbus Airport. Plume dispersion near the burn site was verified with concentrations measured by the trucks from Table 5.1 and the local plume transport was verified at Columbus airport, which was 31 km downwind. Each of the cases were analyzed individually relative to the base case for changes in the total emission, plume height and the maximum ground level $PM_{2.5}$ concentration downwind. Plume height, or the height of the plume centerline, was calculated assuming a Gaussian distribution. Since the plume did not travel in the same direction for all simulations, maximum ground concentrations were extracted at any location along the arc that is 20 km and 31 km away from the fire.

5.4 Results and Discussion

5.4.1 Simulation Verification

WRF predicted the wind direction southeasterly, which was in agreement with the observations at FBGG1. Wind speed was overestimated by WRF, especially after 1400 EDT (Figure 5.2). The average wind speed observed for the duration of the burn was 2.3 m s^{-1} whereas WRF predicted the average wind speed to be 3.5 m s^{-1}. The difference in wind speed affected the timing of the peaks arriving to the measurement sites as well as the magnitude of the peak.

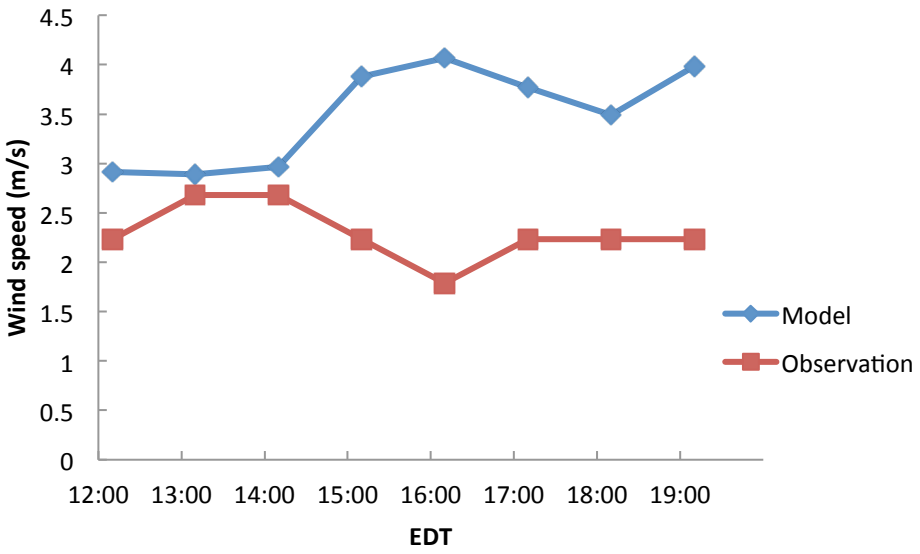

Figure 5.2: Observed and simulated wind speed at FBGG1 (32.3967 ^{o}N, 84.8700 ^{o}W) on 6 April 2009.

Short range $PM_{2.5}$ transport by the model was compared with the measurements from the truck (Figure 5.3a). Both the measured and modeled data were averaged for every 30 minutes, and measurement averages excluded the data collected while the truck was traveling. The smoke arrived at 1345 EDT both in the model and the observed

measurements. The background concentration in the model was slightly lower than the observed measurements, by 5.5 μg m^{-3}. When the background concentration difference is taken in account, the model overestimated the concentration increase by 25.7μg m^{-3}, and the mean fractional error for the duration of the comparison was 56%.

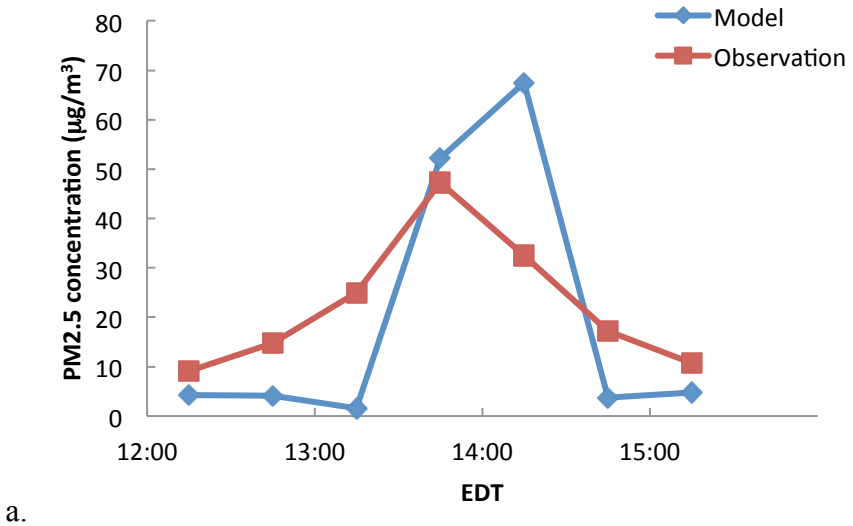

a.

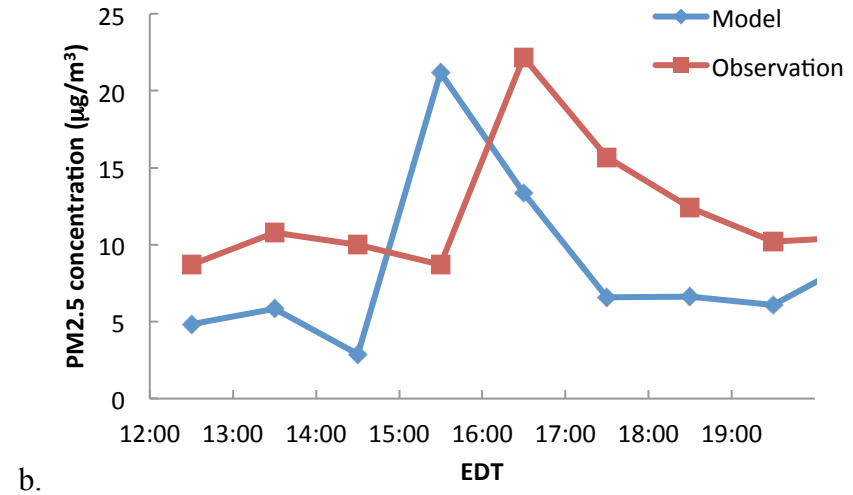

b.

Figure 5.3: Observed and simulated $PM_{2.5}$ concentration at a) short range at the truck and b) long range at Columbus Airport on 6 April 2009.

Long range transport evaluations were done at Columbus Airport (Figure 5.3b). The $PM_{2.5}$ concentration was recorded hourly at the airport, therefore the comparison was done hourly as well. The 1.2 m s^{-1} overestimation corresponds to the smoke plume arriving to the airport 1.3 hours earlier than what the measurements suggested, and this effect is observed with the modeled peak arriving an hour earlier. Modeled background concentration was slightly lower at 6.0 μg m^{-3} compared to the observed background concentration at 9.9 μg m^{-3}. If the difference in background concentration is considered, the modeled concentration increase from the fire was 15.2 μg m^{-3}, an overestimation of 2.0 μg m^{-3}. When the modeled concentration was shifted an hour behind, the mean fraction error compared to the observation was 51%.

5.4.2 Scenarios

Adaptive grid Daysmoke-CMAQ simulated the differences in each scenario (Figure 5.4). The grids adapted heavily towards the center of the fire, and continued to adapt to the plume even after the plume reached 16 km away. Once the portion of the plume beyond 16 km was handed over to CMAQ, the plume was mixed rapidly throughout the PBL as shown by the smoother and higher iso-surface in Figure 5.4. Table 5.5 lists plume heights and the maximum downwind $PM_{2.5}$ concentrations that were predicted.

Table 5.5: Plume heights and maximum $PM_{2.5}$ concentrations observed on ground for each prescribed burning case.

	base	5 year	double area	aerial	morning	afternoon	winter	summer
MCE	0.70	0.70	0.70	0.80	0.80	0.65	0.68	0.66
Plume top height (m)	1350	1450	1680	1620	1250	1400	860	1830
Cmax 20km ($\mu g/m^3$)	56.0	55.1	95.9	39.8	60.6	164.3	22.8	73.6
Cmax 31km ($\mu g/m^3$)	38.0	41.1	74.9	26.5	38.3	97.4	22.2	21.2

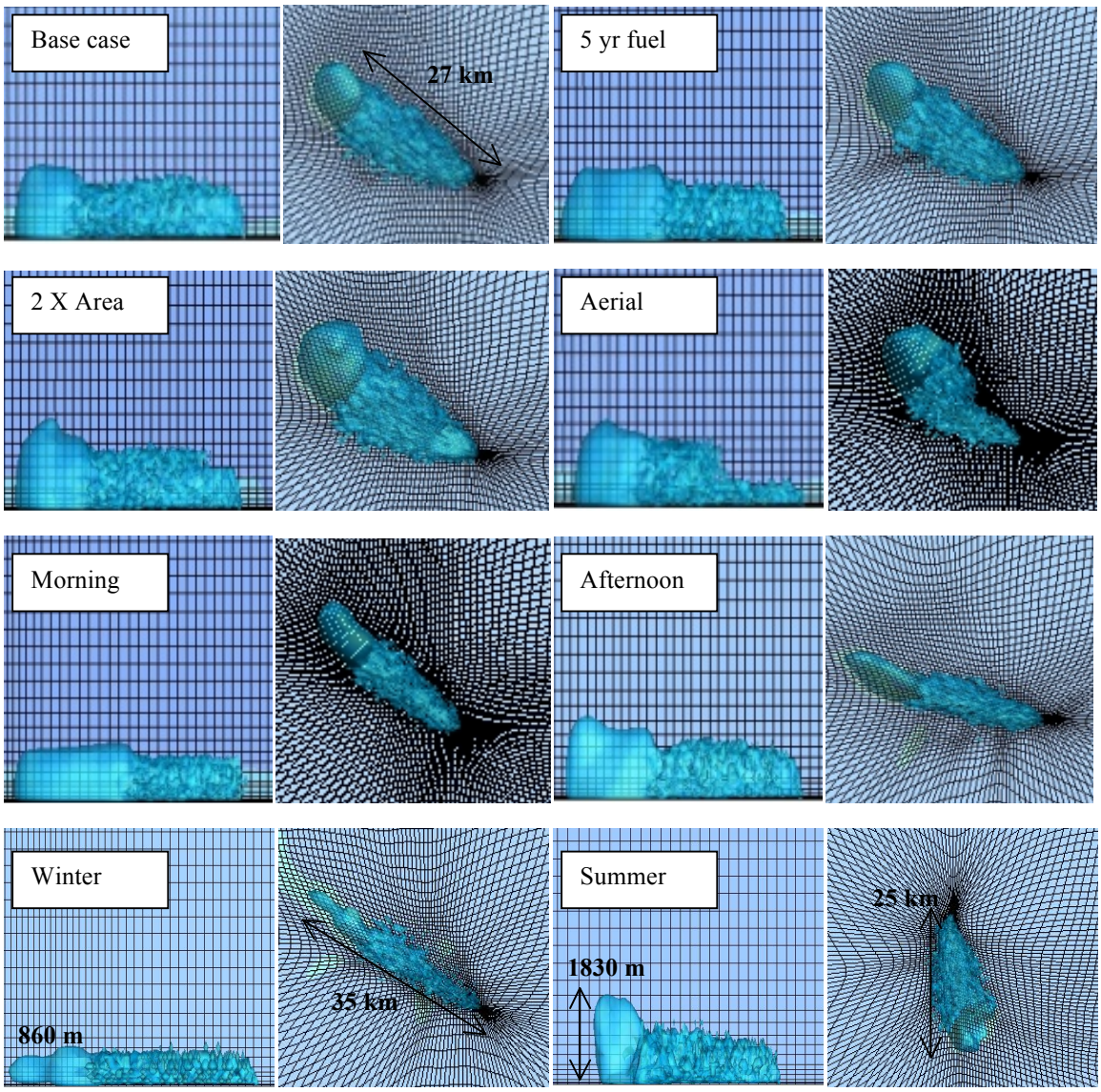

Figure 5.4: Snap shots of the plume 2 hours after ignition. Side view of the plume on the left and Bird's eye view on the right for each scenario labeled in white box. Iso-surface at 20 μg/m^3. Figure resolution stays the same as the base case except for those labeled.

5.4.2.1 Age of fuelbed

The major difference between the base case with the 3 year old fuel and the 5 year old fuel case before going into Daysmoke-CMAQ was the amount of fuel consumed, which also affects heat release, fire diameter, and the total $PM_{2.5}$ emitted. The 5 year old fuel case consumed 3% (42.07 tons) more fuel and increased $PM_{2.5}$ emission by 3% as

well. MCE remained the same at 0.70, but the slight increase in fuel consumption in the 5 year old fuel case , resulting in larger heat flux/fire diameter, increased the plume height (by 100 m at 1430 EDT). The maximum downwind concentration at Columbus Airport increased by 8% with respect to base case. For this burn case, the age of fuel between 3 and 5 years did not have a significant effect on the amount of emissions and the downwind concentrations.

5.4.2.2 Burn area

For the case where the area of the burn increased by two folds, the plume core number was set as 6 instead of 4 considering the larger burn area. The amount of fuel consumed and the total emission also doubled with the size. The maximum fire diameter increased by 41% (17.0 m). The MCE remained the same. The plume height and the ground concentrations downwind were significantly affected in the case with double the burn area. The top of the plume reached above the planetary boundary layer, which was about 1300 m at noon. The maximum concentration 20 km downwind reached up to 95.9 $\mu g\ m^{-3}$. The maximum concentration at 31 km downwind was 74.9 $\mu g\ m^{-3}$, which was twice the maximum concentration from the base case. These concentration levels are too high and may have adverse effects on human health; therefore, the area of the burn is clearly a critical factor in controlling the downwind concentrations.

5.4.2.3 Ignition type

The two types of burning methods, hand lit and aerial ignition, have a few large differences in prescribed burning management. Hand lit ignition requires more personals and is time consuming since the crew must go out in the field and light rows of fire by hand for hours depending on the burn condition and size. With aerial ignition, one can

finish igniting the burn area faster, but it is not cost effective unless the area of the burn is large enough to compensate for the cost of human labor. Aerial ignition was represented in the simulation by having 1 hour shorter ignition time compared to hand lit or base case. Aerial ignition case's fuel consumption and $PM_{2.5}$ emissions were both 22% less than the base case with a higher MCE at 0.8 due to faster, shorter ignition with less smoldering. Since most of the area was burned in the first hour, fire diameter increased to 52.3 m, a 27% increase compared to the fire diameter for the base case. As a result, the larger fire diameter allowed the plume to rise above the PBL. The majority of the plume remained aloft as it traveled downwind, leading to around 30% lower maximum concentrations at 20 km and 31 km downwind. Aerial ignition simulation was the only case where the emissions and downwind concentration peaks decreased compared to the base case.

5.4.2.4 Time of the day

Since the base case started at noon, a case in the morning (i.e., igniting two hours earlier) and another in the afternoon (i.e., igniting three hours later) were studied. The relative humidity was higher and the ambient temperature was lower in the morning, which led to lower fuel consumption. MCE increased to 0.80 and the total emissions decreased by 23%. Despite the increase in combustion efficiency and the decrease in total emissions, the ground concentration at 20 km downwind increased by 10%. The PBL increased throughout the morning starting at 600 m. The plume rose higher with increasing PBL throughout the burn, reaching up to 100 m less than the base case.

The afternoon burn started around the hottest and driest time of the day. The drier environment allowed the fuel consumption and the total emissions to increase by

18%, and MCE decreased by 7%. The plume reached up to 1400 m at the beginning of the burn, but as the sun went down and so did the ambient temperature and PBL, as well as the plume height. The concentration increased by 98% at 20 km downwind and the concentration increased by 88% at 31 km downwind. The afternoon case showed a significant effect of low PBL height on to downwind concentration.

5.4.2.5 Season

Winters in southeast US tend to be colder and drier. The meteorological conditions for the selected date for the winter case did have a lower maximum relative humidity at 66% compared to 89% from the base case. This affected the smaller fuels to be dry, leading to more fuels being consumed by the fire. The fuel consumption and total emissions for the winter case slightly increased from the base case, both by 4%. The difference in MCE was only -2%. The simulated plume for the winter case reached 860 m above ground, yet the plume reached above PBL since PBL is typically lower in winter. Although the wind direction on this day was similar to the base case, the wind speed was more than doubled (Figure 5.5). With the plume reaching the free troposphere and being transported at a higher wind speed (longer extent of the plume in bird's-eye view in Figure 5.4), $PM_{2.5}$ concentrations on the ground remained lower than the base case by 42% at 31 km downwind and 59% at 20 km. Since this phenomenon occurs often in the winter with lower PBL along with other factors such as avoiding ozone season, many prescribed burnings are practiced between winter and spring.

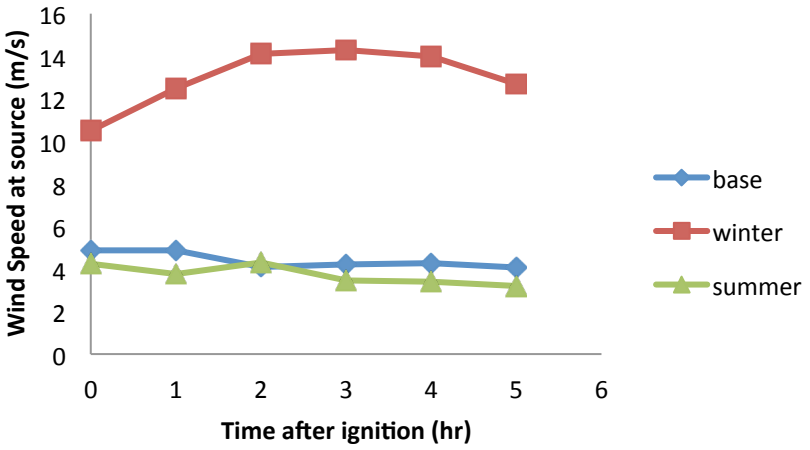

Figure 5.5: WRF predicted wind speeds during the 6 April 2009 burn at Fort Benning (base in blue), wind speed at the same location on 11 January 2007 (winter in red) and on 2 July 2007 (summer in green).

Summers in southeast US are much hotter than spring, often reaching up to 90 $^{\circ}F$. The chosen summer day had slightly drier (6 to 10% lower) relative humidity compared to the base case but temperature was higher with respect to the base case by 20 $^{\circ}F$. The fuel consumption and total emissions were higher by 15% due to drier and hotter condition, and MCE was lower by 6% from base case which indicates an increase in smoldering emissions and/or incomplete combustion. Although the selected summer day had similar wind speed as the base case (Figure 5.5), the wind direction differed with winds blowing from the north at the beginning of the burn (Figure 5.4). The summer case had the highest plume height at 1830 m above ground (36% higher from base case) but this was not enough to reach above PBL, which was at 2230 m above ground. At 20 km downwind right after where Daysmoke plume is handed over to CMAQ, the ground concentration increased by 31%. On the other hand, the ground concentration at 31 km downwind decreased for the summer case. One factor leading to a lower ground

concentration may be due to simulated winds direction drastically shifting to easterly right before the plume reached 31 km downwind. Another reason may be the strong vertical mixing of the smoke concentration once the plume entered CMAQ.

5.5 Conclusion

Different scenarios of prescribed burning were studied through adaptive grid Daysmoke-CMAQ. Changes in environmental conditions affected the amount of fuel consumed, pollutants emitted, combustion efficiency, plume transport, and the downwind concentrations. For the fuel types in the studied regions, the difference in total emission and downwind concentration between 3-year and 5-year fire return interval were higher by less than 8%. As the area of the burn doubled, so did the emissions as well as the downwind smoke concentration. Land managers should carefully choose the burn size since the size does affect the concentration spikes downwind. The simulation of aerial ignited burn emitted less pollutant and burned efficiently that the plume reached above PBL and the concentration on the ground level was lower than the base case. Burns in the morning emit less $PM_{2.5}$ due to higher relative humidity and higher fuel moisture, but the concentrations downwind can still be large if the plume remains within the PBL with less mixing volume in the atmosphere in the morning. The afternoon burn case simulated the dangerous situation where the plume got trapped in PBL as its height decreased at night. Winter was more favorable compared to spring and summer because the plume traveled above the typically lower PBL. Daysmoke-CMAQ was able to simulate the different burn scenarios, showing the effect of environmental and fire behavior changes on downwind concentrations. Daysmoke-CMAQ has the potential to be used to forecast fire events by including forecasted weather parameters and other forecasted input factors into

Daysmoke-CMAQ. This will provide practical applications of Daysmoke-CMAQ to aid land managers with their burn plans and I hope to build this in near future.

5.6 References

Achtemeier, G., S. Goodrick, Y. Liu, F. Garcia-Menendez, Y. Hu, and M. Odman (2011), Modeling Smoke Plume-Rise and Dispersion from Southern United States Prescribed Burns with Daysmoke, *Atmosphere*, *2*(3), 358-388, doi:10.3390/atmos2030358.

Carlson, J., and R. Burgan (2003), Review of users' needs in operational fire danger estimation: the Oklahoma example, *International Journal of Remote Sensing*, *24*(8), 1601-1620.

Hurteau, M., and M. North (2008), Fuel treatment effects on tree-based forest carbon storage and emissions under modeled wildfire scenarios, *Frontiers in Ecology and the Environment*, *7*(8), 409-414.

Larkin, N. K., S. M. O'Neill, R. Solomon, S. Raffuse, T. Strand, D. Sullivan, C. Krull, M. Rorig, J. Peterson, and S. A. Ferguson (2009), The BlueSky smoke modeling framework, *International Journal of Wildland Fire*, *18*(8), 906-920, doi:10.1071/WF07086.

Reid, J. S., E. J. Hyer, E. M. Prins, D. L. Westphal, J. Zhang, J. Wang, S. A. Christopher, C. A. Curtis, C. C. Schmidt, and D. P. Eleuterio (2009), Global monitoring and forecasting of biomass-burning smoke: Description of and lessons from the Fire Locating and Modeling of Burning Emissions (FLAMBE) program, *Selected Topics in Applied Earth Observations and Remote Sensing, IEEE Journal of*, *2*(3), 144-162.

Sullivan, D. C., S. M. Raffuse, D. A. Pryden, K. J. Craig, S. B. Reid, N. J. Wheeler, L. R. Chinkin, N. K. Larkin, R. Solomon, and T. Strand (2008), Development and applications of systems for modeling emissions and smoke from fires: the BlueSky smoke modeling framework and SMARTFIRE, paper presented at 17th International Emissions Inventory Conference.

Ward, D. E., and C. C. Hardy (1991), Smoke emissions from wildland fires, *Environment International*, *17*(2), 117-134.

CHAPTER 6

Reactive Nitrogen Deposition over US National Parks: Sensitivity to Anthropogenic and Biogenic Emissions

Abstract

Deposition of reactive nitrogen species has been increasing due to nitrogen emissions from human activities such as fuel combustion and agriculture. Nitrogen deposition may affect the ecosystem when it exceeds an ecosystem-dependent critical load. Total nitrogen deposition was predicted for the year of 2010 using CMAQ chemical transport model over contiguous US at 36 km grid resolution and over four selected national parks at 4 km resolution. Seasonal concentrations and depositions predicted by CMAQ were within a factor of two when compared to the measurements. The spatial details of concentration and deposition were better captured with finer resolution, especially along the roads and mountains that the coarser grids could not simulate.

Nitrogen deposition sensitivities to major nitrogen emission sectors were studied at the national parks. Ammonia is primarily emitted from livestock manure, while nitrogen oxides are emitted from biogenic and mobile sources as well as power plants. The national parks near or downwind of city traffic were most sensitive to mobile emissions and severe enough that just the mobile source was enough to exceed the typical range of critical load values. At rural sites, nitrogen deposition was most sensitive to biogenic or agricultural emissions.

6.1 Introduction

Atmospheric deposition of nitrogen species has been increasing over the last few decades [*Aber et al*., 2003; *Ellis et al*., 2013; *Galloway et al*., 2003]. Deposited reactive nitrogen originates from ammonia (NH_3) and nitrogen oxides (NO_x) emissions from both anthropogenic and biogenic sources. Livestock, fertilizer, soils, and forest fires are some of the activities creating NH_3 emissions with livestock being the largest source category in the United States (US) [Anderson et al., 2003]. All combustion processes oxidize atmospheric N_2 and fuel nitrogen, creating NOx in the atmosphere. Biogenic NO_x emissions are mainly from lightening and soil. Reactive nitrogen species are formed from previously mentioned emissions via oxidation and/or phase change. Deposition of reactive nitrogen species has acidification impacts on soil and water, contributing to eutrophication [*Pardo et al*., 2011]. Therefore, nitrogen deposition poses a threat to ecosystems and can reduce biodiversity when it exceeds the critical load (CL) [*Stevens et al*., 2004]. In areas throughout the US, nitrogen deposition has been exceeding the CLs, which is typically between 2.5–5 kg N ha^{-1} yr^{-1} [*Ellis et al*., 2013].

CMAQ v5.0.1 with bidirectional exchange of NH_3 better characterizes atmospheric sinks and sources of NH_3 [*Bash et al*., 2013]. In this study, CMAQ v5.0.1 with bidirectional exchange of NH_3 was used to understand the sensitivity of reactive nitrogen deposition to emissions from domestic anthropogenic emissions and natural sources. The study identifies which nitrogen emission sectors (out of agricultural, biogenic, mobile, and power plants) contribute the most to deposition of reactive nitrogen species at four national parks; Joshua Tree (JOT), Grand Teton (GRT), Rocky Mountain (ROM), and Great Smoky Mountain (GSM) National Parks. The sensitivity analysis was

performed on NO_x emissions from mobile, power plants, and biogenic sources, and NH_3 emissions from livestock practices.

6.2 Input Data and Model Configuration

This study simulated nitrogen concentration and deposition using CMAQv5.0.1 with bidirectional NH_3 exchange over contiguous US (CONUS) and the four daughter domains covering the studied national parks for the year of 2010. CMAQ is an Eulerian air quality model that simulates aerosol chemistry and acidic/nutrient deposition for urban to continental scale domains. The Carbon Bond mechanism (CB05) [*Yarwood et al*., 2005] was applied in the simulations. The annual gridded meteorology was simulated by the Weather Research and Forecasting model (WRFv3) [*Skamarock et al*., 2008] using Pleim-Xiu land surface scheme [*Pleim and Xiu*, 1995]. Both WRF and CMAQ was configured with 13 sigma vertical layers and horizontal grid dimensions of 36 km X 36 km for the mother domain and 4 km X 4 km for the regional scale domains over the national parks.

The Sparse Matrix Operator Kernel Emissions (SMOKE) Modeling was used to calculate gridded temporal and spatial emissions from various sectors applied to CMAQ. The emissions inventory in SMOKE was based on the US National Emissions Inventory 2005 (NEI-2005). NEI emissions were grown to 2010 case using the method described in *Trail et al*. [2014]. The agricultural emission rates in SMOKE did not include fertilizer emissions since they were estimated separately in CMAQ through bidirectional exchange using outputs from an agricultural management model called Environmental Policy Integrated Climate (EPIC) model [*Cooter et al*., 2012]. The Fertilizer Emission Scenario Tool for CMAQ (FEST-C) [*Ran et al*., 2012] includes EPIC in the modeling tool, and

calculates fertilizer application rates, depths, and timing based on WRF meteorological data and land use data per grid cell for each day.

Model performance was evaluated by comparing simulated atmospheric nitrogen concentration and nitrogen deposition to actual measurements. Nitrogen deposition was separated into wet and dry forms, with wet deposition compared against NADP measurements and dry deposition compared against CASTNET estimates (Table 6.1). Wet deposition was corrected to include the bias of modeled precipitation by multiplying a correction factor of measured precipitation over modeled precipitation, which follows the method used in *Bash et al*. [2013]. The modeled reduced nitrogen species (NH_x) consisted of NH_3 and ammonium (NH_4^+) in aerosols. The oxidized nitrogen species (NO_y) included NO, NO_2, PAN, HNO_3 and NO_3^-.

Table 6.1: List of coordinates where the measurements were taken for concentration/wet deposition (NADP) and dry deposition (CASTNET) for each national park studied.

National Park	NADP NTN	LAT	LON	CASTNET	LAT	LON
JOT	CA67	34.0695	-116.3889	JOT403	34.0714	-116.3906
GRT	WY08	44.9166	-110.4203	PND165	42.929	-109.7878
ROM	CO19	40.3639	-105.581	ROM206	40.2778	-105.5453
GSM	TN11	35.6645	-83.5903	GRS420	35.6331	-83.9422

Nitrogen deposition sensitivity to four emission sectors was studied as well. Emissions from agricultural (mainly livestock and without fertilizer) NH_3, biogenic NO, mobile NO_x, and power plant NO_x were reduced by 20% individually for each studied case. The sensitivity (S) of specie i to each emission sector is expressed as

$$S_i = \frac{\partial Ndep_i}{\partial Emis} Emis = \frac{\Delta Ndep_i}{0.2} = 5 \times (Ndep_{i,base} - Ndep_{i,reduced\ emis})$$

where $Emis$ is the total amount of nitrogen species emitted in the domain, $\partial Emis$ is the difference in total emissions between the base case and the case with reduced emission from a specific sector, $Ndep$ is the amount of deposition of the studied specie. The simulated sensitivities from 4 km grid domains were analyzed by monthly to understand the effect of the studied emission sectors.

6.3 Results and Discussion

6.3.1 Surface Concentration

The nitrogen species with the three most abundant concentrations in the atmosphere (i.e., ammonium, nitric acid, and nitrate) were studied. The annually averaged concentrations simulated in 36 km and 4 km domains were compared against measurements at or near the studied parks (Figure 6.1). Simulations with higher resolutions reduced the overestimation of the total nitrogen available in the atmosphere, except at the ROM measurement site. Simulated nitric acid is overestimated while nitrate was underestimated by the models except at GSM. The annual ammonium concentration was more in agreement with measurements than the oxidized nitrogen concentrations at all four national park sites.

Increasing the grid resolution also increased nitric acid concentration and decreased nitrate concentration for all sites. This increase in ratio between nitric acid to nitrate reduced the error at GSM but not for the rest of the sites. Nitric acid was overpredicted by 10% to 112% and nitrate was underpredicted by 69% to 88%.

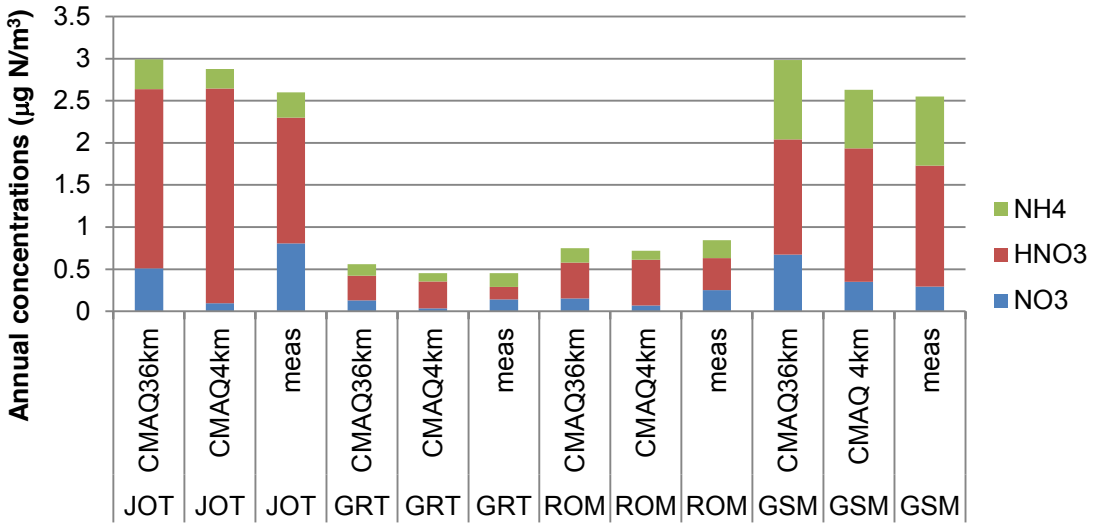

Figure 6.1: Annually averaged concentration for NO_3 (blue), HNO_3 (red), and NH_4 (green) obtained from CMAQ simulations with 36 km grid size, 4 km grid size and measurements from NADP at Joshua Tree (JOT), Grand Teton (GRT), Rocky Mountain (ROM), Great Smoky Mountain (GSM) National Parks.

6.3.2 Deposition Patterns

Annual spatial nitrogen emission and deposition across CONUS are shown in Figure 6.2. NH_3 emissions are localized to regions with cities or agricultural practices (i.e., Midwest, Carolinas, inland of California). NH_3 and NH_4^+ depositions tend to remain near emitted regions. NOx is emitted most in regions with higher population; concentrations are especially higher in major cities. Oxidized nitrogen deposition, unlike reduced nitrogen deposition, transported farther from the source and dispersed wider throughout eastern US and along the west coast. Nitrogen emissions from the northeast US are deposited over the Atlantic Ocean, which could alter the nitrogen cycle in aquatic systems [*Howarth et al*., 1996].

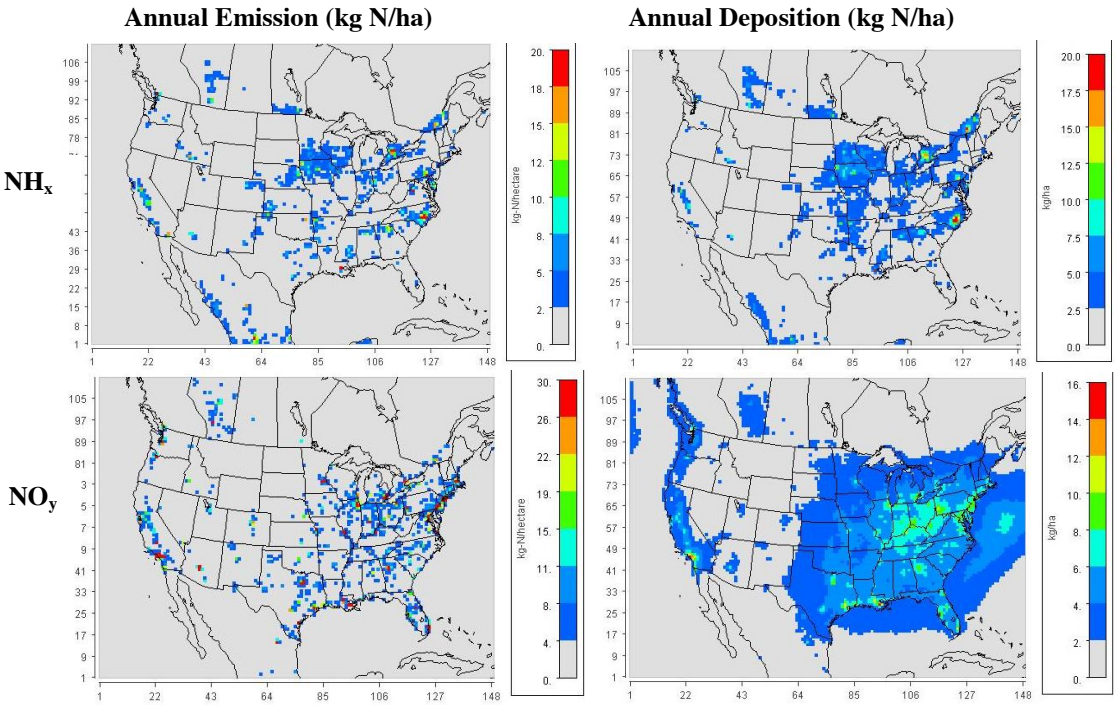

Figure 6.2: Annual nitrogen emission without fertilizer NH_3 emission (left) and deposition (right) for reduced (top) and oxidized nitrogen species (bottom).

Emissions and depositions of the reduced nitrogen species over the studied national parks are shown in detail in Figure 6.3. Reduced nitrogen emissions are higher along the streets (black lines) and agricultural lands (southeast corner in JOT domain, north of Denver in ROM domain, and north Georgia in the GSM domain). The amount of reduced nitrogen deposition is correlated with the amount of emissions with higher deposition in cities or agricultural areas in 4 km domain simulations. The deposition gradient is higher near mountains where GRT and GSM National Parks are located even though there is not a significant nitrogen emission in these parks. NH_3 emissions from nearby regions are being deposited over mountains with greater precipitation. In the Rocky Mountains winds typically blow west to east, therefore, mobile, oil and mining, and agricultural emissions in the city do not get deposited around ROM. The accuracy in CMAQ performance was dependent on the grid resolution since the higher deposition

gradient along the roads and mountains is captured in the 4 km grid simulations but not apparent in the coarser domain.

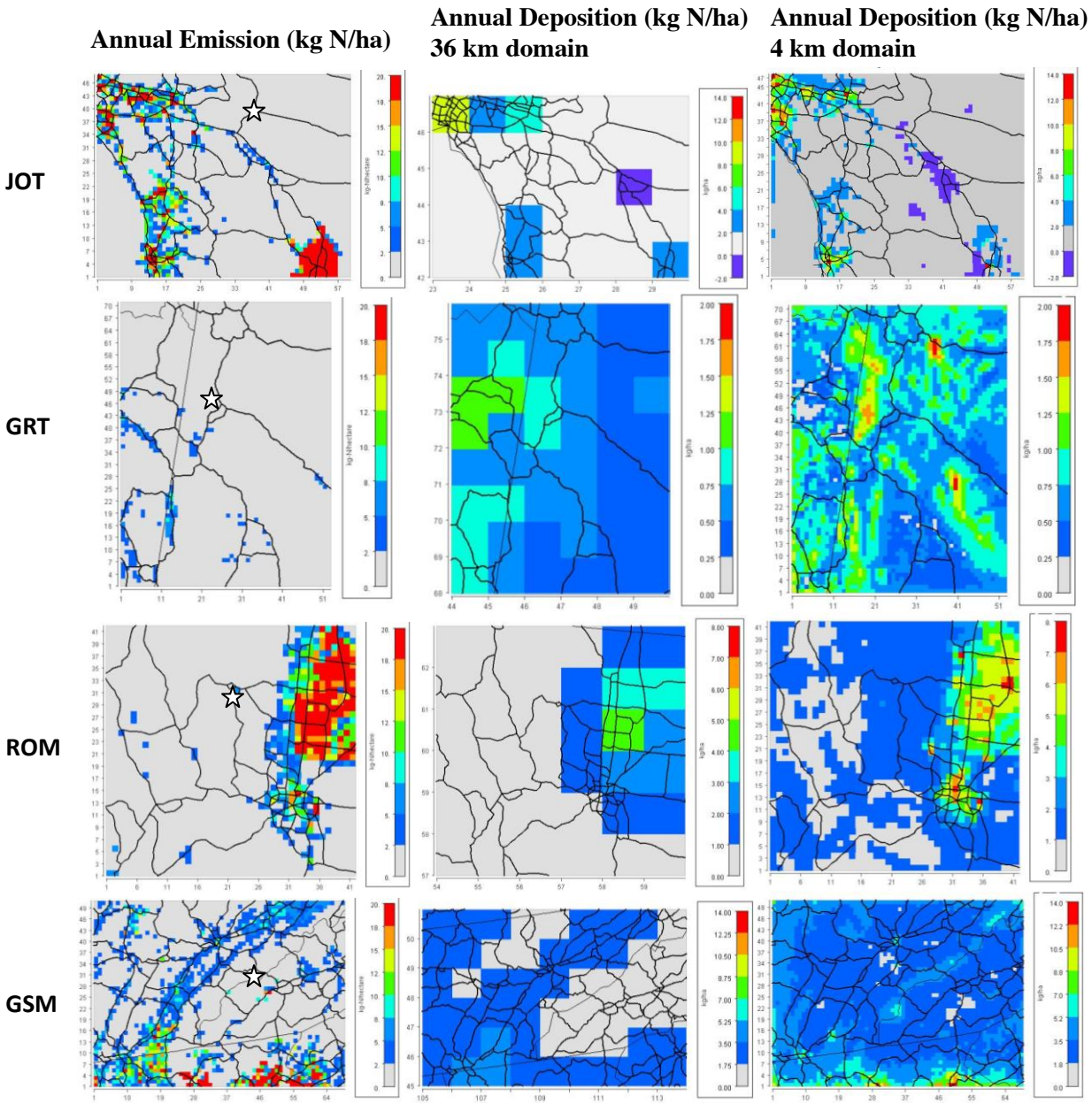

Figure 6.3: Annual NH_3 emissions (left) and reduced nitrogen deposition predicted by 36 km grid domain (middle) and by 4 km domain (right) for the four studied national parks: Joshua Tree (JOT), Grand Teton (GRT), Rocky Mountain (ROM), and Great Smoky Mountain (GSM). Stars label the national parks.

Emissions and depositions of the oxidized nitrogen species over the studied national parks are shown in Figure 6.4. Oxidized nitrogen emissions are higher along the streets (black lines) and especially higher in the cities. Similar to reduced nitrogen deposition, higher emissions of oxidized nitrogen deposition is apparent in the cities in 4 km domain simulations. NO_x emissions from nearby roads are being deposited over the mountains with greater precipitation similar to GRT and the GSM National Parks. Although Los Angeles is a bigger city than Knoxville, city emissions contributed most at GSM. The simulation using 36 km resolution over JOT overestimated nitrogen deposition along the coast compared to the 4 km resolution. The results from coarser grid cells severely underestimated the deposition near Denver compared to the results from finer resolution, again proving that 36 km resolution was not able to sufficiently predict the deposition field in detail. The rest of the analyses at the national parks are performed on results from 4 km grid simulations.

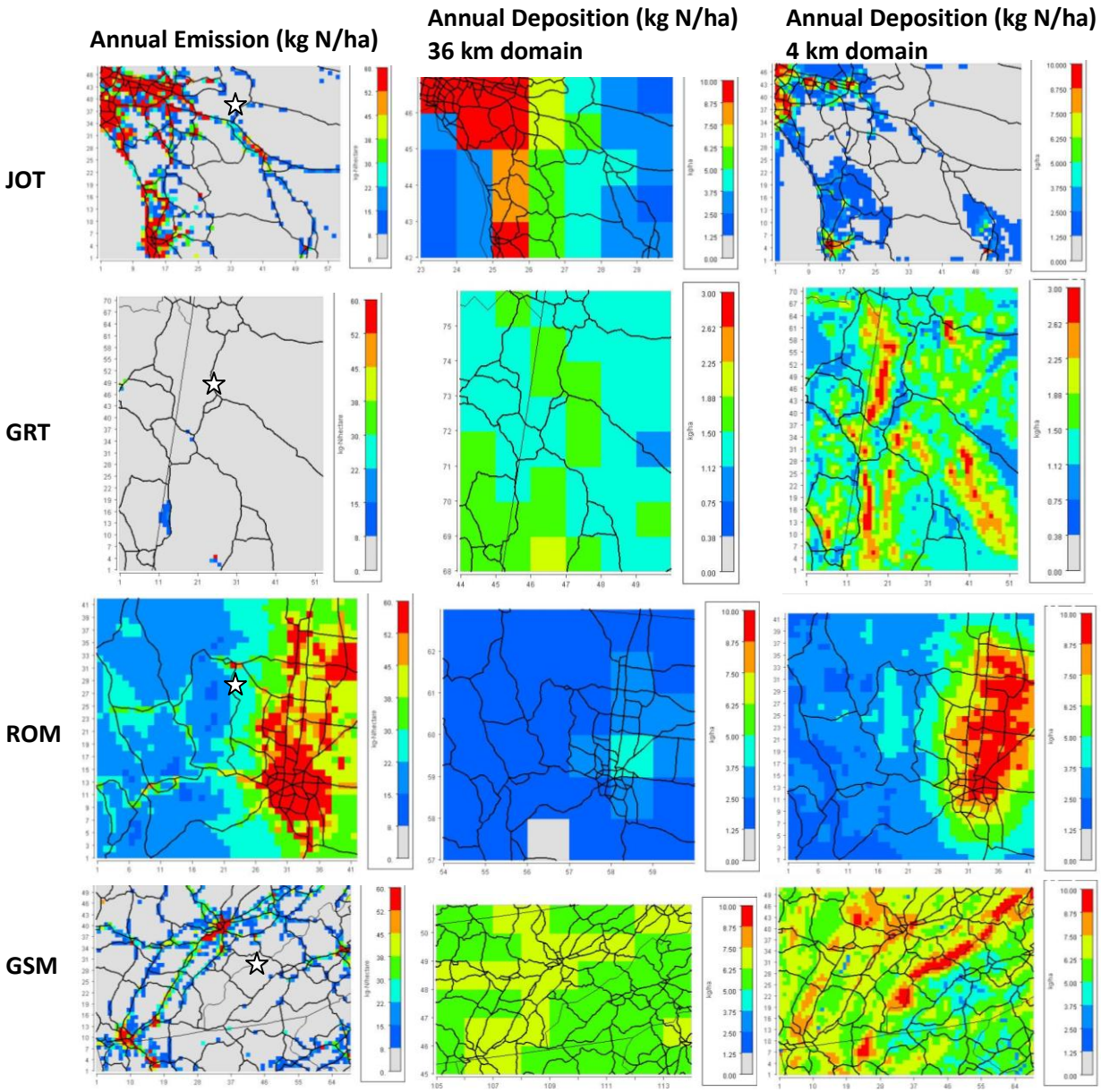

Figure 6.4: Annual NO_x emissions (left) and oxidized nitrogen deposition predicted by 36 km grid domain (middle) and by 4 km domain (right) for the four studied national parks: Joshua Tree (JOT), Grand Teton (GRT), Rocky Mountain (ROM), and Great Smoky Mountain (GSM). Stars label the national parks.

Seasonally measured deposition and precipitation are compared at the measurement sites in or near the studied national parks in Figure 6.5. The model underestimated wintertime precipitation at all studied parks. Overall, CMAQ predicted precipitation remained within 20% of measured precipitation values. The precipitation

correction to the amount of wet deposition reduced the error between the CMAQ-modeled deposition and NADP measured deposition for all sites expect GSM. The correction led to overestimation of wet deposition when precipitation was underestimated and vise versa at GSM. Generally wet deposition at all four sites was underestimated while dry deposition was overestimated. CMAQ also captured the increase in dry deposition during warm seasons as CASTNET estimates suggest at all four studied sites. However, CMAQ was not in agreement with CASTNET on the amount of HNO_3 and NH_4 dry depositions and predicted amount deposited to be double of what CASTNET estimated for most of the seasons.

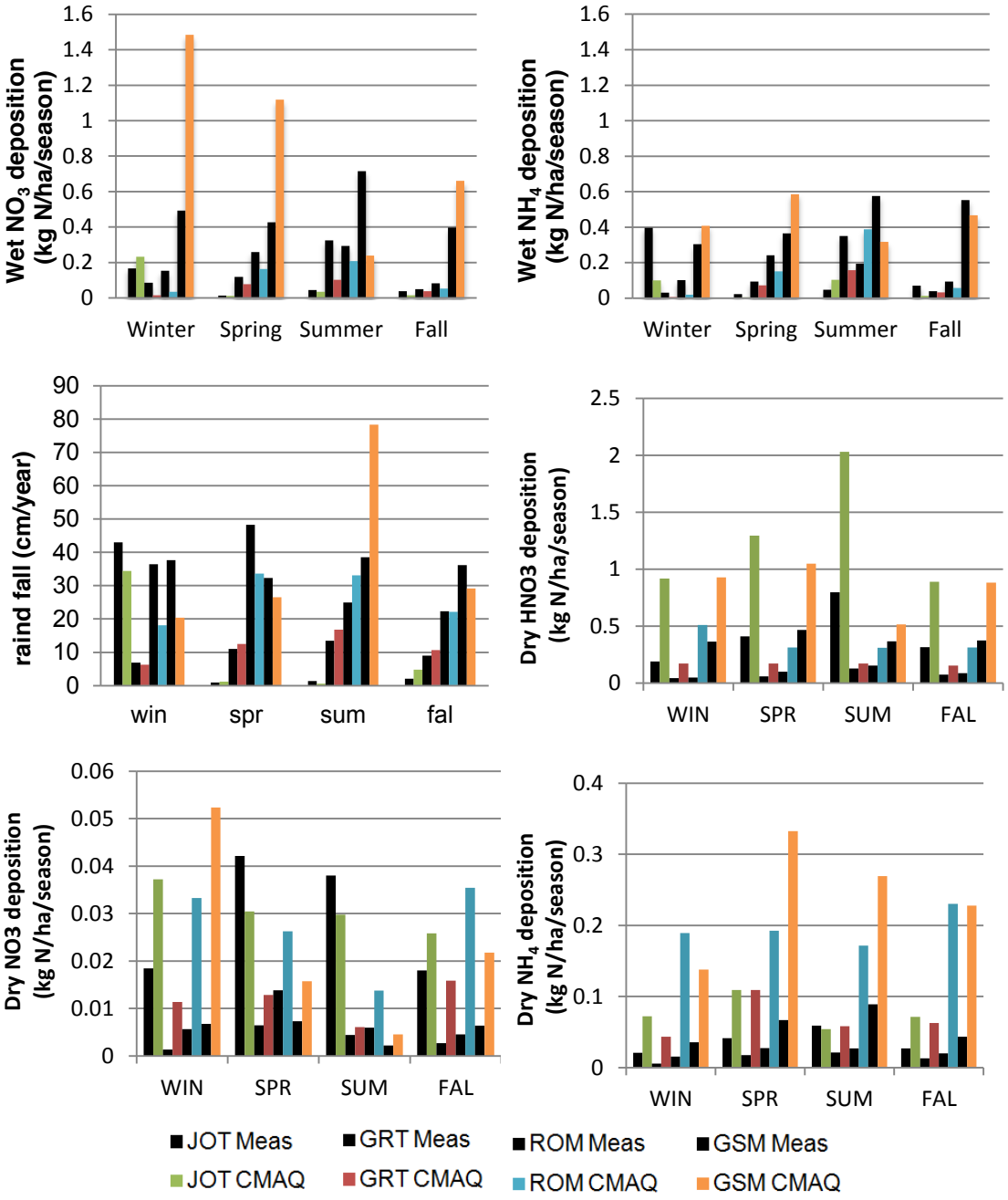

Figure 6.5: Seasonal wet NO_3 (top left), wet NH_4 (top right) deposition, precipitation (bottom left), and dry HNO_3 (top left), dry NO_3 (top right), dry NH_4 (bottom left) deposition obtained from CMAQ simulations with 4 km grid size and measurements from NADP/CASTNET at Joshua Tree (green), Grand Teton (red), Rocky Mountain (blue), Great Smoky Mountain (orange) National Parks.

6.3.3 Reactive Nitrogen Deposition Sensitivity to Emission Sectors

CMAQ predicted monthly nitrogen depositions at the national parks are shown in Figure 6.6. For all sites but GSM, total nitrogen deposition peaked in the summer months. At both ROM and GRT, the monthly deposition increased over the summer because wet deposition increased for those months. At GSM, wet deposition decreased in the warmer months, resulting in lower total nitrogen deposition for the summer. At GSM and JOT, the minimum CL is about 3 kg N ha^{-1} yr^{-1} [*Ellis et al*., 2013; *Pardo et al*., 2011]. CMAQ predicted GSM to have the largest annual total nitrogen deposition at 10.2 kg N ha^{-1} yr^{-1}, which is triple the CL, followed by JOT with 6.9 kg N ha^{-1} yr^{-1}, which is double the CL. Nitrogen deposition over JOT was mostly in dry form due to the lack of precipitation, and nitric acid was the dominant species. ROM had total nitrogen deposition of 5.0 kg N ha^{-1} yr^{-1}, which is double the minimum CL of 2.5 kg N ha^{-1} yr^{-1} [*Ellis et al*., 2013; *Pardo et al*., 2011]. GRT was the only site not exceeding the CL (2.5 kg N ha^{-1} yr^{-1} [*Ellis et al*., 2013; *Pardo et al*., 2011]) at 1.4 kg N ha^{-1} yr^{-1}. Monthly nitrogen deposition sensitivities to different emissions sectors are studied in the following sections.

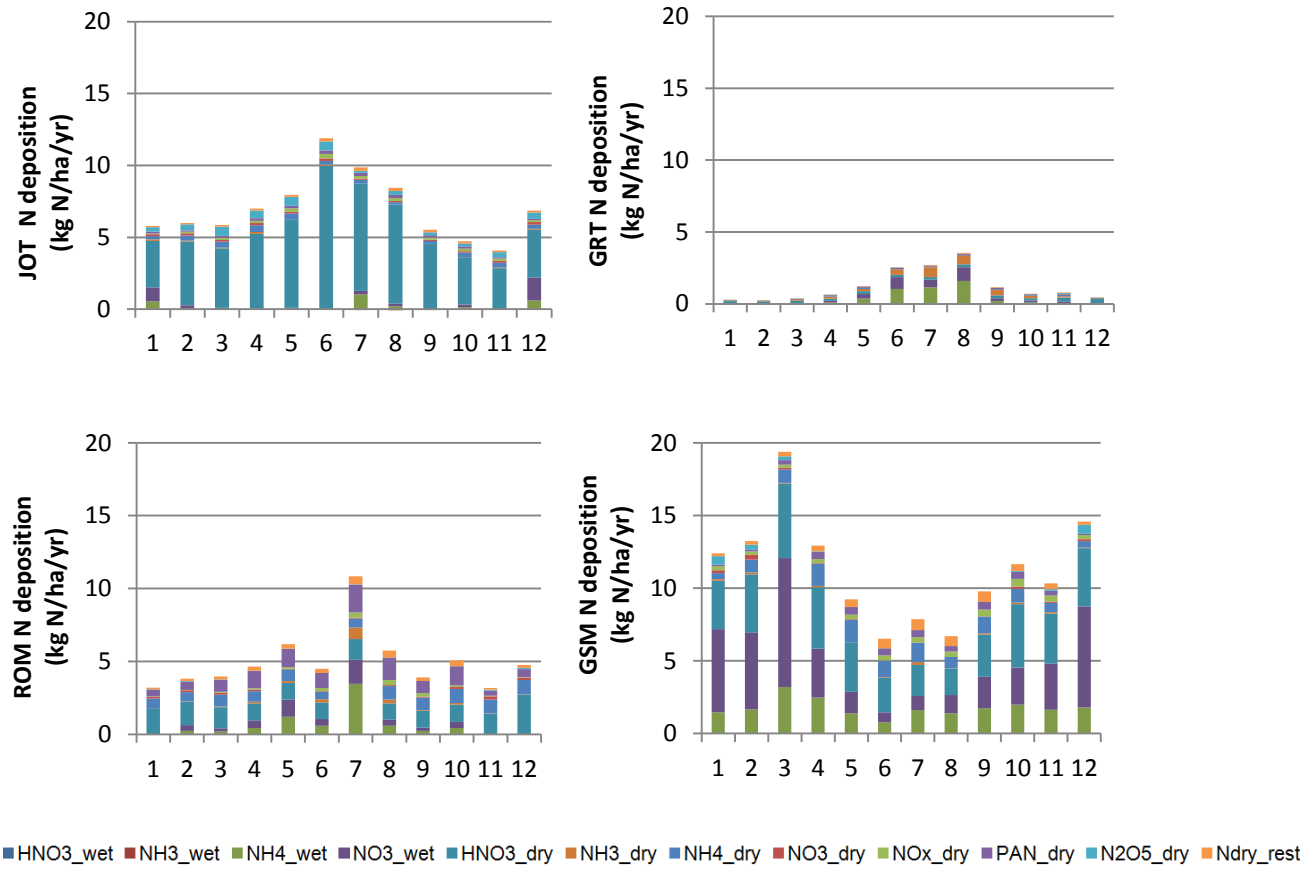

Figure 6.6: Modeled total nitrogen deposition normalized to yearly deposition for each pathway by month at Joshua Tree (top left), Grand Teton (top right), Rocky Mountain (bottom left), Great Smoky Mountain (bottom right) National Parks.

6.3.3.1 Agricultural Emission

Throughout the studied parks, wet NH_4^- and dry NH_3 deposition increased as agricultural NH_3 emission increased. Wet nitrate deposition also increased with an increase in NH_3 emissions since NH_3 reacts with oxidized nitrogen species to form ammonium nitrate. Since agricultural emissions are responsible for much of ammonia emissions in the US, nitrogen deposition at the national parks (Figure 6.7) near agricultural regions (GSM and ROM) were most sensitive to agricultural emissions. NH_3 emission from agricultural practices was predicted to be responsible for 3.4 kg N ha^{-1} yr^{-1}

of total nitrogen deposition at GSM, 1.0 kg N ha^{-1} yr^{-1} at ROM, 0.4 kg N ha^{-1} yr^{-1} at GRT and 0.3 kg N ha^{-1} yr^{-1} at JOT. Similar to the seasonal trend for the total nitrogen deposition (Figure 6.6), deposition sensitivity is larger for the warmer months except for GSM and January at JOT, which was the month with heaviest rainfall. The sensitivity study shows that agricultural practices alone could contribute to exceeding CL at GSM.

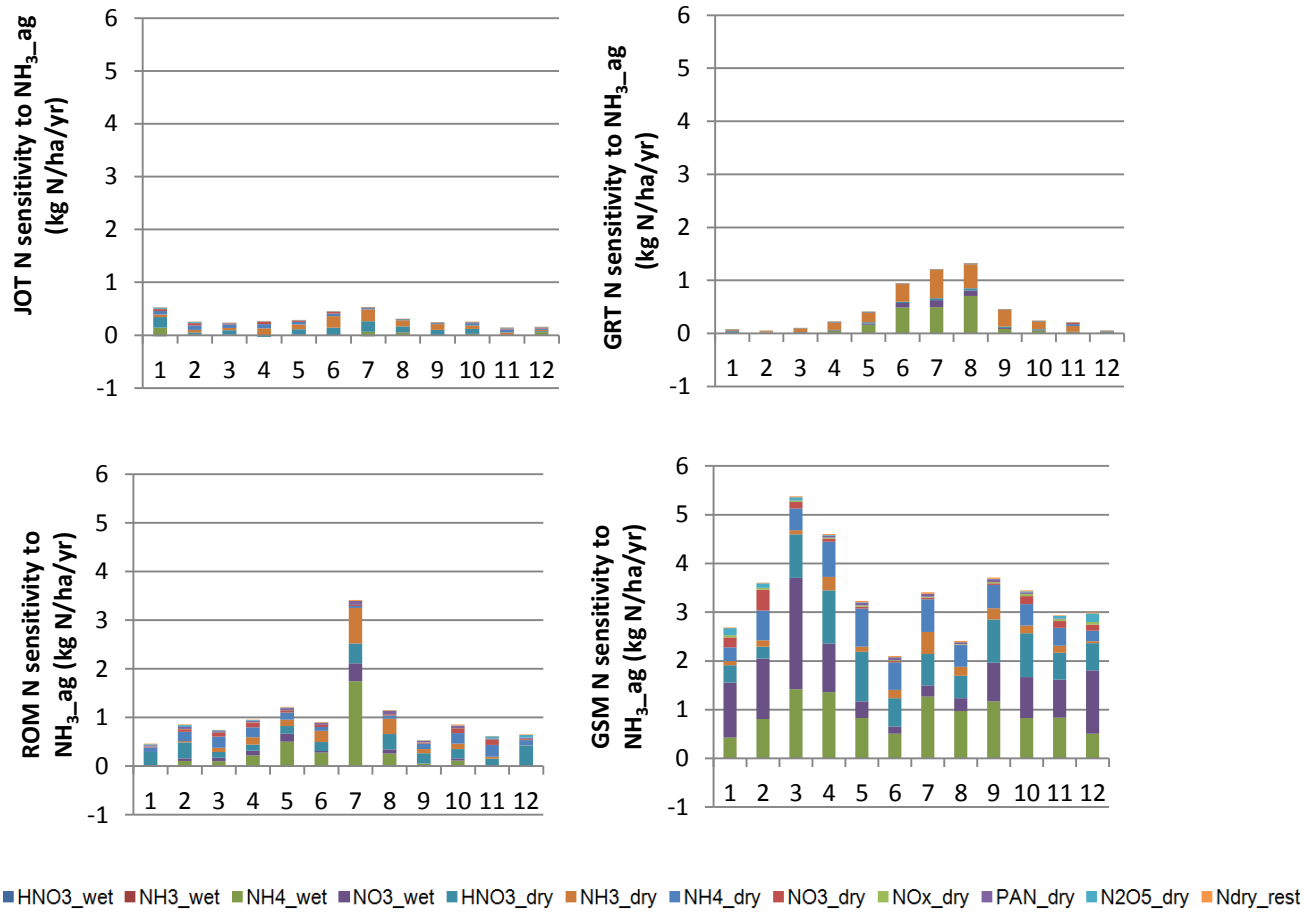

Figure 6.7: CMAQ simulated monthly nitrogen deposition sensitivity to agricultural NH_3 emission, normalized to yearly deposition at Joshua Tree (top left), Grand Teton (top right), Rocky Mountain (bottom left), Great Smoky Mountain (bottom right) National Parks.

6.3.3.2 Biogenic Emission

The sensitivity study of biogenic (soil) NO emission shows that biogenic NO emission does contribute to total nitrogen deposition at sites like ROM and GSM but not enough to exceed CLs from biogenic emissions alone. The simulations predicted that biogenic NO emissions are responsible for 1.0 kg N ha^{-1} yr^{-1} of total nitrogen deposition at ROM and 0.3 kg N ha^{-1} yr^{-1} at GSM. Biogenic nitrogen emission had very little effect on total nitrogen deposition at the other studied sites (JOT and GRT). Reactions related to ammonium nitrate play a large role in creating sensitivities of various nitrogen species to NO emissions. As NO emissions increased, so did HNO_3 concentrations. With more HNO_3 available in the atmosphere, NH_3 was consumed more to form $NH_4NO_{3(s)}$ or NH_4^+ and NO_3^- in aqueous phase. Since ammonium nitrate reaction is temperature dependent and favors to stay in gas phase during warm seasons, positive sensitivity to dry HNO_3 and wet NO_3^- and negative sensitivity to dry NH_3 and wet NH_4^+ increased during summer months.

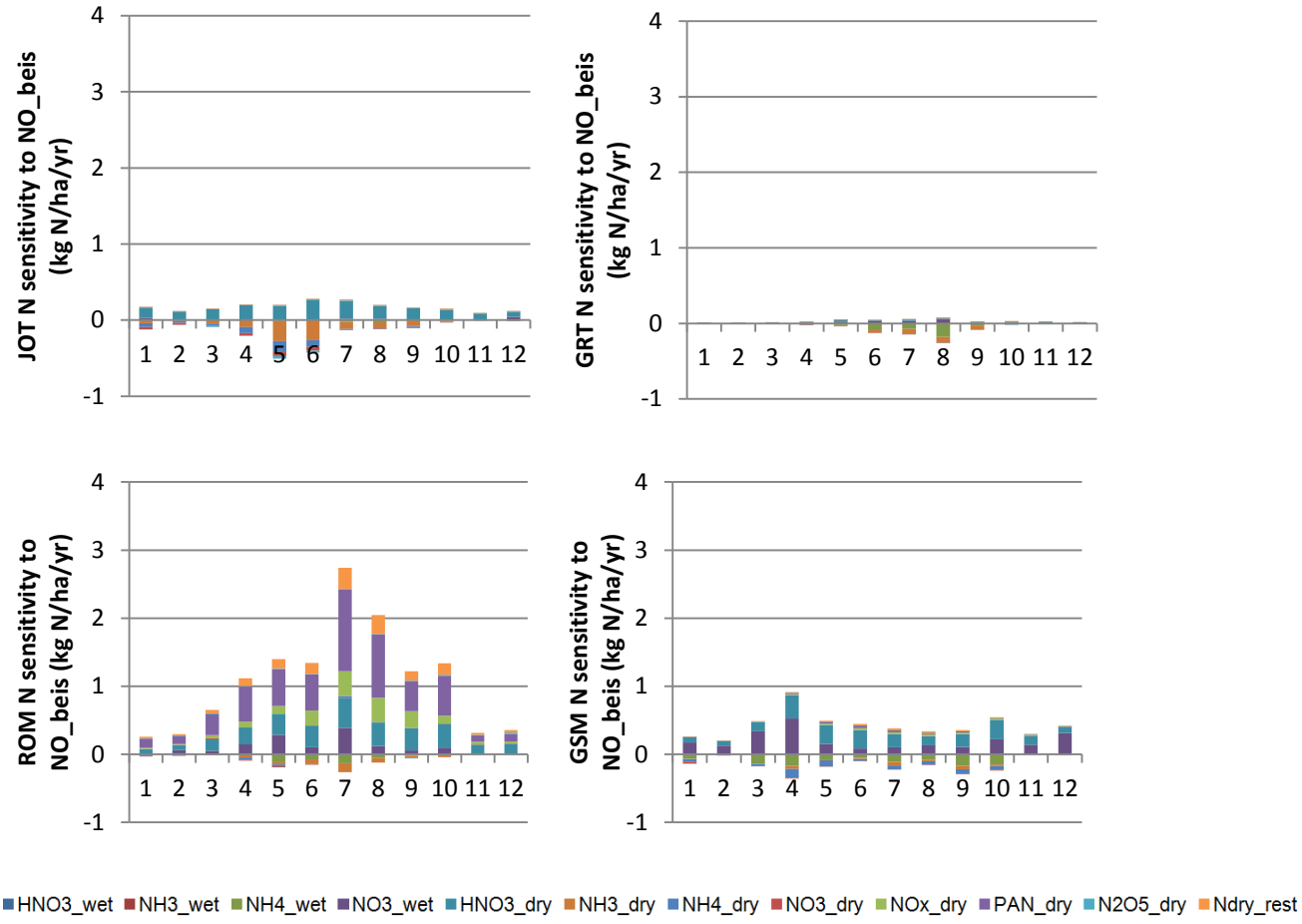

Figure 6.8: CMAQ simulated Monthly nitrogen deposition sensitivity to biogenic NO emission, normalized to yearly deposition at Joshua Tree (top left), Grand Teton (top right), Rocky Mountain (bottom left), Great Smoky Mountain (bottom right) National Parks.

6.3.3.3 Mobile Emission

Mobile NO_x emission has a large effect on nitrogen deposition at national parks near major cities. JOT is near Los Angeles and San Diego, as well as many roads heading towards/through Palm Springs, which is the closest city to JOT. NO_x emission from mobile sources was predicted to be responsible for 3.2 kg N ha^{-1} yr^{-1} of total nitrogen deposition at JOT. GSM is near Knoxville, Ashville, and Chattanooga with many interstates surrounding the national park. Mobile NO_x emission was predicted to be

responsible for 3.5 kg N ha^{-1} yr^{-1} of total nitrogen deposition at GSM. The nitrogen deposition sensitivities at both JOT and GSM were large enough to exceed the CLs just from mobile source emissions. Mobile source NO_x emission did not large of effect at ROM (with it affecting only 0.7 kg N ha^{-1} yr^{-1} of total nitrogen deposition) as it did for JOT and GSM despite ROM being next to Denver because of the winds typically blowing from west to east and ROM always being upwind of the city. GRT is located in a desolate area with little traffic, therefore only 0.1 kg N ha^{-1} yr^{-1} of total nitrogen deposition was predicted to be due to mobile source NO_x emissions.

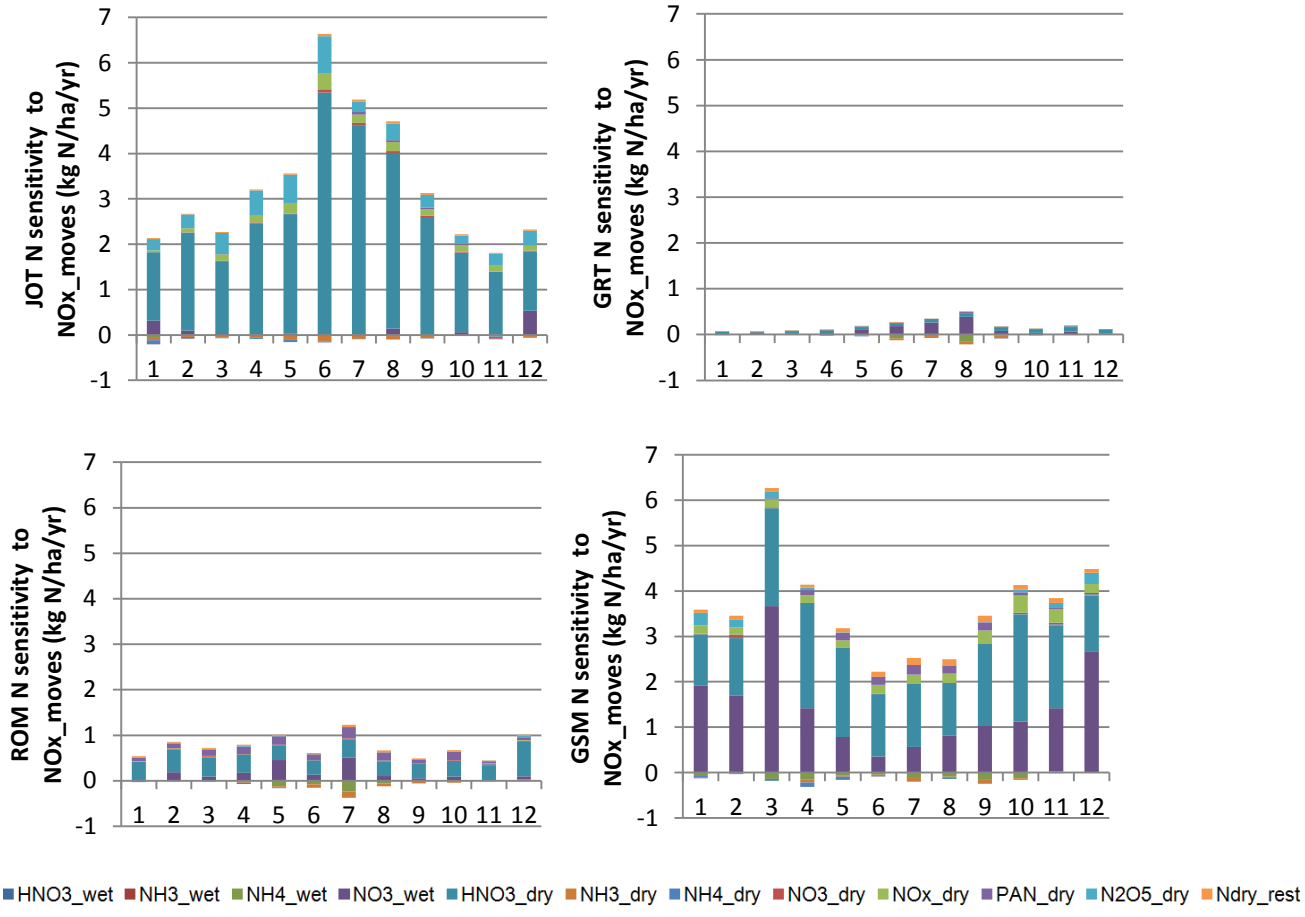

Figure 6.9: CMAQ simulated Monthly nitrogen deposition sensitivity to mobile NO_x emission, normalized to yearly deposition at Joshua Tree (top left), Grand Teton (top right), Rocky Mountain (bottom left), Great Smoky Mountain (bottom right) National Parks.

6.3.3.4 Power Plant Emission

Power plants also emit NO_x emission, which influenced the total nitrogen deposition at GSM, ROM, and JOT. GRT is not included in this part of the study since there was not a power plant inside the domain for GRT. GSM had the largest impact from its nearby power plant emissions with 1.6 kg N ha^{-1} yr^{-1} of total nitrogen deposition, contributing to half of CL. NO_x emissions from power plants near ROM did not have as much effect on its annual nitrogen deposition, affecting only 0.3 kg N ha^{-1} yr^{-1} of the total nitrogen deposition. Power plant emissions near JOT did not have a significant effect on total nitrogen deposition.

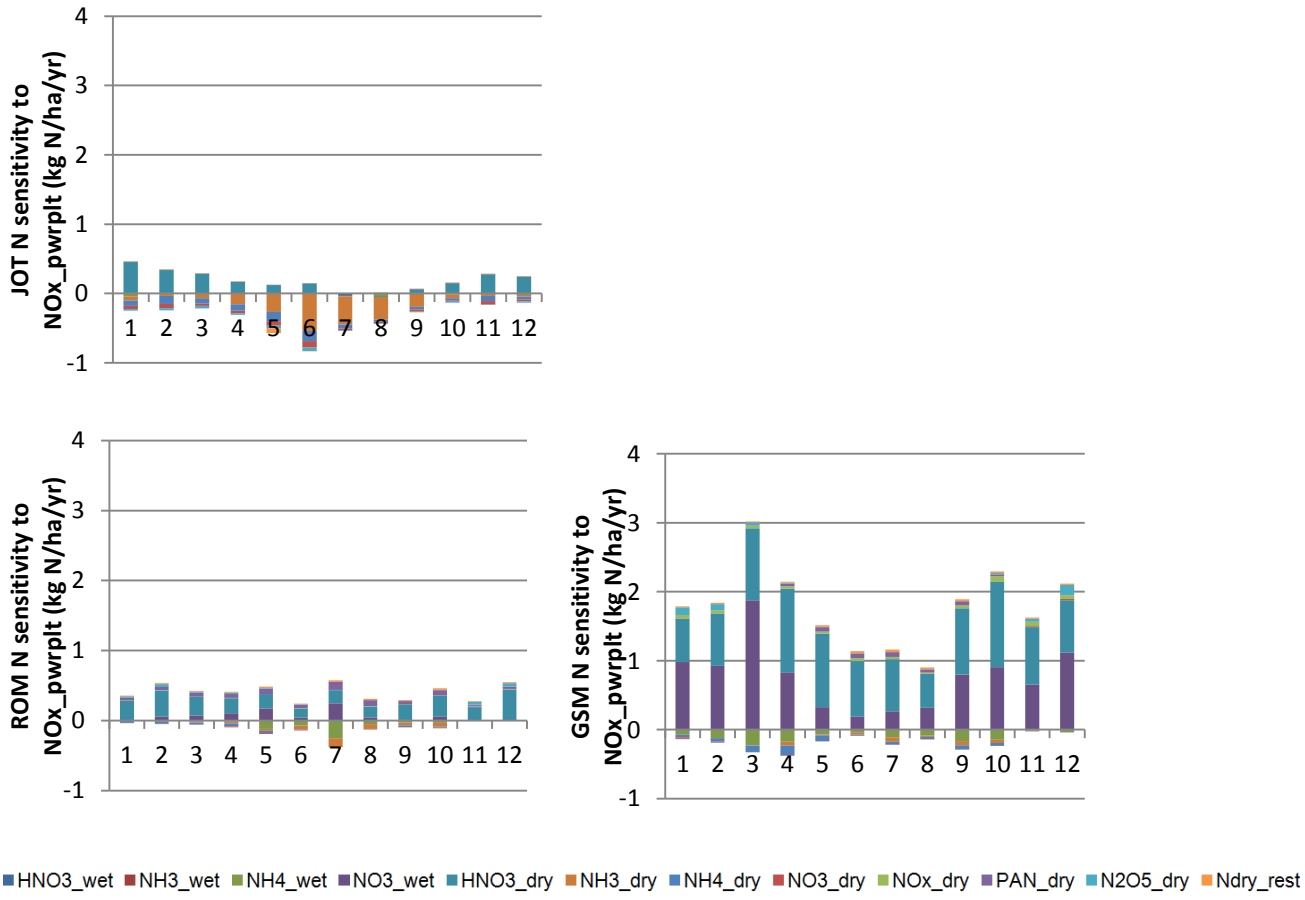

Figure 6.10: CMAQ simulated Monthly nitrogen deposition sensitivity to power plant NOx emission, normalized to yearly deposition at Joshua Tree (top left), Rocky Mountain (bottom left), Great Smoky Mountain (bottom right) National Parks.

6.4 Conclusion

In order to preserve the national parks in the US in its natural state, the ecosystem at the parks must be preserved as well. Excess nitrogen deposition is known to harm the ecosystem over the long term if it is above the CL. In this study, the atmospheric cycle of nitrogen emission, reaction, and deposition was simulated by CMAQ. CMAQ with bidirectional NH_3 exchange available in CMAQ version 5.0.1 was also used to replicate the natural processes as much as possible. Simulations were in agreement (within a factor of two) when compared to NADP concentration and wet deposition measurements and CASTNET predicted dry depositions. CMAQ also showed its strength in capturing spatial details of concentration and deposition gradients along road and mountains when using finer grid resolution (of 4 km grid cells).

The study predicted that for 2010, the total nitrogen deposition at JOT and GSM was well above the CL for each site. The sensitivity analysis of nitrogen deposition to anthropogenic and biogenic sectors showed that mobile source emission alone affected the nitrogen deposition to be above the CLs at JOT and GSM. NH_3 emission from livestock also was large enough to exceed CL by itself at GSM. NO emission from soil was large enough to contribute to about half of CL at ROM and power plant NO_x emission was large enough to contribute up to half of CL at GSM. The sensitivity analysis provided great insight on which emission sectors contributed to excess nitrogen deposition. Similar analysis can be applied for policy aspect, to identify the key contributing emitters and how much emission needs to be reduced in order to avoid CL exceedances at areas sensitive to nitrogen deposition.

6.5 References

Aber, J. D., C. L. Goodale, S. V. Ollinger, M.-L. Smith, A. H. Magill, M. E. Martin, R. A. Hallett, and J. L. Stoddard (2003), Is nitrogen deposition altering the nitrogen status of northeastern forests?, *BioScience*, *53*(4), 375-389.

Anderson, N., R. Strader, and C. Davidson (2003), Airborne reduced nitrogen: ammonia emissions from agriculture and other sources, *Environment International*, *29*(2–3), 277-286, doi:http://dx.doi.org/10.1016/S0160-4120(02)00186-1.

Bash, J., E. Cooter, R. Dennis, J. Walker, and J. Pleim (2013), Evaluation of a regional air-quality model with bidirectional NH 3 exchange coupled to an agroecosystem model, *Biogeosciences*, *10*(3), 1635-1645.

Cooter, E., J. Bash, V. Benson, and L. Ran (2012), Linking agricultural crop management and air quality models for regional to national-scale nitrogen assessments, *Biogeosciences Discussions*, *9*(5), 6095-6127.

Ellis, R., D. Jacob, M. Sulprizio, L. Zhang, C. Holmes, B. Schichtel, T. Blett, E. Porter, L. Pardo, and J. Lynch (2013), Present and future nitrogen deposition to national parks in the United States: critical load exceedances, *Atmospheric Chemistry and Physics*, *13*(17), 9083-9095.

Galloway, J. N., J. D. Aber, J. W. Erisman, S. P. Seitzinger, R. W. Howarth, E. B. Cowling, and B. J. Cosby (2003), The nitrogen cascade, *Bioscience*, *53*(4), 341-356.

Howarth, R. W., G. Billen, D. Swaney, A. Townsend, N. Jaworski, K. Lajtha, J. Downing, R. Elmgren, N. Caraco, and T. Jordan (1996), Regional nitrogen budgets and riverine N & P fluxes for the drainages to the North Atlantic Ocean: Natural and human influences, in *Nitrogen cycling in the North Atlantic Ocean and its watersheds*, edited, pp. 75-139, Springer.

Pardo, L. H., M. E. Fenn, C. L. Goodale, L. H. Geiser, C. T. Driscoll, E. B. Allen, J. S. Baron, R. Bobbink, W. D. Bowman, and C. M. Clark (2011), Effects of nitrogen deposition and empirical nitrogen critical loads for ecoregions of the United States, *Ecological Applications*, *21*(8), 3049-3082.

Pleim, J. E., and A. Xiu (1995), Development and testing of a surface flux and planetary boundary layer model for application in mesoscale models, *Journal of Applied Meteorology*, *34*(1), 16-32.

Ran, L., E. Cooter, V. Benson, and Q. He (2012), Development of an Agricultural Fertilizer Modeling System for Bi-directional Ammonia Fluxes in the CMAQ Model, in *Air Pollution Modeling and its Application XXI*, edited, pp. 213-219, Springer.

Skamarock, J., W. Klemp, J. Dudhia, D. Gill, D. Barker, M. Duda, X. Huang, W. Wang, and J. Powers (2008), A description of the advanced research WRF version 3, NCAR technical note*Rep*., NCAR/TN–475+ STR.

Stevens, C. J., N. B. Dise, J. O. Mountford, and D. J. Gowing (2004), Impact of nitrogen deposition on the species richness of grasslands, *Science*, *303*(5665), 1876-1879.

Trail, M., A. Tsimpidi, P. Liu, K. Tsigaridis, J. Rudokas, P. Miller, A. Nenes, Y. Hu, and A. Russell (2014), Sensitivity of air quality to potential future climate change and emissions in the United States and major cities, *Atmos Environ*.

Yarwood, G., S. Rao, M. Yocke, and G. Whitten (2005), Updates to the Carbon Bond chemical mechanism: CB05, *Final report to the US EPA, RT-0400675*, *8*.

CHAPTER 7

Conclusions

7.1 Major Findings

This thesis covered some of the issues that exist in air quality modeling and has been an ongoing development over the last decade or so. One is the issue of resolving smoke emission from fire in an air quality model, and the other is accurately expressing nitrogen flux between crop/soil and atmosphere in an air quality model. For both issues, sub-grid models have been applied. Previously, fire emissions were typically averaged out throughout the day in emissions model called SMOKE (which led to underestimating the peak concentrations from the burn event) and were inserted at the ground level (which overestimated the smoke concentration at the ground level, especially when the plume entered troposphere). Some studies and recent versions in SMOKE started to inject smoke emissions at higher altitude. However, inserting smoke emissions at higher altitude into a chemical transport model still cannot capture the details such as plume development and entrainment of the plume without including plume specific physics into the air quality model. The studies in the first few chapters were built on top of each other to produce the final version of coupled fire plume-air quality model, Daysmoke-CMAQ. Daysmoke-CMAQ was used to simulate various prescribed burning cases.

The coupling of cropping soil system model in CMAQ was performed by EPA to resolve the unwanted biases that existed in concentration and deposition of nitrogen species. CMAQ with bidirectional ammonia exchange was used to study the transport of

nitrogen emissions in the atmosphere and to identify the nitrogen emission sectors that are responsible for the increase in nitrogen deposition. Another chemical transport model, GEOS-CHEM, was also used for this study by other researchers, but we were interested in using CMAQ particularly to simulate the nitrogen deposition field in detail using finer resolution than GEOS-CHEM. The results from CMAQ simulations were presented in the previous chapter. Major findings from each chapter are presented below.

Chapter 2: Fire Emission Uncertainties and their Impact on Smoke Dispersion Predictions: a Case Study at Eglin Air Force Base, Florida, USA

Fuel loading, fuel consumption, emission factor, emission rate are required for calculating fire emissions and how each parameter's uncertainty affects plume dispersion modeling was studied. For the studied site, uncertainty in emission factors contributed the most significant emission uncertainty. Daysmoke, a plume dispersion model, simulated downwind concentration to be in agreement with the observations when appropriate input parameters were used. Fire emissions affected the uncertainty in downwind concentration, greater than Daysmoke's model uncertainty. Accuracy in fire emissions, as well as other input parameters, are significant for enhancing plume dispersion simulations.

Chapter 3: Prescribed Burning Plume Dispersion Simulation in an Air Quality Model using Ground and Satellite Data

For the studied case, satellite-derived fire emissions were severely lower when compared to emissions estimated from ground measurements using the bottom-up approach. The satellite visually detected fire spread rate, which led to predicting the shape of the plume similar to the observed shape. Total ground-based emissions were converted to fire emission rates using rates from satellite retrievals. Daysmoke simulation

was performed using the hybrid of the two, which was able to capture changes in plume concentration similar to aircraft measurements. Satellite retrievals are used for fire emission calculations, however, combining ground data with satellite retrievals are recommended for smaller fires (i.e., prescribed burnings).

Chapter 4: Coupling of Smoke Dispersion Model with Air Quality Model: Combining Lagrangian Model with Eulerian Model

A new method for coupling a plume dispersion model in an air quality model was introduced. Daysmoke-CMAQ simulated plume growth and dispersion in Daysmoke until the plume was fully developed at a certain distance away from the fire. At the interface between Daysmoke and CMAQ, Daysmoke smoke particles were converted into concentrations and handed over to CMAQ. The coupling of the two models preserved the plume farther in CMAQ. Including adaptive grid in the coupled system further reduced numerical diffusion.

Chapter 5: An Assessment of Air Quality Deterioration from Prescribed Burning Scenarios in a Longleaf Pine Forest

Age of the fuelbed, burn area size, ignition type, start time, and season of the burn are some of the key parameters to be considered when planning for a prescribed burn. Effects of parameters listed above were studied through Daysmoke-CMAQ for a longleaf pine forest in southeastern US. Minimal increases in emission and downwind concentration were observed between fuels with a 2-year age difference. Burn area showed to be one of the more important parameters since an increase in burn area significantly affected the downwind concentration at ground level. Aerial ignition burned more efficiently with less emission, however, the cost and availability of the method may

not always be practical. Relative humidity and planetary boundary layer (PBL) height varied with time of the day and/or season of burn. Simulations showed that when fuels lost its moisture, more pollutants were emitted. In general, the plumes reaching above PBL transported less pollutant on the ground.

Chapter 6: Reactive Nitrogen Deposition over US National Parks: Sensitivity to Anthropogenic and Biogenic Emissions

Reactive nitrogen deposition varied seasonally, with a tendency to increase nitrogen deposition in the summer. Reactive nitrogen deposition was sensitive to anthropogenic and biogenic emissions, and the magnitude varied from month to month. Ammonium nitrate influenced total nitrogen deposition for colder months. Mobile emissions had the largest sensitivity to nitrogen deposition, and mobile source emissions alone can be responsible for exceeding critical load for national parks near cities. Ammonia emissions from livestock also affected nitrogen deposition at nearby national parks, also having the potential to exceed critical load just from agricultural practices. Biogenic and power plant emissions had minimal impact to the studied national parks throughout US.

7.2 Recommendation for Future Research

Problems relating to plume dispersion modeling in air quality models were addressed, however there are more areas to be improved. Chemical reaction rates inside the plume differ from reactions in ambient atmosphere due to differences in environmental conditions such as temperature and oxydant availability. Plume chemistry has been studied by various groups, for example *Akagi et al.* [2012] studying evolution of

trace gasses in the plume, and chemical reactions can be formulated based on their measurements. Ozone chemistry has been implemented in a Lagrangian plume model by *Alvarado and Prinn* [2009], and some of the major plume reactions are included in a few models such as CALPUFF [*Karamchandani et al.*, 2000]. Adding plume chemistry to Daysmoke would improve plume dispersion and chemistry in CMAQ and other air quality models.

The effect of numerical diffusion in CMAQ can be minimized by modifying CMAQ's advection and diffusion schemes. Adding parameters and criteria to account for plume buoyancy, temperature difference inside the plume and its surroundings, can aid in minimizing the strong vertical mixing within PBL that exist in CMAQ. Also adding a parameter for plume entrainment can reduce the effect of numerical diffusion to the plume's surrounding grid cells. Daysmoke-CMAQ can also be improved if Daysmoke is modified to predict plume dispersion to farther distance away from the fire for small and large fire events, and CMAQ includes parameters listed above or other key parameters to better represent the nature of smoke plumes. For that, better measurements on plume height, structure, and concentration gradient are needed. Details of a plume such as plume height and thickness can be measured by LIDAR technology for example; therefore, collaborating with measurement teams can assist with model improvements.

Climate change and its effect on fire occurrences, vegetation, and atmosphere is another area of interest. Daysmoke-CMAQ can be used as a fire forecasting tool by linking it to weather forecast models, along with a fuels map, and fire models. Meteorological models like WRF can produce gridded meteorological data, which can be used to calculate Haines index or other fire danger index and determine which areas are

likely to ignite. After the area is determined, fire emissions can be calculated for the area of interest by extracting fuels data from online Photo series. Once the data to calculate fire emissions are extracted, fuel consumption and emission rates can be calculated following the bottom-up method explained in Chapter 2. Daysmoke-CMAQ can use the calculated fire information with forecasted meteorology to predict plume dispersion and transport. It also can advise citizens to be aware of potentially heavy smoke traveling to their region and react accordingly.

7.3 Closing Remarks

In summary, this thesis has provided insights regarding plume dispersion modeling in an air quality model. Its findings can be used to improve current methods of treating fire emissions in air quality modeling. Methods developed and applied in this thesis should be applicable to other episodes throughout the world and with other models. The thesis also highlighted the issues that exist in smoke dispersion modeling in an air quality model, and listed guidance for future research and applications.

7.4 References

Akagi, S., J. Craven, J. Taylor, G. McMeeking, R. Yokelson, I. Burling, S. Urbanski, C. Wold, J. Seinfeld, and H. Coe (2012), Evolution of trace gases and particles emitted by a chaparral fire in California, *Atmos Chem Phys*, *12*(3), 1397-1421.

Alvarado, M. J., and R. G. Prinn (2009), Formation of ozone and growth of aerosols in young smoke plumes from biomass burning: 1. Lagrangian parcel studies, *Journal of Geophysical Research: Atmospheres (1984–2012)*, *114*(D9).

Karamchandani, P., L. Santos, I. Sykes, Y. Zhang, C. Tonne, and C. Seigneur (2000), Development and evaluation of a state-of-the-science reactive plume model, *Environmental science & technology*, *34*(5), 870-880.